One-off ocean nitrogen fertilization as carbon dioxide removal strategy?

Exploring its long-term carbon sequestration potential

Master thesis

N.M.J. (Noor) Kloppenburg

TUDelft

Van Oord

One-off ocean nitrogen fertilization as carbon dioxide removal strategy?

Exploring its long-term carbon sequestration potential

by

N.M.J. (Noor) Kloppenburg

to obtain the degree of Master of Science in Civil Engineering
at the Delft University of Technology,
to be defended publicly on Thursday the 14th of December.

On the cover: Summer blooms in the Baltic Sea - July 18, 2018 - NASA Earth Observatory images by Joshua Stevens and Lauren Dauphin, using Landsat data from the U.S. Geological Survey and MODIS data from LANCE/EOSDIS Rapid Response

TUDelft Delft University of Technology

Van Oord
Marine ingenuity

Preface

Dear reader,

Before you lies my thesis, which marks the completion of my master's degree in Hydraulic Engineering at the faculty of Civil Engineering and Geosciences at the Delft University of Technology.

I would like to thank my committee for helping me realise this thesis. First of all, many thanks to Gerben de Boer for your enthusiasm and invaluable feedback anytime I needed it. You gave me a lot of freedom during this project, yet your guidance ensured I never lost sight of the end goal. Secondly, I would like to thank Caroline Katsman, our discussions and your crucial advice have contributed to enhancing this report. Peter Herman, thank you for your knowledge on (marine) ecology and comprehensive feedback regarding the overall evaluation. Lastly, thank you Julia Gebert for your insightful view and questions.

Finally, I want to express my gratitude to my friends and family for their support. You not only assisted me in this project but also provided moments of fun and distraction when needed.

N.M.J. (Noor) Kloppenburg
Rotterdam, December 2023

Abstract

To limit global warming to 2 °C or below, the IPCC emphasizes the need for large-scale carbon dioxide removal (CDR) alongside emissions reductions. There is a growing recognition of ocean-based CDR techniques and expanded research is needed. This thesis investigated the long-term (>100 years) carbon sequestration potential of enhancing the biological carbon pump by ocean nitrogen fertilization, a research domain which so far has received little attention. The objective was to make an initial rough quantification of the (cumulative) CDR potential of one-off ocean nitrogen fertilization achieved within 5 years after the fertilization, to evaluate its potential as a global CDR technique and for commercial implementation.

An idealized one-dimensional vertical (1DV) model framework, coupling a marine ecosystem model with a vertical eddy diffusion physical model, was established to simulate ocean nitrogen fertilization, incorporating essential processes of ocean productivity and the biological carbon pump. Half of the ocean was excluded from the framework since these regions are incompatible with 1DV modeling. Additionally, regions where nitrogen is not the first limiting nutrient were excluded. Various fertilization simulations were performed in which the nitrogen limitation in the mixed layer of the remaining ocean areas was replenished by a one-off addition. Long-term carbon sequestration resulting from fertilization was assessed by comparing these simulations with baseline simulations of the biological carbon pump.

An aggregated global outcome, forming the basis for feasibility assessment, was derived by averaging over simulations, while excluding hexagons with low sequestration efficiency as they contribute insignificantly to CDR.

In principle, the one-off nitrogen fertilization shows an effective carbon sequestration efficiency (2.95 kg CO_2 per kg N). However, the high and challenging-to-reduce carbon footprint of current urea production, coupled with challenges in collecting manure and the priority of utilising it in agriculture rather than directing it for carbon removal, leads to a low overall global carbon sequestration potential. Nevertheless, it is demonstrated that implementing one-off nitrogen fertilization at a location with high sequestration efficiency using manure can be commercially viable. The cost per net tonne of CO_2 sequestered is lower than the current market price of a carbon credit, considering the transportation is conducted with vessels that would have navigated the route regardless.

Based on the findings of this study, it is concluded that nitrogen fertilization has very limited potential to serve as a large-scale global carbon dioxide removal strategy, but can be effectively employed on company-level using surplus manure without agricultural purpose. The initial quantification, despite inherent limitations such as the use of a 1DV modelling approach, serves as a valuable addition to the scarcity of research in the domain of ocean nitrogen fertilization. Further more detailed research into strategic nitrogen fertilization for company-level CDR is justified, with this study providing valuable guidance on optimal research locations.

Executive summary

To limit global warming to 2 °C or less, deep and immediate emissions reductions alone are not enough. The IPCC emphasizes the need for large-scale carbon dioxide removal (CDR) to meet the Paris Agreement, which requires collective action from governments and the private sector. CDR techniques remove CO_2 from the atmosphere and sequester it for a minimum of 100 years (long-term) to qualify as carbon credits. There is a growing recognition of ocean-based CDR techniques, which aim to accelerate the ocean's natural processes of the carbon cycle, thereby increasing the uptake of CO_2. One of these processes is the biological carbon pump (BCP). Phytoplankton use sunlight and nutrients to convert dissolved CO_2 into organic matter. A portion of this organic matter is exported to the deeper ocean and remineralized (broken down) back into CO_2 and nutrients at depth. The CO_2 is then sequestered in the ocean until it reaches the surface again. Since most remineralization happens at smaller rather than larger depths, the BCP is primarily associated with storage timescales shorter than 100 years. One proposed CDR approach to boost the BCP is ocean fertilization, which involves adding micro- (e.g. iron (Fe)) or macronutrients (e.g. nitrogen (N) or phosphorus (P)) to regions with limited availability of these nutrients, stimulating phytoplankton growth and consequently CO_2 export to the deep ocean.

This thesis examined the potential of ocean nitrogen fertilization, an underexplored research domain. The objective was to provide an initial quantification of the CDR potential of one-off ocean nitrogen fertilization reached within 5 years, to evaluate its potential as a global CDR technique and for commercial implementation. The objective of this thesis (determining the long-term carbon storage for the CDR potential), as well as the one-off fertilization and the possible marine nitrogen cycle offsetting (loss) feedbacks are illustrated in the figure below.

Due to the exploratory nature of this thesis and the time constraints, the scope was narrowed to the use of a one-dimensional vertical (1DV) model framework, which is valid for 50% of the ocean. A marine biochemical ecosystem model was coupled to a 1DV physical circulation model. The chosen marine ecosystem model has a simple structure, but incorporates the feedbacks from nitrogen fixation and denitrification and the competition for phosphorus, which are crucial for studying ocean nitrogen fertilization. The model is mass conservative for N and P, with C as free parameter through CO_2 exchange with the atmosphere. The physical model only considers vertical eddy diffusion, for which the
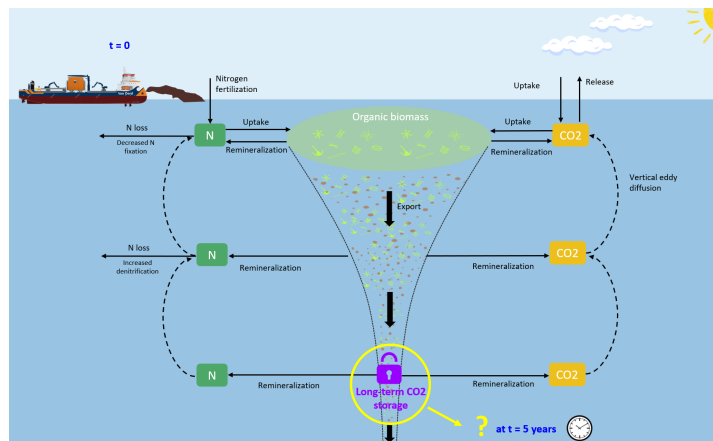
stratified ocean is regarded as a three-layer system comprising the surface mixed layer, the thermocline and the deep ocean, each with a constant eddy diffusivity. Global average eddy diffusivity values were used for the mixed layer and deep ocean, while four different values were employed for the thermocline to address uncertainty and analyse the sensitivity. For this 1DV framework, the ocean was divided into hexagonal columns ($87 \cdot 10^3$ km^2 each). Prior to conducting simulations, hexagons were excluded where the horizontal surface transport of nutrients was considered to be dominant. Additionally, regions were filtered out that were not of interest for the study, with the primary criterion being the exclusion of areas where nitrogen is not the first limiting nutrient.

The model framework was used to assess the effect of the nitrogen fertilization. Initially four baseline simulations of the BCP were performed, characterized by the different thermocline diffusivity values (10^{-5}, $3 \cdot 10^{-5}$, $6 \cdot 10^{-5}$ and 10^{-4} m^{2}s^{-1}). These baseline simulations functioned as model spin-up and as a basis for comparison. In the fertilization simulations nitrogen was fertilized as a one-off (single pulse) addition to all hexagons, fully replenishing the nitrogen limitation in the mixed layer of the hexagons. The variations in fertilization simulations included differences in the spin-up time of the baseline simulation, the moment (season) of nitrogen addition and the thermocline diffusivity, resulting in a total of 32 fertilization simulations. The long-term carbon sequestration reached within a 5-year period following the fertilization was derived by post-processing the additional CO_2 release from organic matter remineralization in the fertilization simulation compared to the baseline simulation, together with the sequestration fractions from another study.

The 32 simulations indicated that the globally integrated long-term carbon sequestration as result from the nitrogen additions varies between 0.07 and 0.18 Gt. An aggregated outcome was derived by averaging over the fertilizations performed in July (which were characterized by a large absolute sequestration), while excluding hexagons with a low sequestration efficiency as these contribute insignificantly to CDR. It was determined that one-off fertilizing 0.20 Gt of nitrogen results in the long-term carbon sequestration of 0.16 Gt of carbon after 5 years, which is equivalent to 0.59 Gt of CO_2. This implies (an average) sequestration of 2.95 kg of CO_2 per kg of nitrogen.

The implementation of nitrogen fertilization would start at specific locations, driven by both their carbon sequestration potential and considerations of delivery costs and associated emissions. Therefore, high-potential locations were identified that align with high-intensity shipping mobilisation routes. Transportation to these locations limits costs and emissions, as the vessels would have navigated the route regardless but then in empty state.

The aforementioned results were used in the overall evaluation of the potential of one-off nitrogen fertilization. For the global evaluation, the impact and availability of fertilizers were considered. 0.59 Gt of CO_2 accounts for 8% of annual global CO_2 removal target. Therefore, a for example annual repetition of the fertilization is necessary for this approach to have a significant impact in the context of a global CDR strategy. The current carbon footprint of urea exceeds the carbon sequestration capacity, yielding a negative CDR potential. While urea might one day be produced in a 'green' manner, leading to a positive carbon storage, leveraging limited renewable resources to triple the global urea production is not anticipated to be a priority in meeting the Paris Agreement. Manure presents another fertilizer option. However, its global-scale collection poses a challenge, and it should be directed towards agriculture. Overall, the global carbon sequestration potential of one-off nitrogen fertilization is considered low.

Nevertheless, the assessment of transporting manure to one of the 'high-potential' locations revealed that implementing nitrogen fertilization is commercially viable. The cost per net tonne of CO_2 sequestered is lower than the current price of a carbon credit.

It can be concluded that nitrogen fertilization possesses very limited potential to serve as a large-scale global carbon dioxide removal strategy. However, it does demonstrate viability as a company-level CDR approach using surplus manure without an agricultural purpose. The initial quantification, despite inherent limitations such as the use of a 1DV modelling approach, serves as a valuable addition to the scarcity of research in the domain of ocean nitrogen fertilization. Further more detailed research into strategic nitrogen fertilization for company-level CDR is justified, with this study providing valuable guidance on optimal research locations.

Contents

List of Figures

List of Tables

Abbreviations

1DV	One-dimensional vertical
3D	Three-dimensional
BCP	Biological carbon pump
BS	Baseline simulation
CDR	Carbon dioxide removal
$\mathbf{D}_{ML}$	Diffusivity of the surface mixed layer
$\mathbf{D}_{thermo}$	Diffusivity of the thermocline
$\mathbf{D}_{deep}$	Diffusivity of the deep ocean
DIC	Dissolved inorganic carbon
DOM	Dissolved organic matter
FS	Fertilization simulation
Gt	Gigatonne
IPCC	Intergovernmental Panel on Climate Change
LT	Long-term (used for carbon storage of 100 years or more)
MLD	Mixed layer depth
NPP	Net primary production
OMZ	Oxygen minimum zone
POM	Particulate organic matter
WOA	World Ocean Atlas

1 | Introduction

This chapter gives an introduction to the research topic, starting with the background information and relevance of the topic in section 1.1. The objective and scope of this thesis are presented in sections 1.2 and 1.3, respectively. Subsequently, the formulated research questions to achieve the study's objective are given (section 1.4). Section 1.5 describes the outline of this thesis.

1.1. Scientific background

1.1.1. The imperative for carbon dioxide removal

The Earth's atmospheric CO_2 levels have now reached historically unprecedented values. Since the industrial revolution, humans have emitted 1.5 trillion tons of CO_2 from activities such as fossil fuel burning and agriculture (National Oceanic and Atmospheric Administration, 2022). It is undeniable that these anthropogenic emissions have caused global warming, leading to amongst others increased risks of floods and droughts, sea level rise and alterations to the environment. Drastic actions are imperative to mitigate further climate change. While reaching net-zero CO_2 emissions by mid-century is required to meet the Paris Agreement, the Intergovernmental Panel on Climate Change (IPCC) climate models indicate that immediate and deep emissions reductions alone are not enough. Large-scale **carbon dioxide removal (CDR)** is part of all modelled scenarios that limit global warming to well below 2 °C, preferably to 1.5 °C (IPCC, 2022) (Figure 1.1). The amount of CDR that is ultimately needed is uncertain, but the IPCC suggests that around 600 Gigatonnes (Gt) of CO_2 need to be removed from the atmosphere by 2100, or on average 7.5 Gt CO_2 per year (starting in 2020) (IPCC, 2022). Achieving these goals requires collective action from governments and the private sector.

Several biotic and abiotic CDR techniques exist, but all require some step of removing CO_2 from the atmosphere or a reservoir in close contact with the atmosphere (e.g. surface ocean) and storing it in another reservoir with the goal of limiting CO_2 release back to the air for some period of time (National Academies of Sciences & Medicine, 2019). The IPCC considers carbon stored for 100 years or more as carbon that is sequestered on climate-relevant timescales (Baker et al., 2022; Boettcher et al., 2019). Therefore, this 100-year timescale is mostly used as the benchmark for carbon removal projects to be considered as 'permanent' and used for carbon credits (Sylvera, 2022). In this thesis, sequestration for 100 years or more is referred to as '**long-term**' storage.

To date, most research has primarily focused on land-based CDR strategies. However, there is a growing recognition of the potential of ocean-based strategies. Scientists are emphasizing the need to accelerate and expand research and field testing of these techniques, to evaluate their effectiveness, environmental impacts and scalability (Boettcher et al., 2019; Goreau, 2023; Lebling et al., 2022; National Academies of Sciences & Medicine, 2022). In line with this, the EU has recently initiated a project dedicated to investigating these aspects (Kiel Institute for the World Economy, 2023). This study therefore explores the potential of an ocean-based CDR technique. The role of the ocean in the carbon cycle and ocean-based CDR techniques are briefly introduced below.
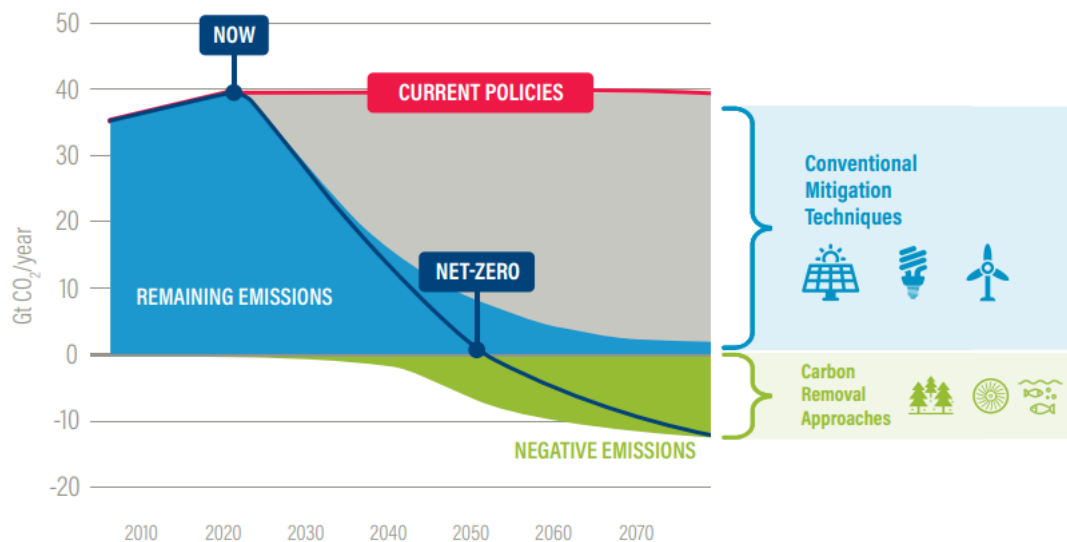
Figure 1.1: Emission pathway to stay below 1.5 °C of global temperature rise (Lebling et al., 2022). This figure illustrates that deep and immediate emissions reductions are required, but not enough to reach this goal. Negative emissions (carbon dioxide removal) are part of the pathway to limit global warming to below 1.5 °C.

1.1.2. The ocean as CDR strategy

The ocean covers 70% of the Earth's surface and acts as a large natural carbon reservoir. It holds around 50 times more carbon than the atmosphere (De Vries, 2022) and absorbs CO_2 at a rate equal to roughly 25% of the annual human emissions (Friedlingstein et al., 2022). Consequently, the ocean carbon cycle plays a critical role in controlling the global climate and moderating the effects of climate change. The air-sea exchange of CO_2 regulates the link between the ocean and atmospheric carbon reservoirs. When carbon dioxide is dissolved in the seawater it becomes part of the **dissolved inorganic carbon (DIC)** pool of the ocean. The magnitude of ocean carbon storage is governed by two mechanisms: the carbon buffering capacity of seawater and the vertical gradient in DIC, which are controlled by natural processes of the ocean carbon cycle (Boyd et al., 2019; De Vries, 2022). Ocean-based CDR techniques aim to accelerate these natural processes, enhancing the uptake and storage of CO_2 from the atmosphere (De Vries, 2022). This study focuses on an ocean-based CDR technique that aims to stimulate the soft tissue biological carbon pump. The soft tissue biological carbon pump, hereafter just referred to as the **biological carbon pump (BCP)**, is one of these natural processes that maintains the surface-to-deep gradient in DIC and therefore plays a major role in the ocean carbon cycle. Before discussing this CDR technique, the BCP is elaborated on below. Subsequently, 1.1.4 addresses how the BCP can be stimulated.

1.1.3. Biological Carbon Pump

The ocean's biological carbon pump represents the set of complex processes in which DIC is fixed into organic carbon created by phytoplankton's **net primary production (NPP)** and transported to the ocean interior, where it can be stored for months to millennia (Siegel et al., 2023). **Carbon fixation** is the process wherein photosynthetic organisms turn inorganic carbon into organic compounds. In a hypothetical scenario where marine life abruptly stops and thus disrupts CO_2 storage by the BCP, the atmospheric carbon dioxide levels would increase by 50% (Heinze et al., 2015)

Phytoplankton photosynthesize CO_2 dissolved in seawater into organic matter using sunlight and nutrients, and they release oxygen during this process. Phytoplankton form the base of the oceanic food web. Most of this organic matter is converted back to CO_2 and nutrients in the surface ocean, where the matter is consumed by zooplankton and other organisms or remineralized by microbes. **Remineralization** is the breakdown of organic matter into the inorganic elements (CO_2 and nutrients), which is dependent on seawater temperature and oxygen concentration (with higher remineralization rates for higher temperatures and oxygen concentrations) (Laufkötter et al., 2017). These recycled elements can be used by phytoplankton again for their production (Sigman & Hain, 2012). A portion of the organic

matter is exported from the upper ocean into the ocean interior. The flux of organic matter decreases with depth, and eventually less than 1% of the NPP reaches the deep seafloor (Iversen, 2023). The residual organic carbon is remineralized back to dissolved inorganic carbon and nutrients in the water column, and stored in the ocean until it reaches the surface ocean again. At the surface the CO_2 can escape into the atmosphere and nutrients can be reused.

Through the uptake and transport of CO_2 fixed in organic matter, the BCP leads to a vertical gradient in DIC, with low concentrations in the surface ocean and high concentrations at depth. The BCP therefore regulates the ocean's capacity to take up CO_2 from the atmosphere (Kwon et al., 2009).

There are three primary export pathways of organic carbon within the BCP; gravitational settling, vertical migration and physical transport (Iversen, 2023). These three export pathways are illustrated in Figure 1.2, as well as the mixing of DIC and nutrients back to the surface ocean. The first pathway refers to the downward sinking of **particulate organic matter (POM)**. This sinking POM is mainly in the form of defecation or dead plankton tissue and is often referred to as marine snow or detritus (Le Moigne, 2019). The gravitational settling is the dominant contributor to carbon export ($\sim$70%) (Boyd et al., 2019; Nowicki et al., 2022). The second export mechanism is the vertical migration pathway, which refers to the vertical migration of zooplankton (small heterotrophic plankton), both on diurnal and longer time scales. Zooplankton thereby transport organic carbon to depth, where they respire CO_2 or produce fecal pellets (Iversen, 2023). Physical transport is the third pathway and encompasses the export of **dissolved organic matter (DOM)** to the ocean interior. The physical transport mechanisms extend from submesoscale eddies to the overturning circulation (Lévy et al., 2013; Omand et al., 2015).
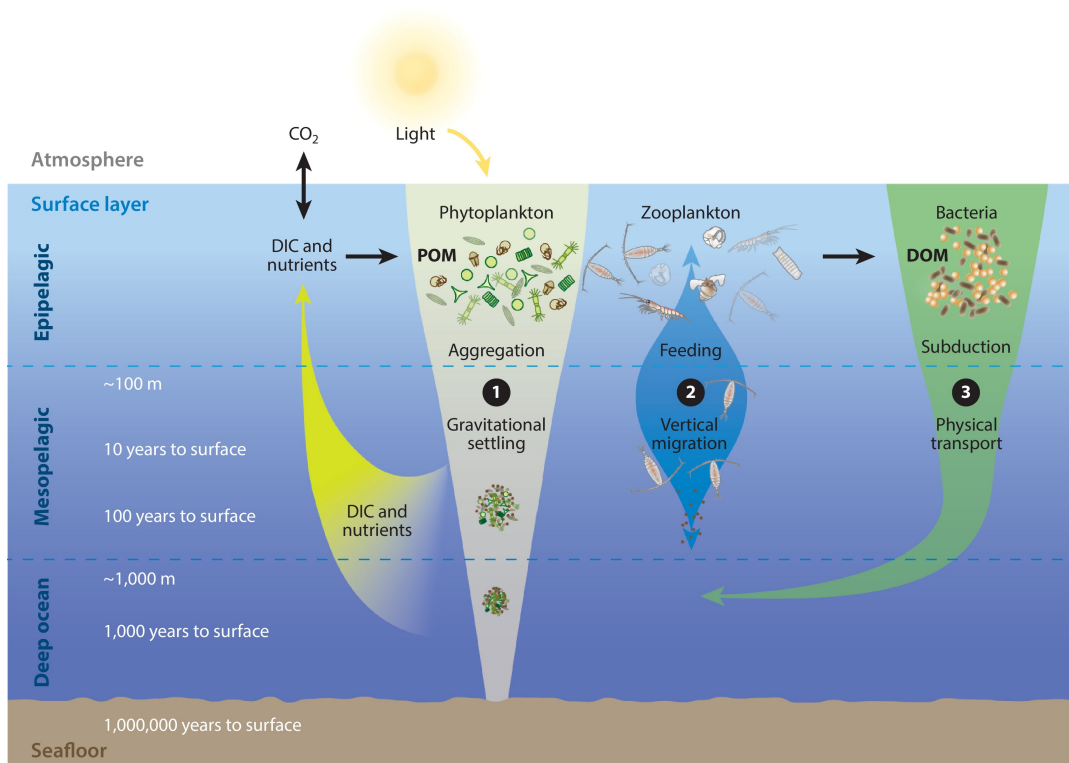
Figure 1.2: Overview of the biological carbon pump and the three main export mechanisms of organic matter by (1) gravitational settling, (2) migration and (3) physical transport. At depth the organic matter is remineralized into DIC and nutrients, and these inorganic elements are subsequently transported toward the surface again. The depth of remineralization determines the sequestration time of CO_2 in the ocean. On the left an indication of the sequestration times for different remineralization depths is displayed. Abbreviations are: dissolved inorganic carbon (DIC), particulate organic matter (POM) and dissolved organic matter (DOM). Figure from Iversen (2023).

Generally, the deeper the exported organic matter is converted back to CO_2, the longer the carbon

is stored in the ocean before it can return to the atmosphere, as can also be seen in Figure 1.2. Furthermore, the sequestration time is dependent on the (geographic) location of remineralization. This is because the downstream pathway of the remineralized exported carbon is crucial in determining the duration for which the carbon remains within the ocean. This pathway is determined by a combination of the wider (thermohaline) ocean circulation, localized physics and the mixed layer downstream (Baker et al., 2022). This results in different sequestration durations both within and between ocean basins (De Vries et al., 2012; Siegel et al., 2021). Figure 1.3 shows the geographical variability in the fraction of CO_2 released at different depth levels that remains in the ocean for a minimum of 100 years. Since the fluxes of organic matter decrease with depth (indicated by the tapering of the pathways in Figure 1.2), and so most of the organic matter is remineralized at smaller rather than larger depths, the BCP is mostly associated with storage timescales shorter than 100 years (Siegel et al., 2021, 2023). This characteristic is noteworthy for this study, as climate mitigation projects necessitate a minimum storage duration of 100 years.

Due to the complex biochemical, ecological and physical interactions, the biological carbon pump is variable in both space and time.
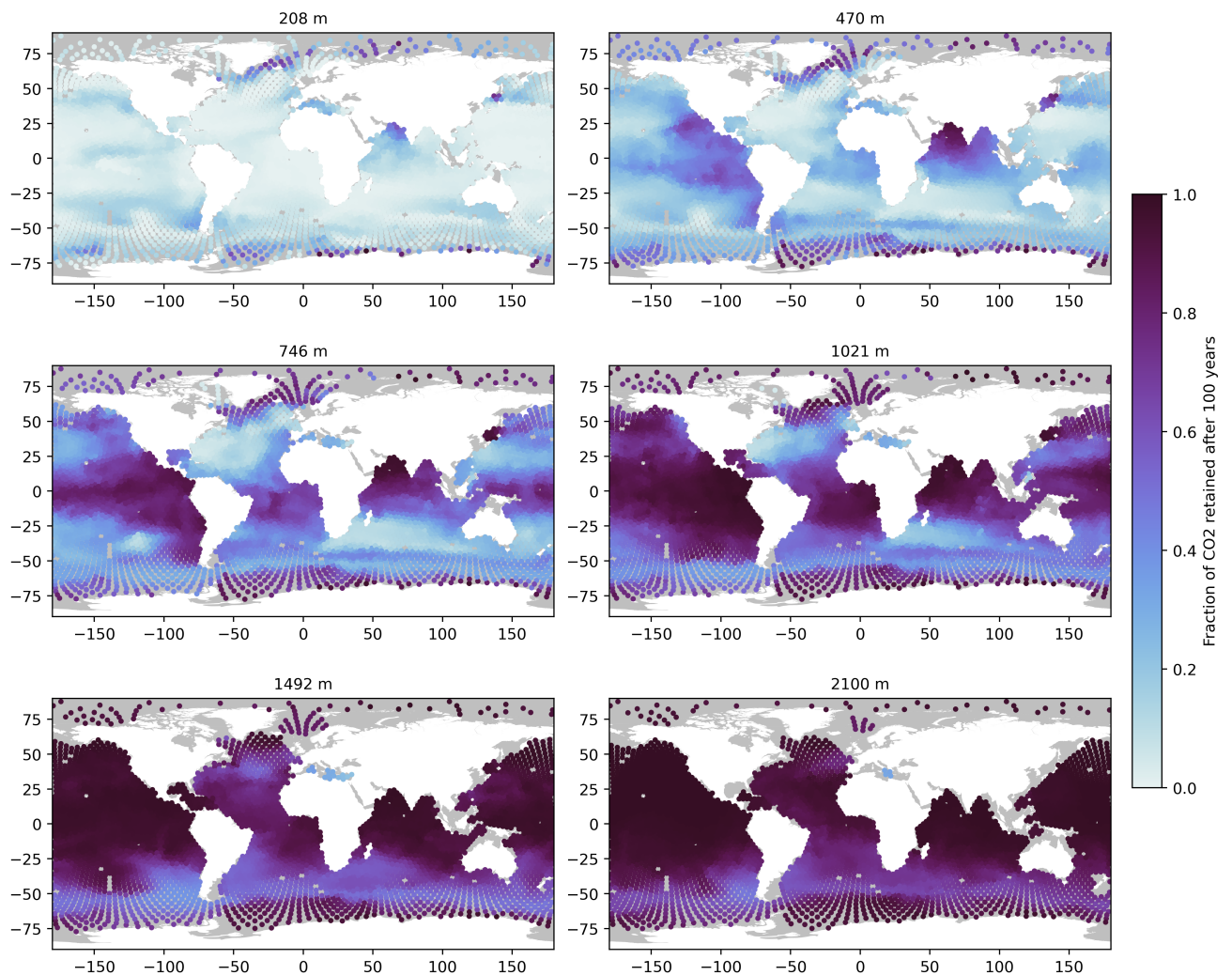
Figure 1.3: Maps of the fraction of CO_2 that remains in the ocean for a minimum of 100 years for different release (remineralization) depths. Obtained from Siegel et al. (2021).

1.1.4. Stimulating the biological carbon pump

This study considers a CDR technique that seeks to enhance the biological carbon pump. CDR techniques stimulating the BCP aim to increase the transfer of carbon to the ocean interior and thereby

the uptake of CO_2 in the surface ocean. As discussed in the previous subsection, the biological carbon pump is driven, and therefore limited, by the phytoplankton productivity in the ocean. This subsection therefore first explains what can limit the productivity of phytoplankton.

As mentioned in 1.1.3, phytoplankton grow by taking up CO_2 and photosynthesize this into organic matter. To do so, they require sunlight and nutrients. Important macronutrients are **nitrogen (N)** and **phosphorus (P)**, which are mainly utilised in the form of bio-available **nitrate (NO_3)** and **phosphate (PO_4)** (Paytan & McLaughlin, 2007; Webb, 2022). Redfield (1958) found that phytoplankton build their biomass with nearly constant C:N:P mole ratios of 106:16:1, which is referred to as the Redfield ratio. The flow of elements associated with phytoplankton photosynthesis, involving the uptake of C (CO_2), N (NO_3), and P (PO_4) in mole ratios of 106, 16, and 1, respectively, and the release of oxygen (O_2) in a mole ratio of 150, is depicted in Figure 1.4. Besides these two macronutrients, phytoplankton require trace (very small) amounts of **iron (Fe)** (C:Fe$\approx$ 100,000:1 mole ratio (Yoon et al., 2018)) and other micronutrients to perform photosynthesis (Schoffman et al., 2016).
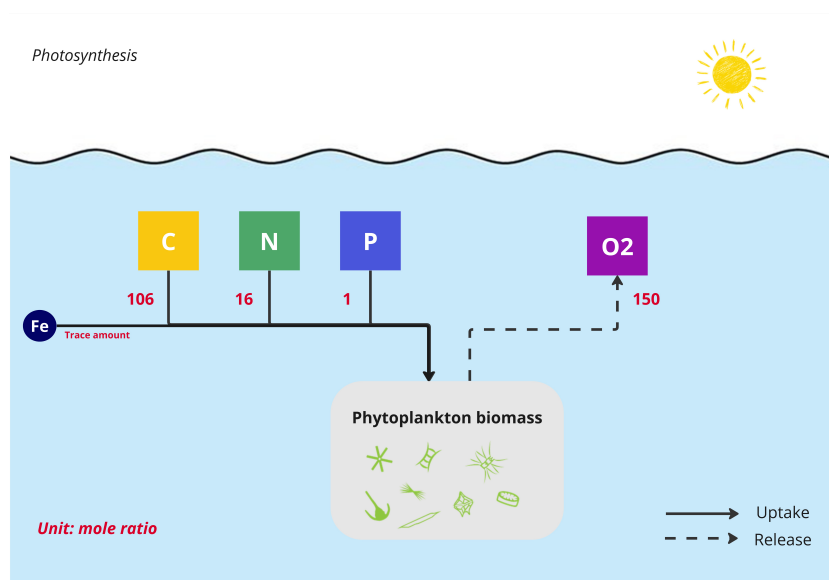
Figure 1.4: The flow of elements associated with the photosynthesis of phytoplankton. C (CO_2), N (NO_3), and P (PO_4) are taken up in mole ratios of 106, 16 and 1, respectively. O_2 is released in a mole ratio of 150.

The growth of phytoplankton is constrained by the most scarce resource among their required nutrients, this is called the first limiting nutrient. Carbon (CO_2) generally has a high concentration in seawater (Bristow et al., 2017; Sigman & Hain, 2012) and is therefore typically not a limiting factor for phytoplankton productivity. In contrast, the availability of other nutrients is crucial. Figure 1.5 illustrates the patterns of nutrient limitation, in which the circles identify locations where nutrient addition experiments have been performed. The inner circles represent the primary limiting nutrient. From the figure it is evident that large oceanic regions, mainly the Southern Ocean, are characterized by iron deficiency (red circles). Phytoplankton are therefore unable to fully utilise the available N and P in these regions. Conversely, in areas where sufficient iron is available, limitations can arise from either nitrogen or phosphorus, as their available concentrations deviate from the Redfield ratio. The substantial amount of green circles and the ratio of nitrate to phosphate concentration (background of the maps) observable in Figure 1.5, reveal that nitrogen is limiting in a significant portion of the ocean. In summary, the first limiting nutrient dictates phytoplankton growth capacity, resulting in the suboptimal utilisation of other nutrients, and different regions exhibit different nutrient constraints.

As the availability of sunlight remains beyond human influence, CDR techniques concentrate on altering nutrient concentrations in the oceanic environment. This study investigates ocean fertilization, a CDR technique frequently proposed to boost the biological carbon pump. The following subsection 1.1.5 introduces ocean fertilization and prior investigations, and elaborates on the particular nutrient

chosen for examination in this study.
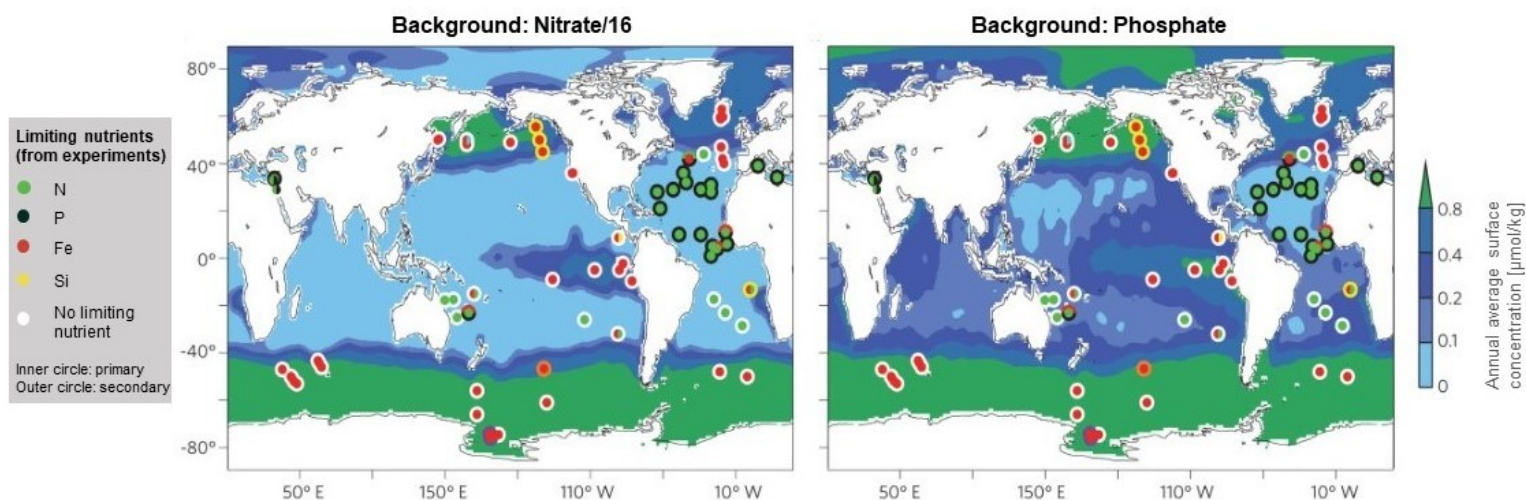
Figure 1.5: Patterns of nutrient limitation. The circles identify locations where nutrient addition experiments have been performed (both in situ and bottle experiments). The inner and outer circles represent the primary (addition of this nutrient led to instantaneous growth) and secondary limiting nutrient, respectively, that the addition experiments revealed. Divided inner circles indicate potentially co-limiting nutrients. The fill colours green, black and red represent N, P and Fe, respectively. White circles indicate that no secondary limiting nutrient was identified, the other fill colours are for this study not of relevance. The background colours of the left and right maps indicate the annual average surface concentrations $[\mu mol/kg]$ of nitrate and phosphate, respectively. For comparison, nitrate is scaled by the Redfield ratio (that is, divided by 16). Figure adapted from Moore et al. (2013).

1.1.5. CDR choice: ocean nitrogen fertilization

Ocean fertilization involves the addition of micro- or macronutrients to regions with limited availability of these nutrients. It therefore aims to enhance ocean productivity, subsequently the transfer of carbon to the deep sea and thereby the uptake of CO_2 in the surface ocean (National Academies of Sciences & Medicine, 2022).

Most scientific attention has been directed towards ocean fertilization with iron. The reason for the focus on iron fertilization is that only very small amounts are needed to stimulate phytoplankton growth. From 1990 to early 2000s, 13 iron fertilization experiments were performed (Yoon et al., 2018). These experiments demonstrated that phytoplankton biomass was indeed stimulated as a result of the fertilization, but the additional export of CO_2 to the deep ocean was not quantified. The results of these experiments and the potential negative environmental side effects were a topic of debate, especially since the public perceived ocean fertilization as interfering with nature. In 2013 an amendment was made to the London Protocol (a global treaty to protect the marine environment from pollution) to prohibit venture capitalists from performing ocean fertilization experiments, as well as other 'dumping' marine geoengineering practices (NOAA, 2022). Since then, scientific institutions have been mostly inactive in conducting new experiments due to the fear of negative publicity (Smetacek & Naqvi, 2008; Yoon et al., 2018).

Given the urgent need for carbon dioxide removal to meet the goals of the Paris Agreement, renewed attention is being directed towards ocean fertilization, as previously discussed in section 1.1.1. However, this thesis does not pursue the study of ocean iron fertilization. The primary reason for this is that areas suitable for this strategy, with the Southern Ocean being by far the largest (see Figure 1.5), are typically distant from continents and shipping routes. The geographical remoteness of these areas can present challenges in the practical delivery, hindering its scalability.

In this study the focus is shifted to macronutrient fertilization, which has received less attention in the scientific community (National Academies of Sciences & Medicine, 2022). Fertilization with phosphorous is undesirable, given the ongoing global concerns about the finite supply of phosphate which is

crucial for food production (Blackwell et al., 2019; McKie, 2023). Hence, attention is turned to ocean nitrogen fertilization.

Nitrogen is the first limiting nutrient in most surface waters (Tyrrell (1999), and Figure 1.5), and these regions are relatively proximate to continents and mobilisation routes. However, the potential for carbon dioxide removal through nitrogen fertilization remains a relatively unexplored research domain. The sole research conducted by Harrison (2017) left out the crucial aspect that most of the CO_2 exported through the BCP resurfaces within 100 years, and is therefore not directly useful in the evaluation of ocean nitrogen fertilization's CDR potential. Also, the study neglected relevant processes of ocean productivity. Furthermore, no single field experiment has taken place to date (Secretariat of the Convention on Biological Diversity, 2009; Williamson et al., 2022). This study thus serves as one of the initial efforts to quantify the carbon dioxide removal potential of ocean nitrogen fertilization.

Before discussing the specific objective of this study in 1.2, the following subsection (1.1.6) first elaborates on the marine nitrogen cycle. The ocean nitrogen cycle is accompanied by two stabilizing feedbacks capable of countering the intended outcomes of nitrogen fertilization (which is elevating the nitrogen concentration to increase organic matter production and export). These feedback mechanisms are thus elucidated below.

1.1.6. Ocean nitrogen cycle

The marine nitrogen cycle is probably the most complex biochemical cycle in the ocean (Gruber, 2008). The nitrogen cycle controls the availability of nitrate (the important bio-available nitrogen nutrient) and ocean productivity, and thus is linked to the fixation of atmospheric CO_2 and export of carbon from the ocean's surface (Zehr & Ward, 2002).

There are two processes in the marine nitrogen cycle of particular importance for this study: nitrogen fixation and denitrification. These two processes tend to stabilize the marine bio-available nitrogen inventory and therefore act as negative feedbacks in this cycle (Tyrrell, 1999). Nitrogen fixation converts nitrogen gas (N_2) into bio-available nitrogen (NO_3), while denitrification is the reverse process. The yellow (red) areas in the upper (lower) map of Figure 1.6 roughly indicate where nitrogen fixation (denitrification) occurs.
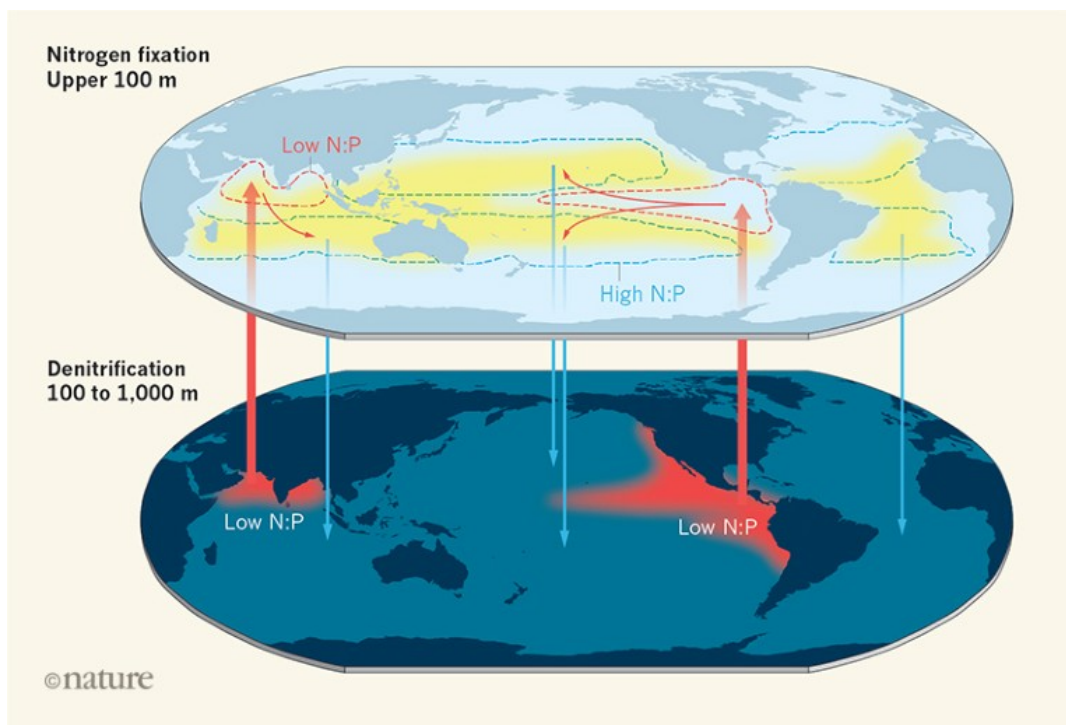
Figure 1.6: Regions where nitrogen fixation (yellow areas in the upper map) and water column denitrification (red areas in the bottom map) take place in the global ocean, figure from Gruber (2019).

Previous studies (Somes et al. (2016) and Tivig et al. (2021)) have simulated prolonged (>100 years) continuous global nitrogen additions from the atmosphere and rivers. These studies showed that this sustained positive nitrogen perturbation (N*) triggers these negative feedbacks within the nitrogen cycle. Despite the ongoing nitrogen influx, the global marine bio-available nitrogen inventory and NPP experienced only marginal increases in their simulations due to the counteracting effects of these nitrogen cycle processes. The upcoming subsections elaborate on the nitrogen fixation and denitrification processes and explain their offsetting feedbacks in response to the continuous nitrogen addition with the help of Figure 1.7, which illustrates both negative feedbacks.

Nitrogen fixation
In the ocean, a unique group of phytoplankton called diazotrophs has the ability to use and fix atmospheric N_2, producing bio-available nitrogen. This type of phytoplankton is therefore not limited by the amount of nitrate in the environment, but they do grow slower than 'ordinary' phytoplankton. Diazotrophs can therefore compete with these ordinary phytoplankton for nutrients in regions where N is depleted but where there is an excess of P (and Fe) (Gruber, 2008).
The feedbacks regarding nitrogen fixation are illustrated on the left side of Figure 1.7. Due to the ongoing addition of nitrogen, diazotrophs lose their competitive advantage (competitive exclusion). Hence, nitrogen fixation is decreased (this could be called a reduction in 'auto-fertilization'), which offsets (decreases) the nitrogen addition perturbation (N*). The studies found that nitrogen fixation provides an immediate offsetting feedback, as it rapidly decreases following the nitrogen addition.
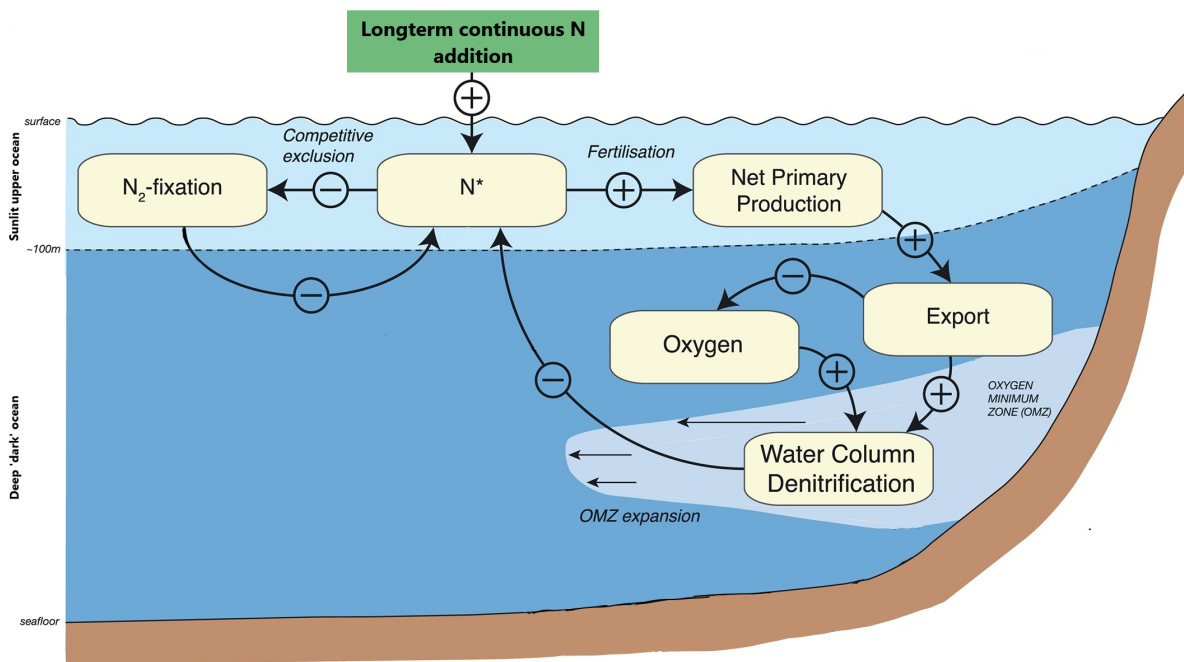
Figure 1.7: Schematic presentation of the negative feedbacks from the nitrogen cycle induced by the continuous addition of nitrogen. The addition leads to a positive (increased) perturbation of nitrogen (N*) that decreases the advantage of diazotrophs leading to a reduction of N_2 fixation. The positive N* also enhances net primary production and export. This results in an increase in water column denitrification. Both the reduced nitrogen fixation and increased denitrification lead to a reduction in nitrogen perturbation, thereby offsetting the addition. Figure adapted from Yang and Gruber (2016).

Denitrification
Fixed bio-available nitrogen is lost from the ocean by water column denitrification. This is a process that takes place instead of the aerobic remineralization (breakdown) of organic matter in low-oxygen (anaerobic) environments. Aerobic remineralization and denitrification and their associated flow of elements are schematized in 1.8a and 1.8b, respectively. With denitrification, nitrate is used instead of oxygen, and transformed back to N_2. Denitrification consumes approximately 7 mol of nitrate for every mole of organic nitrogen remineralized (Landolfi et al., 2013; Tyrrell, 1999). Consequently, bio-available

nitrogen is lost through denitrification.

The feedback that the prolonged nitrogen addition triggers is presented on the right side of Figure 1.7. The N addition stimulates NPP and export of organic matter. This increases the consumption of oxygen for organic matter remineralization (thus decreasing oxygen concentrations). Subsequently, oxygen minimum zones (OMZ) expand and water column denitrification increases. Thereby denitrification also reduces the N*. Denitrification is a slower operating offsetting feedback which increases gradually in the slowly expanding OMZs (Somes et al., 2016).

Denitrification can even overcompensate for the nitrogen perturbation, thereby acting as a 'positive' feedback. This is due to the chemical imbalance of the process, where 7 mol nitrate is consumed (lost) per mole nitrate remineralized (gained). Therefore, if nitrogen is deposited near oxygen minimum zones (in other words where denitrification occurs) and organic matter is produced from the external nitrogen input and exported, this can lead to a local net loss of bio-available nitrogen. Landolfi et al. (2013) called this the 'vicious cycle'.

(a) Aerobic remineralization
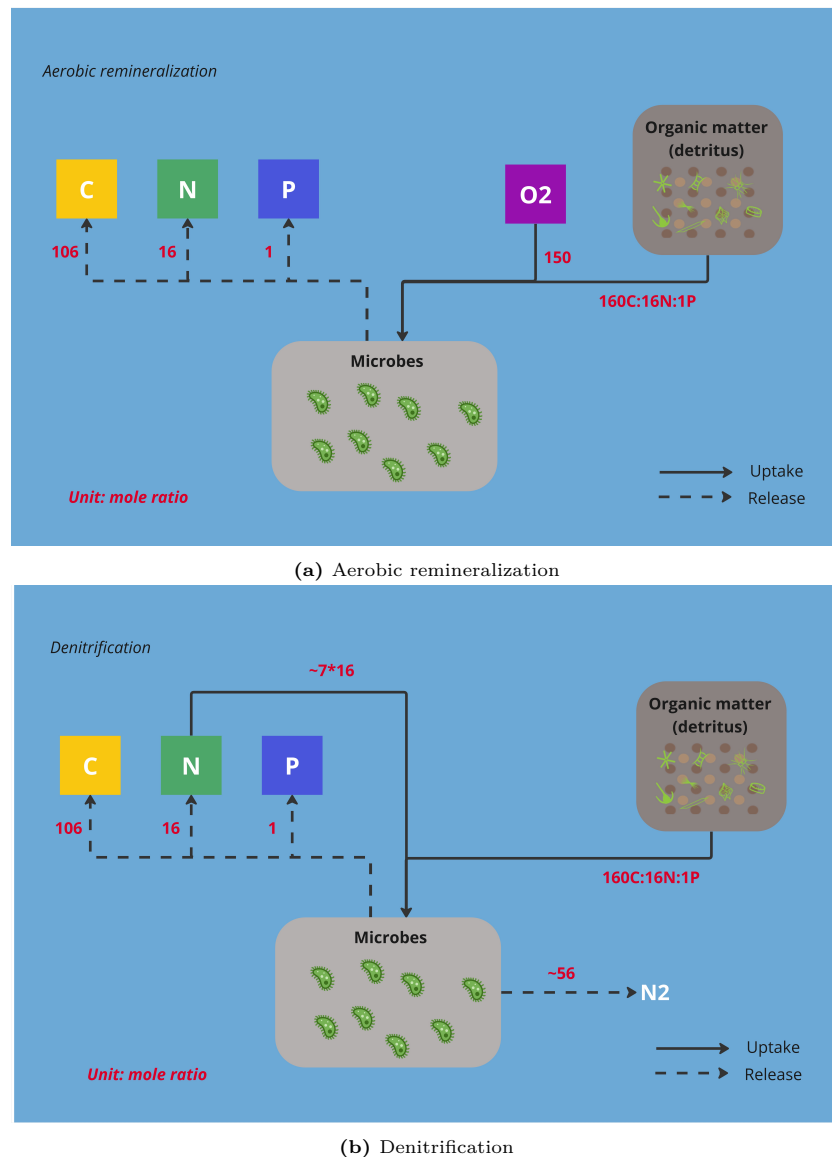
(b) Denitrification

Figure 1.8: The flow of elements associated with the aerobic remineralization and denitrification of organic matter. The red numbers denote the mole ratios of the flows.

When studying ocean nitrogen fertilization, it is crucial to take the (offsetting) feedbacks from nitrogen fixation and denitrification into account. Furthermore, Tivig et al. (2021) suggest that, because of these

processes and their feedbacks, research in the context of ocean nitrogen fertilization should focus on targeted short-term nitrogen additions.

1.2. Objective

As stated in 1.1.5, this research aims to provide an initial quantification of the CDR potential of ocean nitrogen fertilization. The focus is on evaluating both global-scale CDR efficacy and the viability of the strategy for commercial implementation. This study concentrates on one-off nitrogen fertilization, in other words a single pulse of nitrogen, a short term-addition as recommended by Tivig et al. (2021). For CDR assessment, only the long-term (>100 years) carbon storage resulting from a method is relevant (see 1.1.1). Although all fertilized nitrogen can, through multiple reuses, eventually contribute to the long-term storage of carbon (at the Redfield ratio), because of the urgency to meet the Paris Agreement there is a significant interest in assessing the amount of long-term carbon sequestration reached within a brief period after fertilization. In other words, to evaluate the amount of carbon exported during this short period that remains in the ocean for at least 100 years. In this thesis a time frame of 5 years is adopted, and so the focus is on the cumulative long-term carbon sequestration that can be achieved within 5 years after the addition of the nitrogen. Throughout the remainder of the study, this is predominantly denoted as long-term carbon sequestration achieved in 5 years, implying cumulative effects without explicit use of the term. The objective can therefore be formulated as follows:

> **To quantify the CDR potential of one-off ocean nitrogen fertilization achieved within a 5-year period following the fertilization.**

The objective of this thesis (determining the long-term carbon storage for the CDR potential), as well as the one-off fertilization and the possible nitrogen cycle offsetting (loss) feedbacks are illustrated in Figure 1.9. The exclusive transport mechanism of vertical eddy diffusion is elaborated on in 1.3.
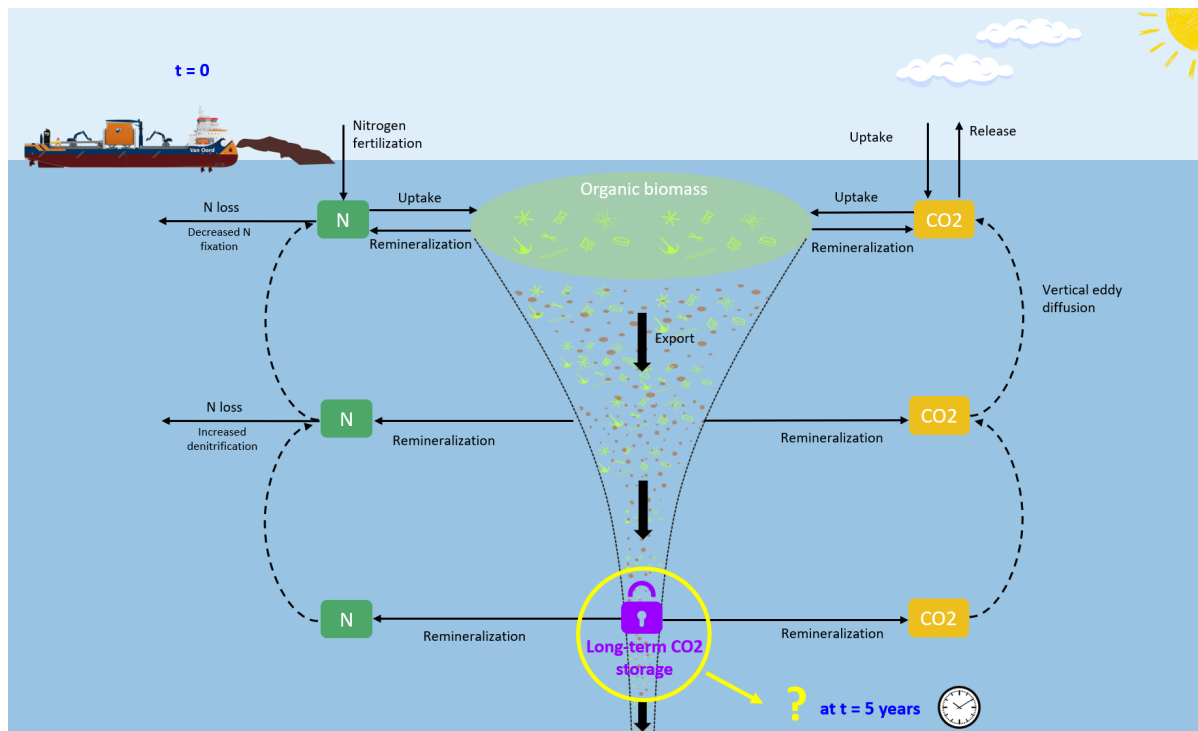
Figure 1.9: The one-off nitrogen fertilization process. The objective of this thesis, quantifying the long-term carbon storage 5 years after the fertilization event for determining the CDR potential, is indicated by the question mark. The possible offsetting (loss) feedbacks from the nitrogen cycle are also shown.

1.3. Scope and approach

The BCP is often modelled with a climate model on a global scale, comprising of a marine biochemical ecosystem module embedded in a three-dimensional (3D) general circulation model of the ocean, and an atmospheric model. Regarding the objective of this study and available time, this is considered unfeasible. In this study, an idealized **one-dimensional vertical (1DV)** model framework with an exclusive focus on the ocean is applied to reach the objective. The global ocean is divided into 1DV hexagonal columns for this framework. Inside a hexagon, vertical eddy diffusion is the sole ocean circulation mechanism. This physical model is structured by treating the stratified ocean as a three-layer system consisting of the surface mixed layer, the thermocline and the deep ocean, each with a constant eddy diffusivity. The surface mixed layer is characterized by the largest mixing, whereas the thermocline experiences reduced mixing, and slightly increased mixing can be found below the thermocline in the deep ocean. A marine ecosystem model is coupled to this physical model. The organic matter remineralization output of this ecosystem model is used, and post-processed to derive the long-term carbon sequestration resulting from the fertilization.

Before conducting any model simulations, regions need to be excluded that do not allow for the 1DV modelling. Besides, hexagons which are not of interest are filtered out, with the primary criterion being the exclusion of areas where nitrogen is not the first limiting nutrient. Attempts are made upfront to exclude regions where offsetting feedbacks from the nitrogen cycle are likely to occur, because these feedback can counterbalance the effect from the fertilization.

After filtering, the effect of the one-off nitrogen fertilization can be assessed by conducting various **fertilization simulations (FS)** and **baseline simulations (BS)**. In this study, a specific experimental plan for nitrogen fertilization is employed, designed as one-off (single pulse) nitrogen additions, where the nitrogen limitation in the mixed layer is fully replenished.

While the 1DV modelling approach can offer valuable insights into the CDR potential of one-off ocean nitrogen fertilization, it does come with certain limitations. Firstly, due to the nature of the 1DV model, certain ocean areas that might contribute to the CDR potential need to be excluded from the study. Additionally, the findings are constrained by the specific experimental design (primarily the amount of nitrogen applied during fertilization). Furthermore, concerning the regions (hexagons) that are included in model computations, the sequestration outcomes should be interpreted as a ballpark estimate due to the use of this idealized model. This suits the objective of the study: to derive an initial quantification of the CDR potential of one-off ocean nitrogen fertilization.

1.4. Research questions

To achieve the objective of this study, in light of the described scope, multiple research questions (steps) are formulated. First, the model framework with essential processes has to be set-up, as outlined in the first sub-question:

1. How to establish a 1DV model framework with the minimal processes of ocean productivity and the biological carbon pump to assess the carbon sequestration from ocean nitrogen fertilization?

Having developed the framework, the next step involves conducting fertilization experiments. To facilitate this, an experimental design plan must be established. The second sub-question is therefore as follows:

2. How to design the experimental set-up for the one-off nitrogen additions and associated simulations?

One facet of the objective is to assess the potential of one-off nitrogen fertilization as CDR strategy from a global perspective. This requires quantifying the global long-term carbon sequestration potential from the nitrogen fertilization. Consequently, the third sub-question is:

3. What is the global long-term carbon sequestration potential resulting from the nitrogen fertilization?

Field trials and initial implementation of one-off ocean nitrogen fertilization would start at specific locations, for which it is of interest to evaluate if the CDR strategy can be commercially viable. Consequently, these locations need to be identified. The selection of these locations is driven not only by their carbon storage potential but also by considerations of delivery costs and associated emissions. Hence, the fourth sub-question is:

4. To which locations is the delivery of the nitrogen energetically and economically viable?

1.5. Outline

This thesis has the following structure: the development of the 1DV model framework is provided in Chapter 2. The design of the nitrogen fertilization experimental plan and the required simulations are presented in Chapter 3. Chapter 4 describes the steps of simulation post-processing to obtain the long-term carbon sequestration as result from the nitrogen additions. In Chapter 5, the results from the nitrogen fertilizations are presented on a global scale. Locations to which the delivery of nitrogen is expected to be viable are identified in Chapter 6. Chapter 7 uses the results from Chapter 5 and 6 to examine the feasibility of one-off nitrogen fertilization as a global CDR strategy and for commercial implementation. Chapter 8 discusses the results and the limitations and implications of this study. Chapter 9 contains the conclusions and recommendations.

Part I

Materials and methods

2 | 1DV model framework development

The first step of this thesis is to set up an one-dimensional vertical (1DV) framework containing the minimal processes of ocean productivity and the BCP to simulate ocean nitrogen fertilization and to determine the resulting carbon storage from the fertilization. The set-up of this model framework is discussed in this chapter. In the upcoming section, the key components and set-up steps to establish the model framework are outlined.

2.1. Model framework components

An overview of all components and their connections required for the 1DV framework is presented in Figure 2.1. All aspects are briefly introduced below, and in detail in a section of this chapter or in one of the following chapters.
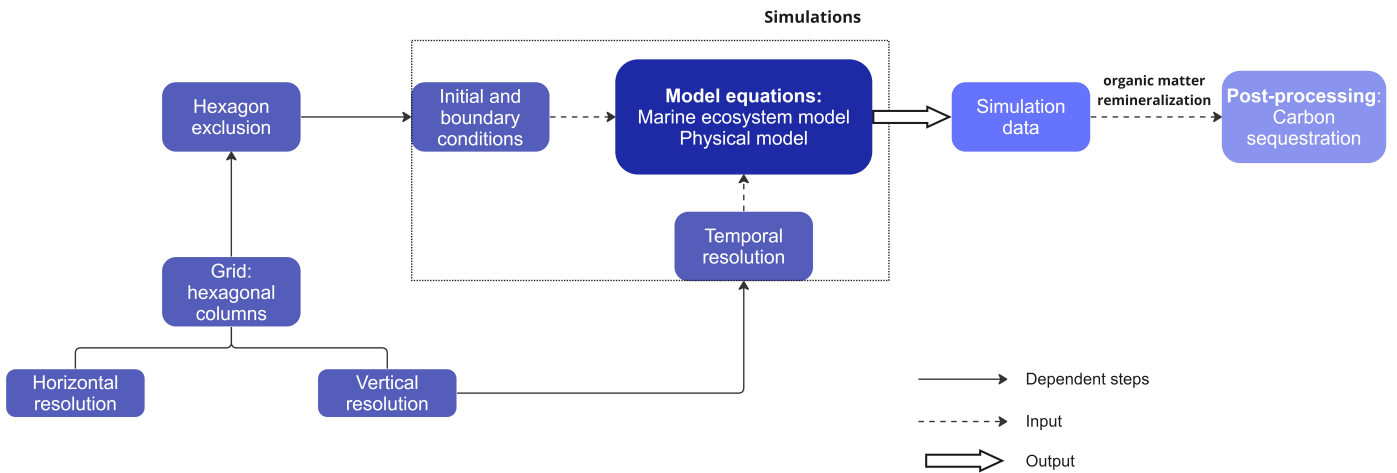
Figure 2.1: Overview of the model framework

In this research, the global ocean is discretized as a grid of *1DV hexagonal columns*. The arrangement of this grid, both horizontally and vertically, is detailed in section 2.2.

The models that need to be included and coupled are:

- *Marine ecosystem model*: A biochemical ecosystem model is used to simulate phytoplankton productivity, the transfer of carbon through the ecosystem, the gravitational sinking of organic matter to the ocean interior and the subsequent remineralization of the matter at depth. Since gravitational sinking represents the dominant export pathway, focusing solely on it suffices for the objective of this study. When modelling the BCP, marine ecosystems are often represented with NPZD models, which include compartments for nutrients (N), phytoplankton (P), zooplankton

(Z) and detritus (D). NPZD models differ in complexity, number of state variables within each compartment and their interactions (Kriest et al., 2010). This study requires an biochemical ecosystem model that includes the processes and feedbacks of nitrogen fixation and denitrification, as discussed in 1.1.6. Consequently, within the phytoplankton compartment, at least two distinct types must be included as state variables, namely 'ordinary' phytoplankton and diazotrophs. Furthermore, the nutrient compartment requires at least nitrogen and phosphorous. Some form of iron limitation has to be included, although this does not explicitly need to be as state variable.

- *Physical 1DV model*: The BCP is a continuous process which is sustained by the continuous (re)supply of nutrients to the euphotic zone (the upper sunlit layer of the ocean), as also illustrated in Figures 1.2 and 1.9. For this study, vertical eddy diffusion is the only included transport and consequently nutrient supply mechanism (section 1.3). This oceanic nutrient resupply is also crucial for simulating nitrogen fertilization, as a portion of the nitrogen can be recycled and reintroduced to the upper ocean. There it can be reused again for organic matter production, potentially contributing to the long-term storage of carbon as it might be exported to greater depths.

A description of all model equations is given in section 2.3.

Determining an appropriate *temporal resolution (time step)* is a necessary step in establishing the model framework, and presented in section 2.4.

Before any simulations are conducted with the model, it is necessary to *filter out hexagons* where the developed framework is inapplicable or which are not of interest to this study, this is discussed in section 2.5.

For the remaining hexagons, *initial and boundary conditions* are required. An overview of all used data sources and required processing is provided in section 2.6.

With the developed model framework different baseline and fertilization *simulations* are conducted. The experimental plan is presented in Chapter 3.

The final step involves *post-processing the simulation outcomes* to derive the *long-term carbon sequestration* as result from the fertilization. For this calculation the magnitude and depth of remineralized CO_2 (from organic matter) and sequestration time scale fractions obtained from the study of Siegel et al. (2021) are used. The post-processing, as well of the sequestration fractions from the respective study, are elucidated in Chapter 4.

2.2. Grid

For this study's 1DV framework, the global ocean is divided into hexagonal columns. The application of 1DV modelling signifies that the hexagonal columns do not interact with each other, as the modelling processes are exclusively confined to the vertical dimension. This implies that all model equations (as discussed in section 2.3) are applied to each hexagon separately. The reason behind choosing hexagons, the number of hexagons (horizontal resolution) and the vertical grid layers used are elaborated on below.

2.2.1. Horizontal grid definition

The global ocean is filled with hexagons using Uber's Hexagonal Hierarchical Spatial Index grid system H3. H3 is a grid system developed by Uber for visualizing and exploring spatial data. Utilising hexagons offers an advantage in that they possess a single distance between the centerpoint of a hexagon and its neighboring hexagons. This characteristic simplifies performing analyses and smoothing over gradients (Brodsky, 2018). The use of a hexagonal grid in this study is further supported considering that the results can potentially be implemented in Van Oord's Climate Risk Overview tool, which uses hexagons as well.

H3 supports sixteen resolutions. For this study resolution level 2 is used. This divides the global ocean into 4222 hexagons, with an average area of $87 \cdot 10^3$ km^2. This is similar to the horizontal resolution used in global climate models (Strandberg & Lind, 2021). Figure 2.2 shows the arrangement of the hexagonal grid. Not all the displayed hexagons are included in the simulations, hexagons where the

developed model is not applicable or hexagons that are not of interest are excluded (see section 2.5)
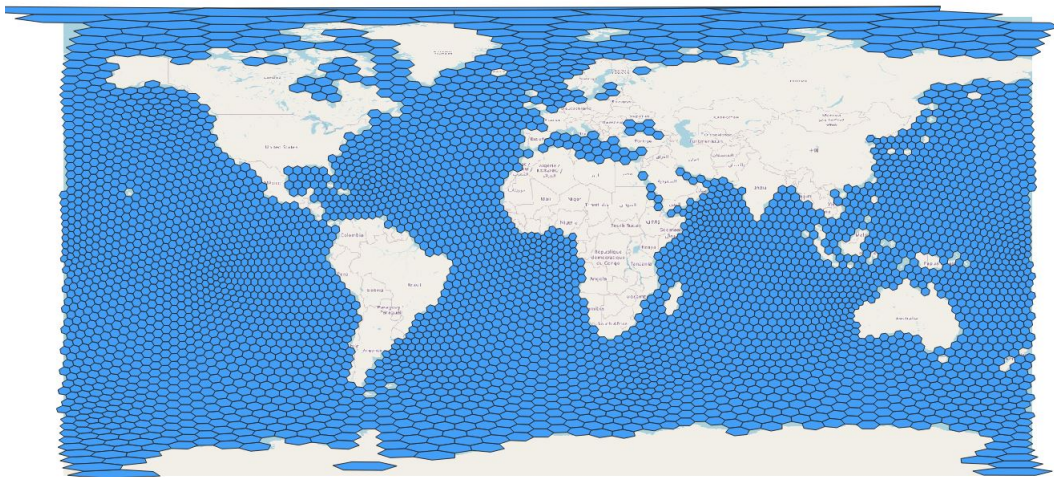
Figure 2.2: Map of the hexagonal grid

2.2.2. Vertical grid definition

The vertical grid used in this study has 40 layers, with a high resolution near the ocean surface and a decreasing resolution with depth. The first thirteen layers have a thickness of 10 m. This high surface resolution is useful for phytoplankton production modelling and facilitates an accurate presentation of the mixed layer and identification of the grid layers within. Beyond these surface layers, the subsequent layers exhibit a 20% increase in thickness compared to the layer directly above, until reaching a thickness of 550 m. From this depth onward, the layer size remains constant at 550 m. With this vertical layer configuration, the maximum depth extends slightly over 6000 m. The values of all state variables and boundary conditions are taken uniform in each layer.

2.3. Model equations set-up

This section presents the equations of the marine biochemical ecosystem and the physical model and their coupling.

2.3.1. Marine ecosystem model

It is chosen to use the biochemical ecosystem model of Keller et al. (2012). It is normally embedded in the ocean circulation model in the University of Victoria Earth System Climate Model (UVic ESCM). UVic ESCM is an earth system model of intermediate complexity. The ecosystem is therefore described more idealized than state-of-the-art models, but the model meets the requirements described in 2.1. It is also used already in many other nitrogen supply studies (e.g. Somes et al. (2016) and Tivig et al. (2021)).

The Marine biochemical ecosystem model consists of seven state variables: ordinary phytoplankton (P_O), nitrogen fixing phytoplankton (diazotrophs) (P_D), zooplankton (Z), sinking particulate detritus ($Detr$), the nutrients nitrate (NO_3) and phosphate (PO_4), and oxygen (O_2).
Each variable's concentration ($Conc$) varies (in each vertical layer) according to:

$$\frac{\partial Conc}{\partial t} = Tr + S \tag{2.1}$$

with Tr representing the transport term, which is discussed in section 2.3.2. S represents all source and sink terms. Equation 2.1 is solved applying the explicit Euler scheme.

The main unit of this biochemical model is mmol N m^{-3}, and all biological variables (P_O, P_D, Z and $Detr$) and are expressed in this unit. A schematic of the fluxes (sources and sinks, indicated by black arrows) of nitrogen between NO_3 and the biological variables is shown in Figure 2.3. These state

variables are presented with a square. N_2 is no state variable, therefore indicated by a circle. The nitrogen fertilization flux is also displayed. The (fixed) Redfield ratio links the C (carbon), N and P content of the biological variables and the exchanges with the inorganic variables (NO_3, PO_4, O_2), this concept is also illustrated in Figures 1.4 and 1.8.

Carbon dioxide is not an explicit state variable in this biochemical model, which is justified since CO_2 generally does not limit the productivity of phytoplankton, as already stated in 1.1.4. Consequently, an instantaneous and unlimited CO_2 supply and CO_2 absorption by the ocean (if needed) is assumed. Nevertheless, the export of carbon to the ocean interior and its release and storage at depth are the ultimate points of interest in this study. This export and release of CO_2 follows from the sinking and remineralization of the detritus (organic matter) multiplied by the Redfield C:N ratio ($R_{C:N}$). A schematic of the transfer of C through the ecosystem is displayed in Figure 2.4, which is the same as the fluxes of N (Figure 2.3) multiplied by the $R_{C:N}$. Since CO_2 is not a state variable (indicated by the circle), its total concentration in the environment is unknown. However, this model facilitates the quantification of additional CO_2 export, remineralization, and subsequent sequestration resulting from ocean fertilization, which is the objective of this thesis.
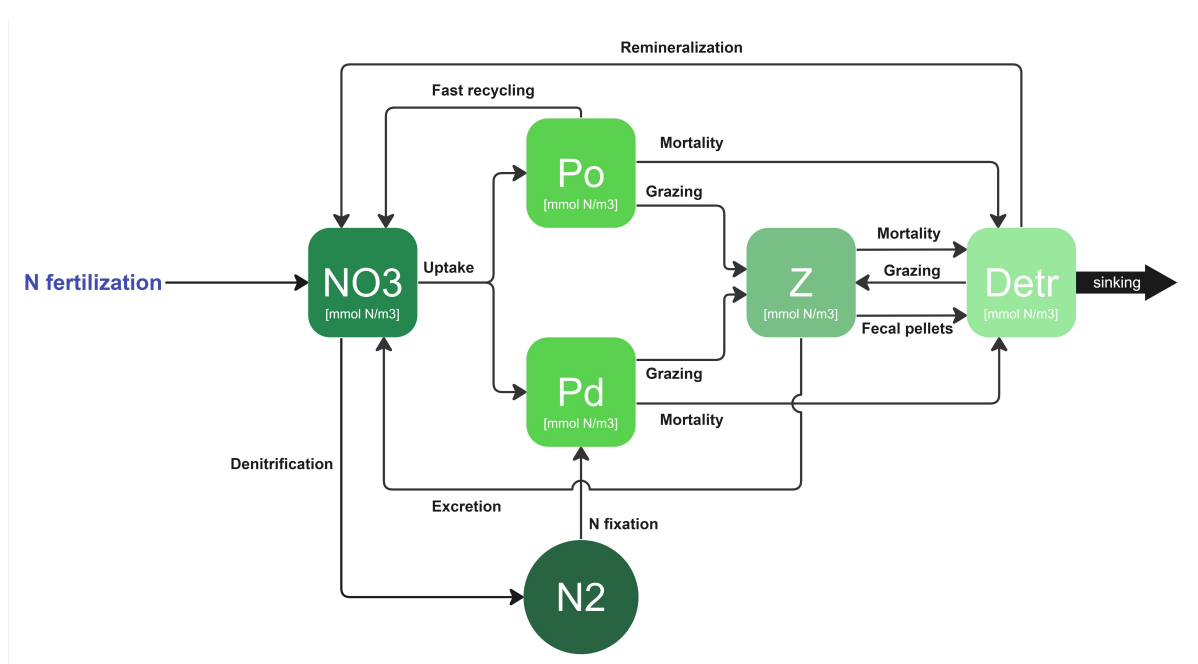
Figure 2.3: Schematic of the fluxes (black arrows) of nitrogen in the marine biochemical ecosystem model. The state variables (NO_3, P_O, P_D, Z and $Detr$) are indicated with a square. N_2 is not a state variable and therefore indicated with a circle. This study investigates nitrogen fertilization, and its input flux is illustrated. The (sinking) and remineralization of detritus are the simulation outputs eventually used in post-processing.
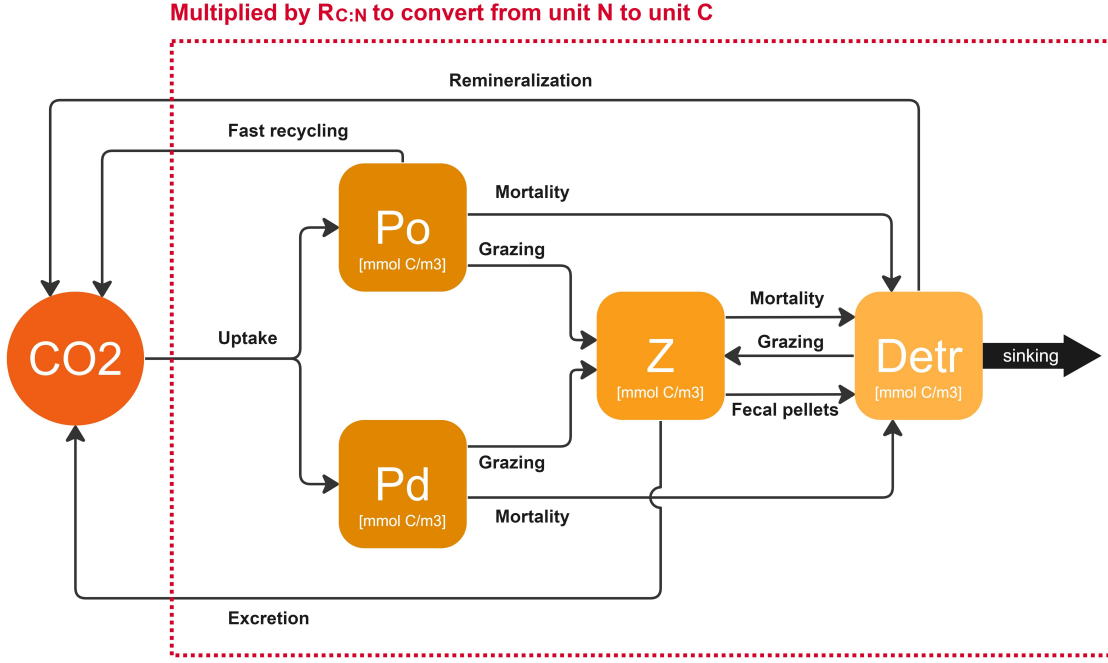
Figure 2.4: Schematic of the fluxes (black arrows) of carbon in the marine biochemical ecosystem model. The state variables (P_O, P_D, Z and $Detr$) are indicated with a square. CO_2 is no state variable and therefore displayed with a circle. The carbon content of the state variables and the fluxes follow from those in unit N, multiplied by the $R_{C:N}$ value. For the carbon sequestration quantification the (sinking and) remineralization of detritus are used from the simulation output.

In the following subsections, the source and sink terms (S) for each state variable are outlined.

Ordinary phytoplankton (P_O) and nitrogen fixing diazotrophs (P_D)
The source and sink terms for P_O and P_D are:

$$S(P_O) = J_O P_O - G_{P_O} - \mu_P^* P_O - m_{P_O} P_O \qquad (2.2)$$

$$S(P_D) = J_D P_D - G_{P_D} - m_{P_D} P_D \qquad (2.3)$$

Where growth (J), mortality (m) and fast recycling (μ_P^*) rates are described below, and losses from zooplankton grazing (G) in subsection 2.3.1.

The growth of ordinary phytoplankton is regulated by shortwave solar irradiance (I), nitrate limitation and phosphate limitation and is defined by the most limiting factor, as introduced in section 1.1.4:

$$J_O = min\left(\frac{J_O^{max} \alpha I}{[(J_O^{max})^2 + (\alpha I)^2]^{1/2}}, J_O^{max} \frac{NO_3}{k_N + NO_3}, J_O^{max} \frac{PO_4}{k_P + PO_4} \right) \qquad (2.4)$$

where the terms on the right-hand side are from left to right the growth rate determined by sunlight, nitrate concentration and phosphate concentration. The complete light (solar radiation) limited growth term is described in Appendix A. k_N and k_P are the half-saturation constants for nitrate and phosphate, respectively. The half-saturation constants represent the concentration at which half of the maximum intake rate is reached (Mulder & Hendriks, 2014). J_O^{max} is the maximum possible growth rate of phytoplankton, and is a function of temperature (T) and dissolved iron concentration (Fe) in the upper ocean layers (first $\sim$ 240 meter). Sufficient iron is required for the uptake and utilisation of nitrate and phosphate. However, iron cycling and interactions between iron and biology are complex which make it difficult to model. Keller et al. (2012) therefore use a global dissolved iron mask in the upper layers, which is an output from the model of Galbraith et al. (2010). Below the ocean surface, iron is not considered to be the most limiting factor and therefore not included in the calculation of J_O^{max}. The

formulation for the maximum growth rate of P_O is:

$$J_O^{max} = a \left(\frac{Fe}{k_{Fe}^{P_O} + Fe} \right) exp(T/T_b) \tag{2.5}$$

where a is a growth parameter and T_b is the e-folding temperature.

Diazotrophic phytoplankton grow according to the same principles as ordinary phytoplankton, but their growth rate is not limited by NO_3 concentrations, although they do take up nitrate if it is available. Diazotrophs can thereby fixate atmospheric N_2 and produce NO_3, this is discussed in section 1.1.6. Their maximum potential growth rate is however set with a handicap c_D (they grow slower than ordinary phytoplankton, as stated in 1.1.6) and they can only grow at temperatures higher than 15 °C. This gives the following formulations for P_D:

$$J_D = min \left(\frac{J_D^{max}\alpha I}{[(J_D^{max})^2 + (\alpha I)^2]^{1/2}}, J_D^{max} \frac{PO^4}{k_P + PO^4} \right) \tag{2.6}$$

$$J_D^{max} = c_D max[0, a \left(\frac{Fe}{k_{Fe}^{P_D} + Fe} \right) (exp(T/T_b) - 2.61)] \tag{2.7}$$

Phytoplankton are lost due to non-grazing mortality, parameterized using a mortality rate (m), and from fast remineralization. Fast remineralization implicitly accounts for the consumption by bacteria (microbial loop), and is temperature dependent: $\mu_P^* = \mu_{P,0}^* exp(T/T_b)$.

Zooplankton (Z)
Zooplankton function as intermediaries within the food chain, facilitating the energy transfer between phytoplankton (primary producers) and larger predators (U.S. Environmental Protection Agency, 2023). Zooplankton are heterotrophic organisms, meaning they cannot produce their own food. Their population grows by feeding (grazing G) on phytoplankton, detritus and itself. The loss terms include predation from higher trophic levels ($m_Z Z^2$) and self predation (grazing on itself):

$$S(Z) = \omega(G_{P_O} + G_{P_D} + G_{Detr} + G_Z) - m_Z Z^2 - G_Z \tag{2.8}$$

All grazing terms are scaled with a growth efficiency coefficient (ω). Grazing of each food source is calculated using a Holling 2 function. A maximum grazing rate (μ_Z^{max}) is scaled by the relative food preference ψ_X (where X is the food source), the total prey population and a half-saturation constant for grazing k_{graze} (2.9). The sum of all the preferences has to be 1.

$$G_X = \mu_Z^{max} Z \frac{\psi_X X}{\psi_{P_O} P_O + \psi_{P_D} P_D + \psi_{Detr} Detr + \psi_Z Z + k_{graze}} \tag{2.9}$$

The maximum potential grazing rate is a function of a maximum grazing rate at 0 °C, seawater temperature (T) and oxygen concentration (O_2). Grazing is limited when temperatures exceed 20 °C and under hypoxic conditions:

$$\mu_Z^{max} = \mu_Z^\theta max \left[0, [0.5(tanh(O_2 - 8 \quad mmol \quad m^{-3}) + 1)] b^{c*min(20°C,T)} \right] \tag{2.10}$$

Particulate detritus ($Detr$)
Particulate detritus is the collective name for non-living organic matter that can sink to the deeper ocean. CO_2, locked in detritus, is exported from the surface ocean to the ocean interior. In this study, the sinking of detritus is the only included export mechanism of the BCP (export mechanism 1 from Figure 1.2).

The source and sink terms for sinking particulate detritus are:

$$S(Detr) = (1 - \gamma)(G_{P_O} + G_{P_D} + G_{Detr} + G_Z) + m_{P_O} P_O + m_{P_D} P_D + m_Z Z^2$$
$$- \mu_D Detr - G_{Detr} - w_D \frac{\partial Detr}{\partial z} \tag{2.11}$$

Detritus is generated by zooplankton fecal pellet production and mortality among the three classes of plankton (P_O, P_D, Z). γ represents the assimilation efficiency coefficient of zooplankton. The grazing rates multiplied with $(1 - \gamma)$ therefore represent the fecal pellet production. Detritus is lost by remineralization (μ_D), grazing and export (sinking) to the deeper ocean layers. Remineralization is the breakdown of the organic detritus into the inorganic variables. It therefore returns the N and P content of the detritus to NO_3 and PO_4 and releases CO_2. The remineralization rate is dependent on temperature and oxygen concentration:

$$\mu_D = \mu_{D0} exp(T/T_b)[0.65 + 0.35 tanh(O_2 - 6 \ mmol \ m^{-3})] \tag{2.12}$$

Detritus sinks to the ocean interior with a sinking speed $w_D = w_{D,0} + m_w z$, where $w_{D,0}$ is the sinking speed at the surface ocean. The sinking speed increases linearly with depth. This is due to the aggregation of detritus particles (Brewin et al., 2021; Christina & Passow, 2007). The sinking term $w_D \frac{\partial Detr}{\partial z}$ is approximated by $export - import$, where the $import$ is the export of the layer above. The export is determined by $export = w_D \frac{Detr}{\Delta z_{layer}}$.

Phosphate (PO_4)
The phosphate concentration per grid layer changes according to:

$$S(PO_4) = (\mu_D Detr + \mu_P^* P_O + (\gamma - \omega)(G_{P_O} + G_{P_D} + G_{Detr} + G_Z) - J_O P_O - J_D P_D)R_{P:N} \tag{2.13}$$

The source terms include the remineralization of detritus, bacterial consumption of ordinary phytoplanklton and excretion by zooplankton. The latter is represented by the term $(\gamma - \omega)$ multiplied by the grazing rates. Excretion is the fraction of grazing zooplankton use for their metabolism. The sink terms include the use of phosphate by the two phytoplankton classes for their growth (NPP). Since all biological variables are expressed in mmol N m^{-3}, they are scaled by the molar Redfield P:N ratio of organic matter ($R_{P:N}$)

Nitrate (NO_3)
The source and sink terms for nitrate are:

$$\begin{aligned} S(NO_3) = (\mu_D Detr + \mu_P^* P_O + (\gamma - \omega)(G_{P_O} + G_{P_D} + G_{Detr} + G_Z) \\ - J_O P_O - u_{NO_3} J_D P_D) - denitrification \end{aligned} \tag{2.14}$$

where $u_{NO_3} J_D P_D$ represents the nitrate consumption of diazotrophs for their production, here $u_{NO_3} = \frac{NO_3}{k_N + NO_3}$. This demonstrates that P_D only take up nitrate when it is available, but as already stated nitrate does not limit their growth.
Denitrification (water column) is a loss term for nitrate in which NO_3 is used for the remineralization of organic matter instead of O_2 in suboxic (oxygen depleted) waters, as explained in 1.1.6. The denitrification is parameterized by:

$$denitrification = 0.8 r_{sox}^{NO_3} O_{2,consumption} \tag{2.15}$$

Denitrification consumes nitrate at a rate of 80 % the oxygen equivalent rate, as nitrate is a more efficient electron acceptor than oxygen.
In equation 2.15, $r_{sox}^{NO_3}$ is equal to: $0.5[1 - tanh(O_2 - 5 \ \ mmol \ \ m^{-3})]$.
This mathematical formulation indicates that at an oxygen concentration of 5 mmol m^{-3} the breakdown of organic matter occurs equally between aerobic remineralization and denitrification. There is complete aerobic remineralization, no denitrification, above ~ 8 mmol m^{-3}.

Oxygen (O_2)
Photosynthesis produces oxygen, while respiration and remineralization consume oxygen. The rate of oxygen production and consumption is equal to the rate of phosphate consumption and remineralization, respectively, multiplied with a molar $R_{O:P}$ ratio. The consumption of oxygen is inhibited in suboxic waters, as already explained in the previous subsection. This gives the following equation for the changes in O_2 concentration:

$$S(O_2) = F_{sfc} - S(PO_4)R_{O:P} r_{sox}^{O_2} \tag{2.16}$$

where $r_{sox}^{O_2} = 0.5[tanh(O_2 - 5 \quad mmol \quad m^{-3}) + 1]$ and F_{sfc} is the oxygen exchange with the atmosphere. In the UVic ESCM this exchange is calculated according to Wanninkhof (1992), using a transfer velocity and the partial pressures of O_2 in the atmosphere and the ocean surface layer (Weaver et al., 2001). Since the model framework does not contain an atmospheric component unlike UVic ESCM, it is not possible to formulate F_{sfc} using this relation. To prevent unrealistically high concentrations of oxygen in the surface ocean, where oxygen production generally exceeds consumption and exchange across the thermocline is limited, it is necessary to parameterize the exchange with the atmosphere. This is done by implementing an efflux term in the surface grid layer. This efflux term is parameterized based on the solubility of dissolved oxygen in seawater as a function of temperature (T) and salinity (S). The oxygen saturation concentration in mmol m^{-3}, taken from Benson and Krause Jr (1984), is:

$$Conc_{O_2,sat} = exp\left[-135.90205 + \frac{1.575701 \cdot 10^5}{(T + 273.15)} - \frac{6.642308 \cdot 10^7}{(T + 273.15)^2} + \frac{1.243800 \cdot 10^{10}}{(T + 273.15)^3} - \frac{8.621061 \cdot 10^{11}}{(T + 273.15)^4}\right.$$
$$\left. -S \cdot (0.020573 - \frac{10.754}{(T + 273.15)} + \frac{2140.7}{(T + 273.15)^2}\right]$$

(2.17)

where T is temperature and S is salinity. When the oxygen concentration in the surface grid layer is larger than the saturation concentration, the oxygen concentration is reduced to this saturation value, which simulates the efflux of oxygen to the atmosphere.

In order to prevent negative concentrations, outgoing fluxes are set to 0 whenever a variable falls below a minimum concentration of $5 \cdot 10^{-12}$ mmol N m^{-3}. All model parameters used in the equations of this section are listed in Table B.1. A few of these parameters are from the study of Yao et al. (2019), who calibrated (and improved) the parameters from Keller et al. (2012).

2.3.2. Physical model

Tr in equation 2.1 represents the transport of the variables. The transport is primarily needed to simulate the supply of nutrients to the euphotic zone to support phytoplankton production. As discussed in section 1.3, this study only includes the transport of the state variables due to vertical eddy diffusion. According to Fick's law, the flux of a substance (with concentration *Conc*) due to vertical eddy diffusion is:

$$F_{eddy-diff} = -D\frac{\partial Conc}{\partial z}$$

(2.18)

where D is the vertical eddy diffusivity [m^{2}s^{-1}]. Fick's law describes the movement of particles from a region of high concentration to a region of lower concentration. The diffusion equation that describes the rate of change of concentration is:

$$\frac{\partial Conc}{\partial t} = -\frac{\partial}{\partial z}F_{eddy-diff} = \frac{\partial}{\partial z}\left(D\frac{\partial Conc}{\partial z}\right)$$

(2.19)

Equation 2.19 is approximated using the forward Euler finite volume method:

$$\frac{Conc_k^{n+1} - Conc_k^n}{\Delta t} = \frac{D_{k+\frac{1}{2}}}{h_k}\frac{Conc_{k+1}^n - Conc_k^n}{h_{k+\frac{1}{2}}} - \frac{D_{k-\frac{1}{2}}}{h_k}\frac{Conc_k^n - Conc_{k-1}^n}{h_{k-\frac{1}{2}}}$$

(2.20)

where n is the time step and k is the grid layer. Figure 2.5 shows an illustrative example of the grid representation and layer terminology. $D_{k+\frac{1}{2}}$ ($D_{k-\frac{1}{2}}$) is the average of the diffusivities of layers k and $k + 1$ (k and $k - 1$).
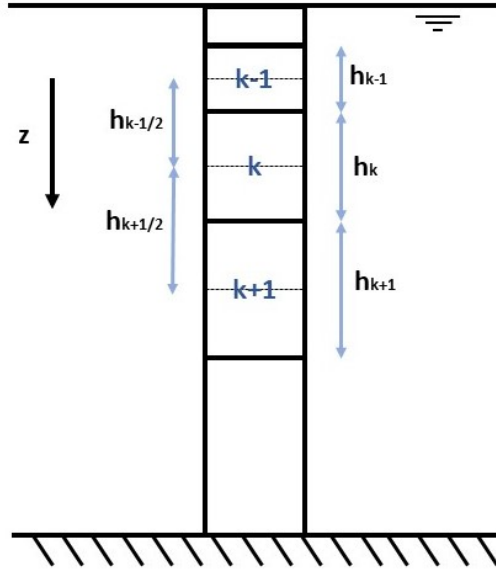
Figure 2.5: Illustrative example of the grid representation and layer terminology. The number of vertical layers is not the actual number of layers used in the model.

Eddy diffusivity exhibits significant variability in both time and space. A highly idealized modelling approach (as in e.g. Lohmann et al. (2013)) is to consider the stratified ocean as a three-layer system: the surface mixed layer, the thermocline and the deep ocean. The surface mixed layer is the uniform upper ocean region and undergoes the most substantial mixing due to influences such as wind, heat fluxes, and evaporation. In the thermocline, rapid temperature decline with depth creates stable stratification. The thermocline therefore experiences the lowest mixing rates. In the deep ocean the mixing is again slightly increased. The depth of each layer depends on the season and geographic location (latitude), with determination for each hexagon based on oceanographic conditions, as further discussed below (2.3.2). To each of the three layers a constant eddy diffusivity is assigned, requiring an assessment of these diffusivity values. The values for each layer are discussed in 2.3.2.

Layer boundaries
The depth of the mixed layer is retrieved from the World Ocean Atlas (WOA) (World Ocean Atlas, 2018). WOA determines the mixed layer depth (MLD) with a density threshold, based on the change in potential density from 10 meters depth (NOAA National Centers for Environmental Information, 2021). The thermocline starts at the bottom of the mixed layer. In this three-layer modelling approach, the thermocline is used rather than the pycnocline. This choice is justified as temperature predominantly governs density in most oceans (Fiedler, 2010; Romero et al., 2022). The definition of the bottom of the thermocline is based on Chu and Fan (2019), which utilises the temperature difference between the mixed layer and the deep ocean, as illustrated in Figure 2.6. The depth at which there is a 70% temperature difference compared to the temperature in the mixed layer is considered as the thermocline bottom. Temperature profiles for each season from WOA are used for the determination of the thermocline bottom (section 2.6). Although this estimation provides a rough approximation, it is deemed satisfactory, particularly given the relatively coarse resolution of the employed vertical grid in the ocean interior (as elaborated in 2.2). The third layer, the deep ocean, extends from the bottom of the thermocline to the ocean floor.
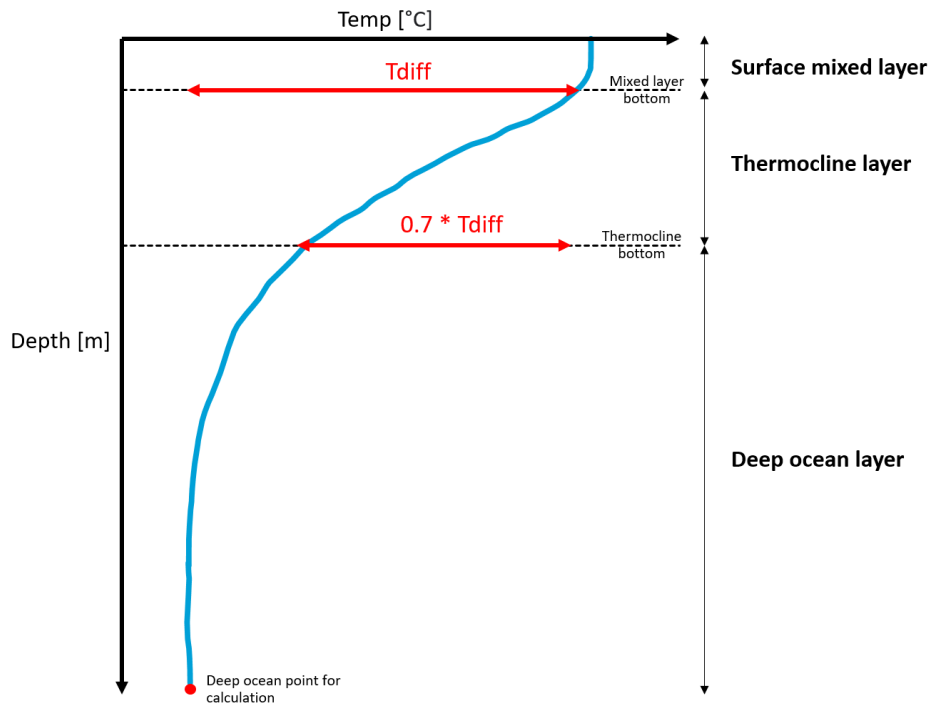
Figure 2.6: Illustrative example to elucidate the criterion for the thermocline bottom. The thermocline bottom is assumed to be at the depth where the temperature reaches 70% of the temperature difference (Tdiff) the between mixed layer and the deep ocean.

For this physical model, each of the (40) vertical grid layers need to be assigned to their respective oceanic layer (surface mixed layer, thermocline layer or deep ocean layer). To achieve this, the two grid layers with their (deeper) boundary closest to the surface mixed layer and thermocline bottom, respectively, are identified. Subsequently, the vertical grid layers are divided accordingly. An example of the three-layer partition can be seen in Figure 2.7, in which the green, pink and blue parts represent the mixed layer, thermocline and deep ocean, respectively.
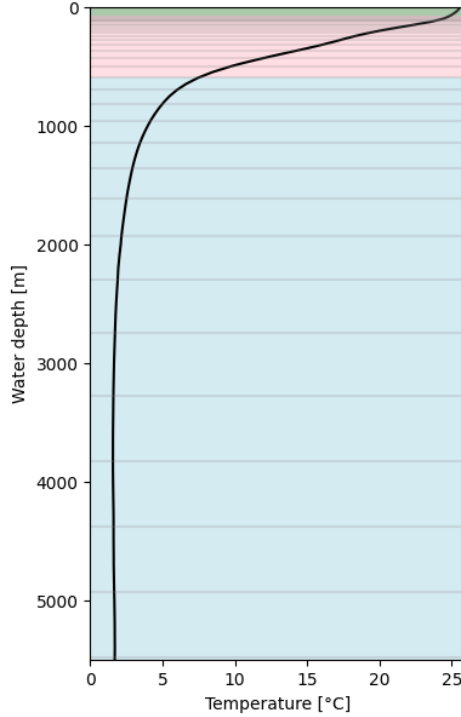
Figure 2.7: An example of the three ocean layer partition, with the surface mixed layer (green), thermocline layer (pink) and deep ocean layer (blue) based on a temperature profile (black line) at 19.5 °N, 126.3 °E in the winter season (January-March). Horizontal gray lines represent the vertical grid layer boundaries

Eddy diffusivities

Determining the appropriate mixing value for each of the three ocean layers poses a challenge. Vertical eddy diffusivities exhibit high variability, both spatially and temporally, and the available measurements are limited, sparse, and often indirect. Eddy diffusivities in the mixed layer (D_{ML}) can range from 10^{-5} to 10^{0} m^{2}s^{-1}, in thermocline (D_{thermo}) from 10^{-7} to 10^{-3} m^{2}s^{-1} and in the deep ocean (D_{deep}) from 10^{-6} to $5\cdot10^{-3}$ m^{2}s^{-1} (Jurado et al., 2012; Lohmann et al., 2013). The global average D_{ML}, D_{thermo} and D_{deep} are $\mathcal{O}(10^{-3})$, $\mathcal{O}(10^{-5})$ and $\mathcal{O}(10^{-4})$ m^{2}s^{-1}, respectively (Waterhouse et al., 2014).

In the simulations, 10^{-3} m^{2}s^{-1} and 10^{-4} m^{2}s^{-1} are used as D_{ML} and D_{deep}, respectively. A range of eddy diffusivities are used for D_{thermo} to account for some uncertainty and yield information on the sensitivity. This is elaborated on in Chapter 3.

Relative importance of detritus transport mechanisms

For all state variables except detritus, diffusion is the only transport mechanism. In the case of particulate detritus, it can also sink into the deeper ocean. To identify the relative importance of the sinking versus the diffusion of detritus, the Péclet number is analysed. The equation for the dimensionless Péclet number is (Rapp, 2017):

$$Pe = \frac{sinking\ transport\ rate}{diffusive\ transport\ rate} = \frac{Lw}{D} \tag{2.21}$$

where L is the characteristic length scale, for which the grid layer thicknesses are used, w is the sinking velocity and D is the diffusivity. All these parameters are variable in depth. The surface grid layer is characterized by the smallest Péclet number, which is attributed to its large (mixed layer) eddy diffusion and lowest sinking velocity. In this layer, the Pe is in the order of $\mathcal{O}(10^5)$. Therefore, particulate detritus exhibits negligible diffusion. For this reason, and to avoid the need for an excessively fine grid resolution (Zijlema, 2021), diffusion of detritus is neglected.

2.3.3. Verification
To ensure that the implementation of the model is correct, different verification tests are performed and functions are included. These are summed up below:

- Ecosystem function tests: during these tests model parameters are given a very high or low value to qualitatively evaluate if the fluxes and dependencies between model variables are set up correctly. *Outcome*: these tests revealed the model equations are set up correctly.
- Conservation: nitrogen (taking into account sources and sinks from N fixation and denitrification, respectively) and phosphorus needs to be conserved at all times. To ensure this, conservation functions are built in the model that calculate the total amount of nitrogen and phosphorus in the system at each time step and compare it with the amount of N and P, respectively, at t = 0. The amount of nitrogen in the system may change because of N fixation or denitrification, but these processes are taken into account in the conservation calculations. With these conservation checks it can evaluated that the fluxes are set up correctly. *Outcome*: nitrogen and phosphorus were conserved at all times during all performed simulations, indicating the correct set-up of the fluxes.
- Negative values: even though outgoing fluxes are set to 0 if a variable falls below the minimum concentration, small negative values can still occur due to integration and the diffusion scheme. A function is implemented to monitor the occurrences of negative concentrations throughout a simulation. *Outcome*: the model variables exhibit negative concentrations in fewer than 0.001% of their total states during simulations (across all moments in time and points in space), which is deemed acceptable.

2.4. Temporal resolution
The time step for the biochemical model follows from the detritus sinking and is determined using the Courant number, which has to be smaller than 1. The expression for the Courant number is (Zijlema, 2021):

$$C = \frac{w\Delta t}{\Delta h} \tag{2.22}$$

with velocity w, time step Δt and spatial resolution Δh. Since this study uses an irregular vertical grid, for each of the 40 layers the corresponding sinking velocity of detritus (see 2.3.1) and layer thickness are used in the expression above. This analysis indicates that a time step of 8 hours is adequate.

A Δt of 8 hours is also sufficient considering the stability criterion of the diffusion equation:

$$\Delta t \leq \frac{\Delta h^2}{2D} \tag{2.23}$$

The conjunction of the largest eddy diffusivity (10^{-3} m^{2}s^{-1}) and smallest layer thickness (10m) is used to validate this time step.

2.5. Exclusion of hexagons from model computations
Before conducting model computations, different filtering processes are applied to the 4222 hexagons to exclude those not relevant to the study or where the developed model is inapplicable. Hexagons are considered irrelevant if nitrogen is not the first limiting nutrient, if they have a small water depth, contain a substantial land portion or are situated in impractical delivery regions. Hexagons where the horizontal surface transport of nutrients is expected to be dominant do not allow for 1DV modelling and must be excluded. Additionally, given the feedbacks from the nitrogen cycle can counteract the fertilization effects, the exclusion of these areas is also being considered in this section.

Each filtering step is elaborated upon below. The outcomes and additional figures of each individual filtering step are presented in Appendix C, and the combined outcome is presented in Figure 2.8.

2.5.1. Nitrogen not first limiting nutrient
Hexagons for which nitrogen is not the first limiting nutrient are not of interest for this study, since fertilizing these areas with nitrogen does not lead to the enhancement of the BCP and thus no additional

carbon sequestration. Iron is likely to be the first limiting nutrients for phytoplankton productivity in ocean regions having an annual average surface nitrate concentration larger than 4 μM (Okin et al., 2011). The nitrate concentration at 10m is used for this filtering process. This leads to the exclusion of hexagons in the North Pacific and Atlantic Ocean, the Equatorial Pacific and all hexagons in the Southern Ocean, as presented in Figure C.1. Examining Figure 1.5 again reveals that the applied filtering criterion effectively excludes regions characterized by an iron deficiency.

The annual P to N concentrations in the upper 100m are used to exclude hexagons in which there is an excess of nitrate with respect to phosphate according to the Redfield ratio, meaning phosphate is the first limiting nutrient in the upper ocean. Figure C.2 reveals that this is only the case for a handful of locations.

2.5.2. Small water depth and/or substantial presence of land

For the depths inside the hexagonal columns data from GEBCO Compilation Group (2023) is used. Hexagons with a median bed level above -500m and/or a 90th percentile bed level greater than 0m are disregarded from the model simulations. The former criterion ensures detritus can sink to significant depths and that sedimentary processes play a minor role. Also, by adopting this criterion coastal waters are excluded (McConnaughey, 1984), where nitrogen addition is known to cause eutrophication (Secretariat of the Convention on Biological Diversity, 2009). The second criterion is necessary due to the coarse resolution of the hexagons. As a result, hexagons around coastal zones may contain a significant portion of land. The 90th percentile criterion is therefore applied to filter out these hexagons, while retaining those that include only a small portion of land, such as hexagons in the vicinity of Pacific Ocean islands (Figure C.3).

2.5.3. Impractical for transportation

Considering the importance of nitrogen transportation to the oceanic locations for the feasibility of the nitrogen fertilization, this study excludes ocean regions located poleward of 65 °N or 50 °S from model computations. These regions are far from continents and high dense shipping routes.

2.5.4. Large horizontal surface transport (advection) of nutrients

The developed model framework only includes nutrient supply by vertical eddy diffusion. Hexagons for which the horizontal surface transport is considered strong and hence expected to be the dominant nutrient supply mechanism are therefore excluded from computations, since the model is not valid for those locations. Whether this is the case is determined by calculating the annual average horizontal gradients in phosphate and nitrate over the upper 100m of each hexagon (using WOA data, Garcia et al. (2019b)). These upper 100m are considered to be the Ekman layer, and therefore directly driven by wind stress (Talley, 2012). Maps of the annual average surface concentrations (used to determine the gradients) and horizontal surface gradients of both phosphate and nitrate of the upper 100m of the global ocean are presented in C.3. The global distribution of surface gradients for both nutrients is depicted in a histogram in C.3. The global distributions of nutrient gradients are positively skewed, indicating that most hexagons exhibit relatively small gradients, with fewer exhibiting larger gradients. Due to this skewness, the median of the global distribution for both nutrient gradients is selected as the filtering criteria. Hexagons with a phosphate and/or nitrate horizontal surface gradient larger than the median gradient specific to the corresponding nutrient are excluded from computations. The result is presented in Figure C.10.

Analysing Figure C.10, one can observe that regions experiencing influence of upwelling are excluded from computations. This includes coastal, equatorial and polar upwelling zones. Upwelling brings nutrient-rich waters toward the surface, forming nutrient gradients. Not all nutrients are consumed in the upwelling zones themselves, due to other growth limitations or residence time, and they laterally circulate to other regions. On the way the nutrients are consumed, horizontal gradients decrease and the contribution of lateral transport diminishes. With the used filtering criteria, regions where iron is the first limiting nutrient and surrounding zones are excluded (compare Figures C.2 and C.10). In these areas, macronutrients cannot be fully utilised (as explained in 1.1.4) leading to horizontal nutrient transport and subsequent gradients. In light of these evaluations, the applied filtering criteria is deemed appropriate.

Figure 2.8 presents the combined outcome of the four different filtering aspects described above. All

red hexagons are filtered out, with the darker red hexagons being excluded only due to the horizontal surface transport (advection) criterion (969 hexagons). The blue hexagons are included in the model computations. A total of 1527 hexagons remain, 706 in the Northern Hemisphere and 821 in the Southern Hemisphere. Following the filtering steps, the remaining hexagons are mostly located within the subtroical gyres, and to a lesser extend zones around the edges of the gyres.

2.5.5. Nitrogen cycle feedbacks

As pointed out in 1.1.6, the N cycle feedbacks from nitrogen fixation and denitrification can offset the desired effects of the fertilization. It could therefore be desirable to avoid these feedbacks and filter out corresponding hexagons, if possible. Especially the denitrification feedback, since this may lead to a net loss of fixed N. Although the effect of this net loss on ocean productivity might not be observed already within the 5 years of focus, avoidance is desired.

Comparing the still included ocean regions after the filtering processes from 2.5.1 to 2.5.4 (Figure 2.8) and areas where denitrification occurs (Figure 1.6), oceanic regions prone to denitrification are already excluded from the model framework.
Nitrogen fixing diazotrophs cover a large area of the global oceans. Comparing Figure 2.8 and Figure 1.6, in the majority of the included hexagons nitrogen fixation likely occurs, and excluding these hexagons from simulations and thus fertilization experiments is therefore not directly possible.

This implies that regarding the nitrogen cycle, no extra hexagons can be excluded from simulations upfront.
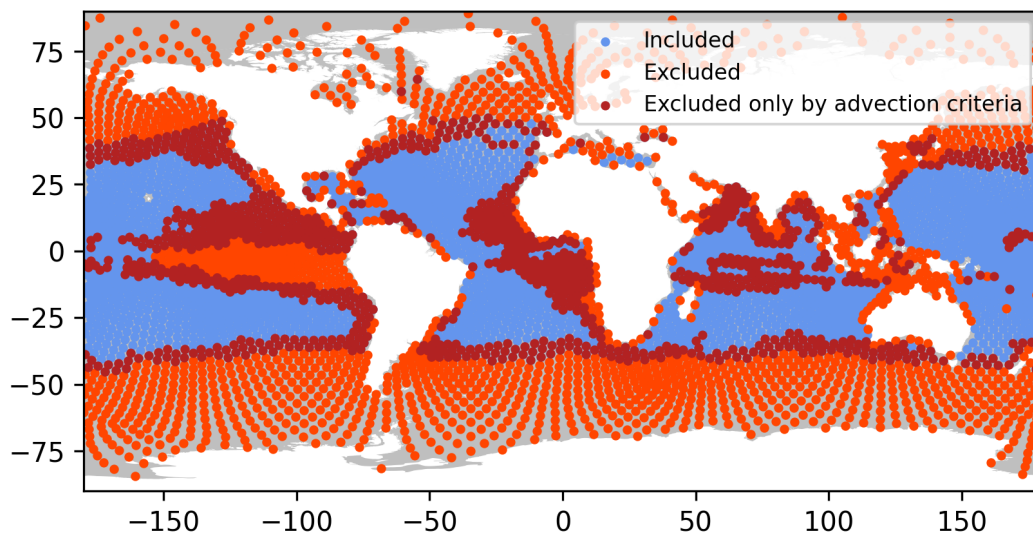
Figure 2.8: Map of the combined outcome of the hexagon filtering steps described in 2.5.1, 2.5.2, 2.5.3 and 2.5.4. The blue hexagons are used for model computations (1527 hexagons). All red hexagons are filtered out, with the darker red hexagons being excluded only due to the horizontal surface transport (advection) criterion.

2.6. Initial and boundary conditions

For all state variables and boundary conditions of both the ecosystem and physical model, data must be found and used as input for the hexagons included in model computations. Table 2.1 gives an overview of all data used. For the objective of this study, the use of seasonal data is considered adequate. Seasonal data is thus applied for all input data except solar irradiance and iron, since for these only monthly datasets were available (and it is not considered to further processes them into seasonal data). The four seasons considered in this study are winter (January to March), spring (April to June), summer (July to September), and autumn (October to December).

It is important to note that most of the data used in this study is available at a finer horizontal

resolution than that of the hexagonal grid employed in the model framework. Therefore the average of all data inside a hexagon is taken using Python's Gdal warp function, unless specified otherwise. The datasets that require further processing, beyond regridding on the hexagons by taking the average, or those that require additional considerations, are discussed below.

Variable	Source	Data	Data frequency	Time span	Unit
State variables					
Phytoplankton (P_O & P_D)	Aqua-Modis 3&4[1]	Near surface chlorophyll concentration	Seasonal climatology	2002 - 2022	mg Chl m^{-3}
Zooplankton (Z)	Aqua-Modis level 3&4[1]	Near surface chlorophyll concentration	Seasonal climatology	2002 - 2022	mg Chl m^{-3}
Particulate detritus (D)	-	-	-	-	-
Phosphate (PO_4)	World Ocean Atlas 2018[2](WOA)	Phosphate concentration	Seasonal climatology	1960 - 2017	$\mu mol/kg$
Nitrate (NO_3)	World Ocean Atlas 2018[2](WOA)	Nitrate concentration	Seasonal climatology	1960 - 2017	$\mu mol/kg$
Oxygen (O_2)	World Ocean Atlas 2018[3](WOA)	Dissolved oxygen concentration	Seasonal climatology	1960 - 2017	$\mu mol/kg$
Boundary conditions					
Temperature (T)	World Ocean Atlas 2018[4](WOA)	Temperature	Seasonal climatology	2005 - 2017	° C
Salinity (S)	World Ocean Atlas 2018[5](WOA)	Salinity	Seasonal climatology	2005 - 2017	psu
Radiation	Copernicus CCI SLSTR on sentinel 3a[6]	Surface downwelling shortwave flux	Monthly	2017 - 2021	W/m²
Iron (Fe)	Keller et al. (2012)	Dissolved iron concentration	Monthly	-	nmol m^{-3}
Mixed layer depth (MLD)	World Ocean Atlas (2018)	MLD	Seasonal climatology	2005 - 2017	m

[1] NASA Ocean Biology Processing Group (2022)
[2] Garcia et al. (2019b)
[3] Garcia et al. (2019a)
[4] Locarnini et al. (2018)
[5] Zweng et al. (2019)
[6] Poulsen et al. (2022)

Table 2.1: Overview of data sources used for all initial and boundary conditions

2.6.1. Initial conditions of state variables
For the initial conditions of all state variables, seasonal data is used. So depending on the start of the simulation, the corresponding initial data is used.

Ordinary and diazotrophic phytoplankton
The initial condition of phytoplankton are determined from MODIS derived chlorophyll concentrations assuming a carbon to chlorophyll ratio of 50 (required to go from mg Chl m^{-3} to mmol N m^{-3})

(Sathyendranath et al., 2009; Schmittner et al., 2005). Since MODIS can only measure the surface chlorophyll concentration, the data needs to be extrapolated on the vertical grid. As in Schmittner et al. (2005), which uses a predecessor of the model from Keller et al. (2012), an exponential profile for both phytoplankton is assumed with an e-folding depth of 100m. For both phytoplankton a surface value of half the measured chlorophyll concentration is used.

Zooplankton and detritus

Measured data for zooplankton and sinking detritus are sparse, and therefore initialised using the 100m e-folding exponential profile with a surface value of $1/10^{th}$ of the chlorophyll concentration and a uniform value of 10^{-4} mmol N m^{-3}, respectively (Schmittner et al., 2005).

Phosphate and nitrate

Seasonal data of phosphate and nitrate of the WOA is available from the surface until 800m, while only annual data is available below this depth. These datasets are merged to create the seasonal input data for the full water column. In order to convert the data to the units mmol m^{-3}, a seawater density of 1000 kg m^{-3} is used for the whole ocean.

In the vertical, concentrations of PO_4 and NO_3 are measured at high intervals. To conserve the mass of PO_4 and NO_3 within the water column the measurements are regridded on the vertical grid. This process assumes a linear profile between the measurements and employs an integration-interpolation-differentiation function.

Oxygen

The preparation of oxygen data follows a similar procedure as that for phosphate and nitrate, as discussed above. The difference is that oxygen measurements over the full ocean depth are available.

2.6.2. Boundary conditions

For the boundary conditions a combination of seasonal and monthly data is used. The same boundary conditions are used each simulation year.

Temperature

The WOA temperature data is measured at 102 standard depth levels in the vertical. To establish temperature values for each grid layer, a linear interpolation technique using the midpoints of the grid layers is employed.

Salinity

Only the salinity value in the first grid layer is required (to determine the oxygen effluent). Integration-differentiation of the surface measurements is done to determine this.

Iron

For the iron concentrations the same monthly iron mask is used as in (Keller et al., 2012), which is based on outputs of the BLING model of Galbraith et al. (2010). The horizontal resolution of this iron mask is similar to that of the hexagonal grid and therefore for some hexagons the Gdal Warp function does not return a value. For those hexagons, the nearest neighbour principle is applied. To regrid the iron concentrations on the higher resolution of this study's vertical grid, again the integration-interpolation-differentiation principle is employed.

3 | Experimental design of one-off nitrogen fertilization

In Chapter 2, the set-up of the 1DV model framework to simulate the BCP and ocean fertilization and its carbon sequestration is discussed. This chapter describes the experimental design to analyse the potential carbon sequestration from ocean nitrogen fertilization and the corresponding simulations that are required. Before any nitrogen fertilization is modelled, a series of baseline simulations of the present state biological carbon pump are conducted. These baseline simulations are explained and described in section 3.1. From there on different nitrogen fertilization simulations are performed, the design of those is presented in section 3.2. In this thesis, the focus is on the long-term carbon sequestration reached within 5 years after the fertilization, but a single long simulation is performed, which is discussed in section 3.4. The outputs that are saved from each simulation are summed up in section 3.5.

3.1. Baseline simulations (BS)

In this study, the baseline simulations function as model 'spin-up' and control simulations. The fertilization simulations are initialised with model variable states taken from the end of the spin-up period. This is further discussed in section 3.3. The control aspect of the baseline simulations serves as a 'do-nothing' comparison, facilitating an assessment of the additional carbon storage resulting from nitrogen fertilization in a FS. Initial and boundary conditions described in section 2.6 are used as input for the baseline simulation. Subsequently, it is forced by the marine ecosystem and physical model, and run for 10 years.

In the physical model of a simulation, a constant eddy diffusivity is used globally in each of the three oceanic layers. But as already stated in 2.3.2, eddy diffusivity is highly variable in space and time. Preliminary test simulations for a handful of hexagons using different values for the thermocline diffusivity (D_{thermo}) while keeping the diffusivities in the surface mixed layer and deep ocean constant, revealed that a different D_{thermo} can result in large differences in nutrient concentrations and consequently phytoplankton productivity in the upper ocean layers. Hence, it is chosen to use four values for D_{thermo} throughout the simulations: 10^{-5}, $3 \cdot 10^{-5}$, $6 \cdot 10^{-5}$ and 10^{-4} m^{2}s^{-1}. Adopting four different thermocline diffusivity values yields information on the sensitivity and puts the result into perspective. The used thermocline eddy diffusivity values are in the range of $\mathcal{O}(10^{-5})$ (its global average) but towards the higher end. The reasoning behind this is to implicitly account for the lateral (mesoscale) eddy transport of nutrients into the thermocline. This lateral transport is an important nutrient replenishment mechanism of the interior of subtropical gyres (Gupta et al., 2022). Since the developed model framework only includes transport by vertical eddy diffusion, this replenishment mechanism is not directly implemented. Its effect can however be simulated indirectly using eddy diffusivities towards the higher end.

In total four distinct baseline simulations are executed, each employing a different value for D_{thermo}, as discussed above. The baseline simulations all start on January 1st. The 10-year simulations require 16 computer hours to complete.

Specific ecosystem outputs of the baseline simulations are presented in Tables D.1 to D.4. These outcomes confirm that a different thermocline diffusivity results in a significant difference in NPP, as well as nitrogen fixation. The difference in NPP and N fixation in the 5th year of the baseline simulations are up to a factor 8 and 5, respectively, comparing the different simulations. It can be observed

that an increase in thermocline diffusivity corresponds to a higher NPP, but a concurrent decrease in nitrogen fixation.

It can also be observed that in none of the four baseline simulations a steady state is reached for the ecosystem, neither on a global or (for most also) hexagonal scale. This is also the case for the yearly amount of nitrogen fixation, which on global scale reduces annually in all baseline simulations. A yearly reduction of N fixation is also observed in most hexagons (Figure D.1). Since the feedback from nitrogen fixation can offset the carbon sequestration effect from the fertilization, it is important to address this. It is chosen to adopt different baseline simulation spin-up times, to be able to gain a comprehensive perspective on the results and strengthen their reliability. Two different spin-up times are used; 1 year and 4 years.

3.2. Fertilization simulations (FS)

After the baseline simulations are executed, various fertilization simulations are conducted. Per baseline simulations different fertilization simulations are performed. The design of the fertilization simulations and their linkage with the baseline simulations are explained in this section.

In a FS, nitrogen is fertilized to all the included hexagons as one-off (single pulse) additions. Figure 3.1 illustrates the addition for a single hexagon. With these one-off additions, the nitrogen limitations (at that moment) of the grid layers that comprise the surface mixed layer of each hexagon are neutralized. In other words, nitrogen is added to these layers to reach a nitrogen to phosphorous ratio equal to the Redfield ratio. This is only done in the grid layers that have a shortage of nitrate with respect to phosphate at the time of the fertilization, if this is not the case the concentration is left untouched.

(a) Nutrient ratios just before fertilization.

(b) Nutrient ratios immediately after fertilization. The ratios in red are the ones that are changed.
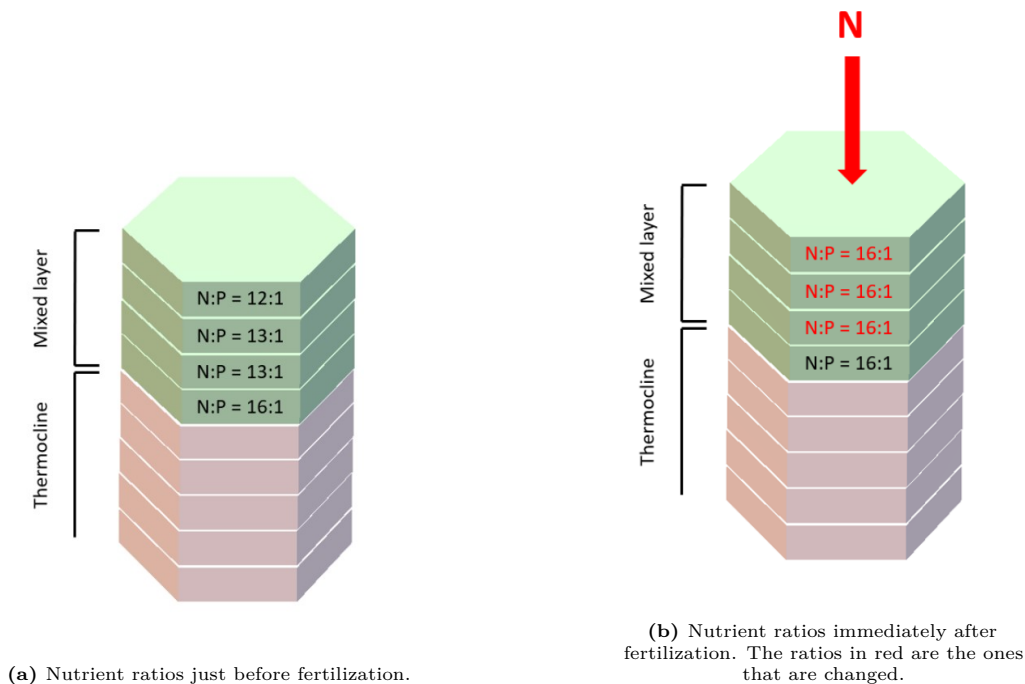
Figure 3.1: Illustrative example of the nitrogen fertilization approach to a single hexagon

In a fertilization simulation, the one-off nitrogen additions to all hexagons are performed at 1st of January, 1st of April, 1st of July or 1st of October, identifying the start of the winter, spring, summer and autumn season, respectively. A different timing is associated with a different MLD, nutrient concentration and consequently a different amount of added nitrogen during fertilization. In each fertilization simulation nitrogen is added once (a single pulse) to the hexagons, so for each different season of addition there is a different simulation. Nitrogen additions are done right at the beginning of a fertilization simulation.

Total number of fertilization simulations
Considering the moments of nitrogen fertilization and the variations in baseline simulation spin-up discussed above and in the previous section, for each D_{thermo} value (baseline simulation) 8 different fertilization simulations are performed. These 8 simulations together are referred to as a simulation group. An overview of the set-up of the fertilization simulations for a single baseline simulation is given in the section 3.3. Since four different baseline simulations are conducted, a total of 32 fertilization simulations are performed. Each of these fertilization simulations lasts 5 years because the objective is to assess the long-term carbon sequestration reached within 5 years after the one-off fertilization. Each FS takes 8 hours of computer time.

3.3. Overview simulations set-up
A schematic overview of the set-up of the baseline simulation, the fertilization simulations and their linkage for a single D_{thermo} is shown in Figure 3.2. The blue, green, yellow and orange dots present the start of the winter, spring, summer and autumn seasons, respectively. The small dotted lines separate different simulations (calendar) years. As can be seen from the figure, the baseline simulation lasts 10 years. The fertilization simulations are initialised (black arrows) with the states at the end of a season of the baseline simulation, which season end is used depends on the fertilization simulation. To elucidate this configuration, two distinct examples are considered.

The FS which is characterized by 1 year spin-up and where nitrogen fertilization takes place on January 1st is initialised with the model variable states at the end of the autumn season of baseline simulation year 1. The FS which is characterized by 4 full years of spin-up and in which nitrogen additions are done on the 1st of July, is initialised with baseline simulation states at the conclusion of the spring seasons of the fifth simulation year. This encompasses 4 full years of spin-up and an additional two seasons to align the simulation's start date with July 1st.

In all fertilization simulations, nitrogen is added immediately following the simulation's initiation, as indicated by the red arrows. To analyse the effect of the nitrogen fertilization, all fertilization simulations are compared with the overlapping part of the baseline simulation, which is illustrated in the figure.

3.4. Single long simulation
The main focus of this thesis is to determine the long-term carbon storage achieved from one-off nitrogen fertilization within 5 years after the nitrogen addition. However, there is also an interest in gaining insight into the potential long-term carbon storage after an extended period following fertilization, as well as understanding the temporal evolution of cumulative long-term carbon sequestration. To address this, a single 50-year-long fertilization simulation is conducted. Also in this simulation, the nitrogen addition is performed immediately at the beginning of the simulation. This extended fertilization simulation is characterized by a thermocline diffusivity of $3 \cdot 10^{-5}$ m^{2}s^{-1}, 1 year of baseline simulation spin-up, and nitrogen additions are done at the beginning of July. Correspondingly, an extended baseline simulation is also executed.

3.5. Output variables
From each simulation, and for each hexagon, the following outputs are saved:

- The states of the seven model variables at the end of each season [mmol N m^{-3}, mmol P m^{-3} or mmol O_2 m^{-3}, depending on the variable]
- The cumulative total net primary production in the water column, saved at the end of each season [g C m^{-2}].
- The cumulative total nitrogen fixation in the water column, saved at the end of each season [g N m^{-2}].
- The cumulative remineralization of organic matter in each grid layer, saved at the end of each season [g C m^{-3} per grid layer].
- For the fertilization simulations only: The amount of nitrogen added to each hexagon [g N m^{-2}].

The parameters are saved in grams, not mole (which are used in the model simulations). This choice of unit is preferred because it aligns with common understanding and practical applications. Using the molar mass of elements facilitates this conversion.

The data undergo further processing required to be able to compare fertilization and baseline simulations with each other. The steps to obtain the long-term carbon sequestration from the one-off nitrogen fertilization, using the cumulative remineralization of the simulations, are presented in the Chapter 4.
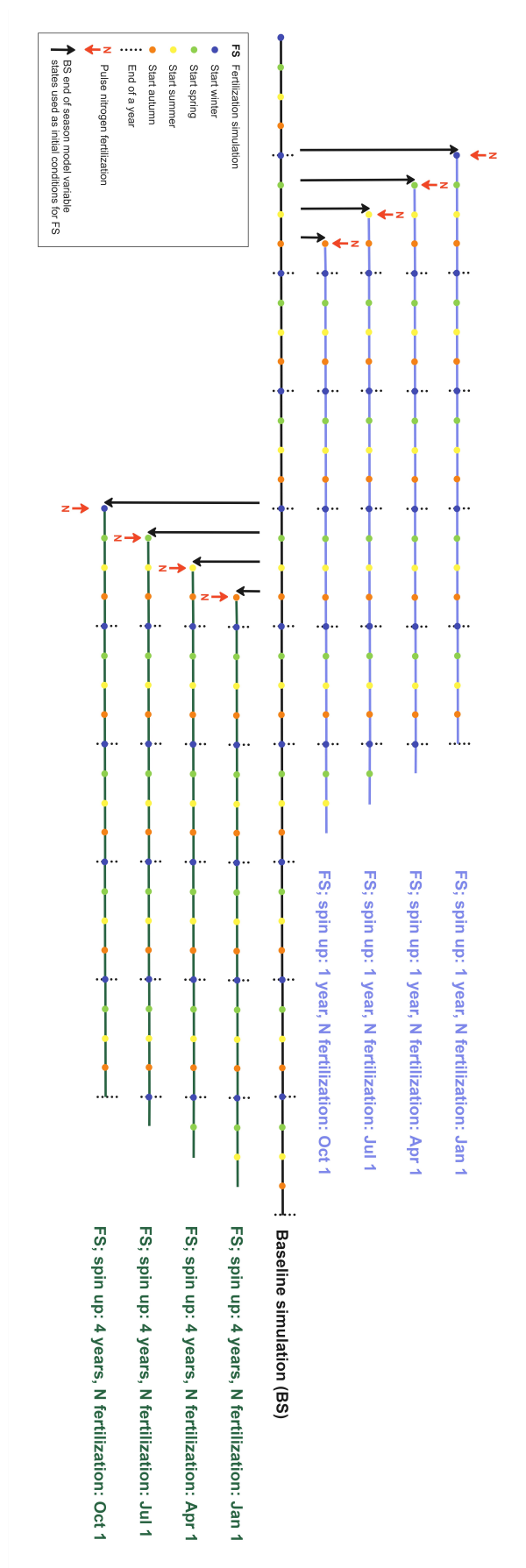
Figure 3.2: A schematic overview of the set-up of the baseline simulation, the fertilization simulations and their linkage for a single D_{thermo} value. The blue, green, yellow and orange dots present the start of the winter, spring, summer and autumn seasons, respectively. The small dotted lines separate different simulations (calendar) years. The fertilization simulations are initialised (black arrows) with the states at the end of the corresponding season of the baseline simulation. Nitrogen additions are done immediately at the start of the fertilization simulations (red arrows). The fertilization simulations are compared with the overlapping part of the baseline simulation.

4 | Simulation post-processing: carbon sequestration

This chapter presents the required simulation post-processing to obtain the long-term carbon sequestration resulting from the fertilization achieved within 5 years after the event, as this is not explicitly modeled.

Figure 4.1 shows a visualization of the simulation data post-processing and calculation steps. It is applied to a single hexagon from a fertilization simulation characterized by 4 years of baseline simulation spin-up and nitrogen is added on the first of July. The different steps are described below using the figure. All hexagons in each simulation involve the same steps.

The cumulative released CO_2 from organic matter remineralization in the fertilization and baseline simulation are used to obtain the long-term carbon storage resulting from the nitrogen addition. The initial step involves extracting relevant data from the baseline simulation, excluding remineralization during the spin-up period to facilitate the comparison of the two simulations (first line Figure 4.1). The cumulative outcome over the 5-year duration of the fertilization simulation can be used immediately.
Following this, the cumulative CO_2 remineralization of the (processed) baseline simulation is subtracted from that of the fertilization simulation (left figure of second line Figure 4.1). This results in the additional amount of CO_2 released in the FS (right figure of second line Figure 4.1), and it therefore follows from the nitrogen fertilization.
Subsequently, the additional carbon remineralized in (each grid layer) is multiplied by the corresponding 100-year (long-term) sequestration fractions (third line Figure 4.1). The sequestration fractions are elaborated on in the text box below.
Finally, the depth integral of this product is performed (fourth line Figure 4.1), to obtain the total amount of long-term carbon sequestered in a hexagon as a result of the fertilization.

100-year sequestration fractions

The 100-year sequestration fractions are derived from the study of Siegel et al. (2021). This research used a 3D ocean circulation inverse model to investigate the timescales over which CO_2 released at global spatial scales remains sequestered in the ocean, yielding the fraction of carbon that remains stored as a function of time. For this thesis the 100-year sequestration fractions are used, which represent the portion of released CO_2 that is stored in the ocean for a minimum of 100 years. The global 100-year sequestration fractions are for a few depth levels depicted in Figure 1.3.
In other words, these fractions facilitate the quantification of the amount of additional remineralized CO_2 at each depth level (resulting from fertilization) that remains in the ocean for at least 100 years, thereby qualifying as long-term carbon storage.
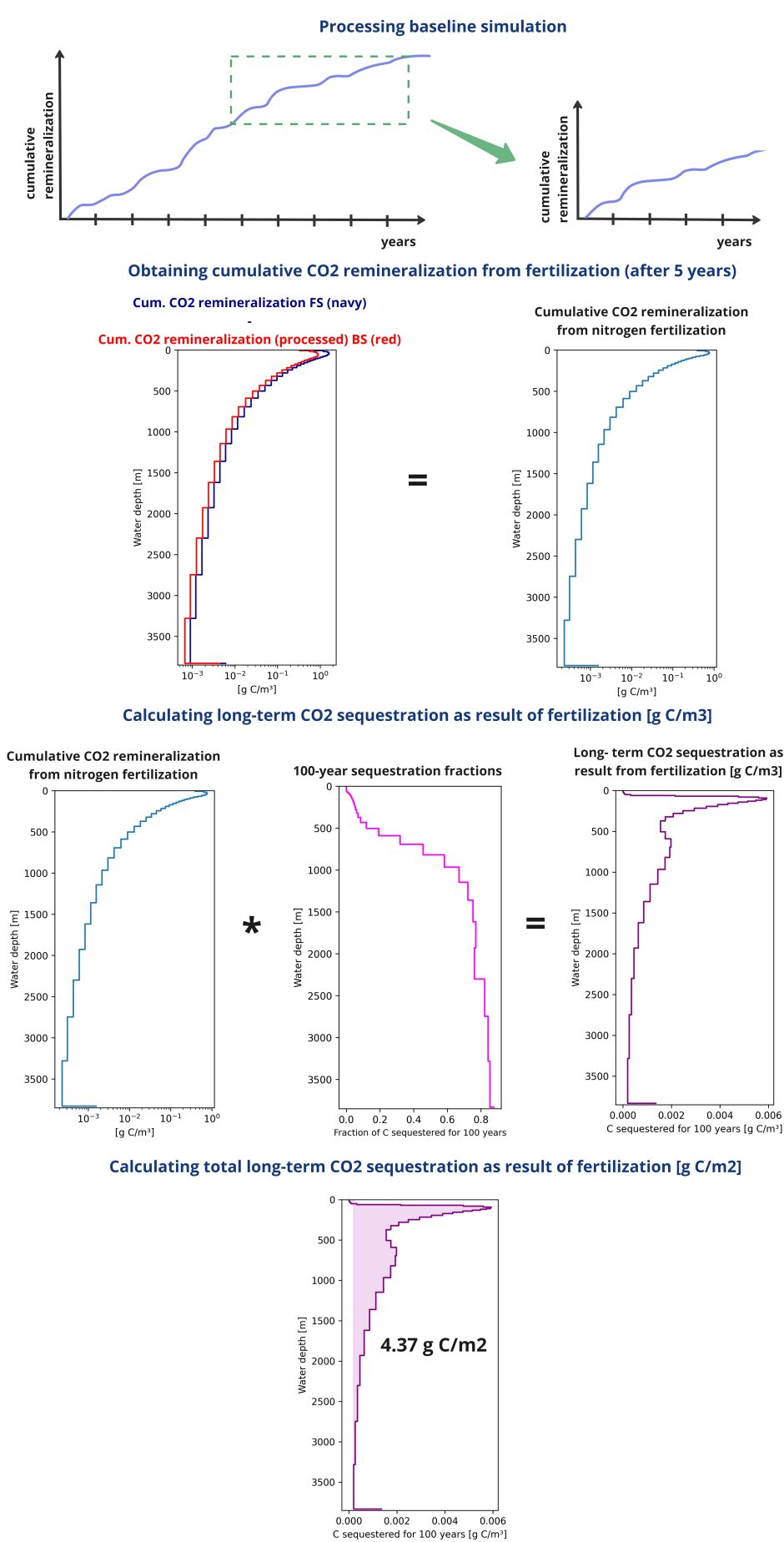
Figure 4.1: Overview of the simulation data processing to obtain the amount of carbon that remains sequestered for 100 years as a result of a fertilization. The steps are specifically applied to the hexagon at 31° S, 0.6° W in the fertilization simulation characterized by a thermocline diffusivity of $6 \cdot 10^{-5}$ m^{2}s^{-1}, baseline simulation spin-up of 4 full years and the nitrogen addition is done on the 1st of July.

To summarize, this part (Chapters 2 to 4) presented the materials and methods of this research. A 1DV model framework was established by partitioning the ocean into hexagonal columns and coupling a biochemical model with the physical circulation model, which only incorporates vertical eddy diffusion. Half of the ocean was excluded from model computations because the surface advection of nutrients was expected to be dominant there, thus not allowing for 1DV modelling. Also hexagons which are not of interest were disregarded, mostly because nitrogen is not the first limiting nutrient. With these filtering criteria, regions prone to denitrification were already filtered out. Nitrogen fixation was likely to occur in the majority of the hexagons still included, thus excluding nitrogen-fixing regions from our simulations upfront was not a viable option.

With the model framework, 4 baseline simulations (BS) (for spin-up and comparison) and 32 fertilization simulations (FS) are performed. In a fertilization simulation, nitrogen was fertilized as a one-off (single pulse) addition to all hexagons, fully replenishing nitrogen limitation in the mixed layer (if any). The fertilization simulations differ in applied thermocline diffusivity, baseline simulation spin-up, and season of nitrogen addition. To obtain the effects from the one-off nitrogen fertilization, the simulations outputs are post-processed, and the outcomes of the BS are subtracted from the FS.

Part II

Results

5 | One-off nitrogen fertilization on global scale

In this chapter, the results of the one-off nitrogen fertilization simulations are analysed on a global scale. The one-off nitrogen fertilization was simulated using the developed 1DV model framework and experimental plan described in Part I. First in section 5.1, the globally integrated results of nitrogen fertilization in all 32 simulations are presented. Here, 'globally integrated' denotes the summation of the outcomes from all hexagons. Section 5.2 focuses on the nitrogen fertilization outcomes of two FS that reveal notable differences in globally integrated values. In section 5.3 an aggregated outcome of the global one-off nitrogen fertilization is obtained from the simulations. Section 5.4 presents the results from the extended simulation, as outlined in 3.4.

5.1. Globally integrated results from one-off nitrogen fertilization in the 32 fertilization simulations

This section provides an examination of the globally integrated effects from the one-off nitrogen fertilization across all FS, presented in Figure 5.1. In this figure, distinct bar colours correspond to different seasons of addition. Panels group simulations with the same thermocline diffusivity, with an increase in D_{thermo} from the left to the right panel. Within each panel, simulations with 1-year (4-years) baseline simulation spin-up are presented in the left (right) block. Figure 5.1a presents the long-term carbon storage resulting from the nitrogen additions achieved within a 5-year period following the fertilization. This is determined using the cumulative additional remineralization in the FS according to the steps in Figure 4.1. Figure 5.1b displays the amount of nitrogen added in each fertilization simulation. In 5.1a and 5.1b, the bars are divided by a horizontal line. The portion of each bar below the line corresponds to the Southern Hemisphere, while the portion above represents the Northern Hemisphere.

As previously mentioned, nitrogen fixation is possible in a substantial part of the fertilized hexagons. Hence, an offsetting feedback from reduced nitrogen fixation that decreases the nitrogen perturbation from the additions (see left side of Figure 1.7) in the FS is probable. Figure 5.1c shows this normalized offset [%] stemming from the reduced nitrogen fixation (cumulative over the 5 years) in the fertilization simulation as compared to the baseline simulation. This normalization takes into account the total added nitrogen, expressed through the following equation: $\frac{Nfix,BS-Nfix,FS}{Nadd} * 100\%$.

Finally, the global efficiency ratios of long-term (LT) stored C [gm^{-2}] per N added [gm^{-2}] (C$_{LT}$/N) for all 32 simulations are shown in Figure 5.1d. It is essential to highlight that the C:N mole ratio of 6.625:1 translates to 5.68:1 in terms of mass. This conversion is derived from scaling the mole ratio with the molar mass of the two elements (6.625*12.01/14.007). So if all the added nitrogen would result in the long-term sequestration of carbon, the efficiency ratio would be 5.68.

It must be noted that hexagons where the fertilization resulted in a negative carbon sequestration (less carbon sequestration compared to the baseline simulation) have been excluded from the calculations of the globally integrated values across all simulations. Had this exclusion not been applied, the global carbon sequestration (nitrogen addition) would decrease (increase) with a maximum of 0.6% (6%), with an average of 0.2% (2%) across the simulations.

(a) The globally integrated long-term carbon sequestration from the nitrogen additions achieved within 5-year period following the fertilization [Gt C]. The portion of each bar below the horizontal division line corresponds to the Southern Hemisphere, while the portion above represents the Northern Hemisphere.

(b) The globally integrated amount of nitrogen fertilized for all 32 simulations [Gt N]. The portion of each bar below the horizontal division line corresponds to the Southern Hemisphere, while the portion above represents the Northern Hemisphere.

(c) The normalized offset [%] stemming from the reduced nitrogen fixation (cumulative over the 5 years) due to the nitrogen fertilization. This normalization takes into account the added nitrogen, expressed through the following equation: $\frac{Nfix,BS - Nfix,FS}{Nadd} * 100\%$

(d) The global efficiency ratio of C sequestered (long-term) per unit N added [g m^{-2}/g m^{-2}]

Figure 5.1: An overview of the globally integrated results of the one-off nitrogen fertilization in the 32 fertilization simulations, varying in moment of addition, used thermocline diffusivity (D$_{thermo}$) and spin-up of the baseline simulation.

For all 32 simulations, Tables E.1 and E.2 give the numerical values of the globally integrated results of the nitrogen fertilization depicted in Figure 5.1. Hemisphere-specific values are provided whenever applicable. Additionally, Table E.2 includes the number of hexagons per FS where no nitrogen limitation was present in their mixed layer at the time of the addition.

Across the 32 simulations, the global long-term carbon sequestration of one-off nitrogen fertilization varies from 0.07 to 0.18 Gt. The global C_{LT}/N efficiency ratio also exhibits variability, ranging from 0.57 to 0.97. The 32 simulations vary in the moment (season) that nitrogen was added, spin-up time of the baseline simulation and employed thermocline diffusivity. In the subsequent subsections, each of these three components is explored through analyses and comparisons between the simulations.

5.1.1. Season of fertilization

The long-term carbon sequestration and C_{LT}/N efficiency among simulations with the same D_{thermo} and baseline simulation spin-up but a different moment of addition (so simulations within the same block) differ at most by a factor of 2 and 1.3, respectively (Figures 5.1a and 5.1d). Across all fertilization simulations, the most substantial global carbon sequestration is found in the 8 simulations where nitrogen fertilization is performed in July (green bars in Figure 5.1a). Within this subset of 8 simulations, the long-term carbon sequestration varies from 0.14 to 0.18 Gt. These simulations are also characterized by the largest global nitrogen inputs (green bars in Figure 5.1b). These large N inputs can be mainly attributed to the combination of the relatively large depth of the mixed layers in the Southern Hemisphere's hexagons on the 1st July (start cold season) and that they (concurrently) experience (relatively large) nitrogen limitations in their mixed layers (see Appendix E.2). For most diffusivities it is found that the C_{LT}/N efficiency of the July additions is slightly lower compared to the other seasons (most panels of Figure 5.1d), this cannot directly be explained with the outcomes of Figure 5.1 (or Tables E.1 and E.2).

The smallest absolute global carbon sequestration is found in the simulations where nitrogen fertilization took place on January 1st (blue bars Figure 5.1a). Within this subset of 8 simulations, the carbon sequestration ranges between 0.07 to 0.13 Gt. The relatively low carbon sequestration observed in the January addition simulations with two highest D_{thermo} values can be attributed to the comparatively low nitrogen inputs (indicated by the blue bars in the two rightmost panels of Figure 5.1b). Therefore, these simulations exhibit similar C_{LT}/N efficiency values as observed in other seasons (as shown in the two rightmost panels of Figure 5.1d). In contrast, for the lowest D_{thermo} ($= 10^{-5}$ m^{2}s^{-1}), C_{LT}/N efficiency of the two January addition simulations is notably lower than that of the other seasons (compare blue bars of left panel of 5.1d with the other bars). It is suggested that this is the result of a combination of factors. Firstly, the offset from reduced nitrogen fixation is relatively high for these two simulations compared to other seasons, both in normalized terms (as depicted in the left panel of Figure 5.1c) and in absolute values (Table E.2). Secondly, Table E.2 reveals that the number of hexagons experiencing no nitrogen limitation is significantly lower for these January addition simulations compared to other seasons. It is therefore speculated that in the January addition simulation, some hexagons 'naturally' lose their nitrogen limitation within a simulation season. As a result, the added nitrogen has minimal impact in these hexagons, contributing to the relatively low efficiency values observed in these two simulations.

5.1.2. Spin-up duration of baseline simulation

Because in the conducted baseline simulations no equilibrium was reached, especially considering nitrogen fixation, the choice was made to use two different spin-up times to test the sensitivity, as explained in 3.1. Among the 32 simulations performed, pairwise comparisons can be conducted. Each comparison involves simulations with identical thermocline diffusivity and nitrogen addition timing but different spin-up durations. From Figure 5.1c it is evident that in the case of 4-year spin-up simulations (right block of bars in each panel) the percentage offset by reduced nitrogen fixation is comparatively lower when contrasted with the 1-year spin-up (left block of bars in each panel).

The percentage change in carbon sequestration from the one-off additions ranges from -15% to +5% when comparing the 4-year spin-up simulations to their 1-year spin-up counterparts. The C_{LT}/N ratio exhibits a broader spectrum of changes, with percentages ranging from -10% to +41%. For the simulations with 10^{-5} and $3 \cdot 10^{-5}$ m^{2}s^{-1} as thermocline eddy diffusivity an increase in C_{LT}/N is found for the

4 years spin-up compared to the 1-year spin-up, while for the other two diffusivities mostly a decrease in the efficiency ratio is observed.

5.1.3. Thermocline diffusivity

To investigate the effect of varying thermocline diffusivity on carbon sequestration results, the simulations are divided into multiple sets. Each set comprises four fertilization simulations with the same spin-up durations and nitrogen addition timing, but differing thermocline diffusivity. Within each set, the outcomes from the one-off fertilization are compared to one another and the highest relative differences observed are recorded. These analyses reveal that for each set the globally integrated long-term carbon sequestration and C_{LTy}/N ratios exhibit relative variations extending from 1.2 to 2 and 1.7 respectively. For most sets, the smallest C_{LTy}/N ratio is found in the simulation with $D_{thermo} = 10^{-4}$ m^2s^{-1}.

Substantial variations exist in the normalized offset resulting from reduced nitrogen fixation, with a clear trend indicating a reduction in normalized offset as diffusivity increases, as illustrated in Figure 5.1c. While the normalized offset may introduce a bias, as simulations with higher eddy diffusivities are associated with larger nitrogen inputs (Figure 5.1b), the absolute offset from reduced nitrogen fixation is also smaller for higher thermocline diffusivities (see Table E.2). Across all sets, the largest normalized offset [%] is at least 5.8 times larger than the smallest offset, and the maximum relative difference within a set reaches 12.6 times.

This section discussed the globally integrated effects of the nitrogen fertilization and differences among the FS. With the exception of the normalized offset, variations across simulations range within a twofold magnitude. Examining the geographical distributions is also of interest. Therefore, the following section focuses on the spatial patterns of the one-off nitrogen fertilization outcomes of two specific FS. As evident in Figure 5.1 and explored in subsections 5.1.2 and 5.1.3, the most significant contrast arises between simulations featuring $Dthermo = 10^{-5}$ m^2s^{-1} and those with $Dthermo = 10^{-4}$ m^2s^{-1}. Consequently, one FS representative of each of these diffusivity values is selected.

5.2. Spatial patterns

This section presents a qualitative analysis and comparison of the spatial patterns of the effect of the one-off nitrogen fertilization in two fertilization simulations with a thermocline diffusivity characterized 10^{-5} and 10^{-4} m^2s^{-1}. For a fair comparison, simulations with the same moment of nitrogen addition and spin-up are used.

Figure 5.2 displays the global long-term carbon sequestration resulting from the nitrogen additions in the two FS characterized by a baseline simulation spin-up of 1 year, nitrogen additions done on the 1st of July, and D_{thermo} of 10^{-5} (left) and 10^{-4} (right) m^2s^{-1}. In the dark blue hexagons, no nitrogen was added, since there was no nitrogen limitation in their mixed layers at the moment of fertilization. Comparing these two maps of Figure 5.2, one can observe that the spatial sequestration patterns of these two fertilization simulations closely resemble each other. Regions with high (e.g. South Eastern Pacific and South Eastern Atlantic Ocean) and barely any (purple areas) sequestration values exhibit a substantial degree of overlap. However, higher sequestration values are observed locally in the simulation with $D_{thermo} = 10^{-5}$ m^2s^{-1} (left). In the simulation with $D_{thermo} = 10^{-4}$ m^2s^{-1} (right), the high value regions seem to cover a larger area.

Additionally, in regions where no nitrogen addition occurred, a relatively strong correspondence is found in the North Atlantic between the fertilization simulations. In contrast, in the West Pacific Ocean a significant absence of nitrogen fertilization is observed in simulations employing $D_{thermo} = 10^{-5}$ m^2s^{-1}, whereas this phenomenon is not observed in simulations using $D_{thermo} = 10^{-4}$ m^2s^{-1}. These two regions exhibit N:P surface ratios closely to the Redfield ratio (Figure 1.5), which can (in part) explain the absence of nitrogen limitation in these hexagons in the simulations.

Figure 5.3 displays the patterns of the normalized offset of the nitrogen additions from reduced nitrogen fixation in the two simulations. These are clearly very different, as was already observed on a globally integrated scale in Figure 5.1c. In the simulation with $D_{thermo} = 10^{-5}$ m^2s^{-1} (left), for the

majority of the hexagons the added nitrogen (perturbation) is almost fully offset due to reduced nitrogen fixation. For the $D_{thermo} = 10^{-4}$ m^{2}s^{-1} simulation (right) this full offset is found in significantly fewer hexagons, and in most regions the normalized offset is (almost) 0%. In both simulations, regions experiencing high/full offset of the added nitrogen consistently align with regions having (relatively) high rates of nitrogen fixation in the baseline simulations (Figure D.1).

The ratio of long-term C sequestered per unit N added [g m^{-2}/g m^{-2}] in these two simulations is shown in Figure 5.4. The C_{LT}/N efficiency maps from the simulations are quite distinct from one another. The $D_{thermo} = 10^{-5}$ m^{2}s^{-1} simulation (left) shows a more clear partition between high and low efficiencies and relatively higher efficiencies are locally observed, whereas in the $D_{thermo} = 10^{-4}$ m^{2}s^{-1} simulation (right) the efficiencies are more uniform on a global scale. For both simulations, hexagons that encounter a complete offset from reduced nitrogen fixation (Figure 5.3) are logically associated by a 0 (or negative) C_{LT}/N efficiency, as the fertilization is entirely counterbalanced. The highest efficiencies are for both simulations found in the North and South Eastern Pacific. These areas are characterized by relatively high 100-year sequestration fractions (Figure 1.3) and little to no offset from reduced nitrogen fixation (Figure 5.3), factors that drive these high efficiencies. The magnitude and location of the high efficiencies however differ between the simulations. It is for example remarkable that the hexagons in the South Eastern Pacific region around 25° S, 85° W have a high C_{LT}/N efficiency in $D_{thermo} = 10^{-5}$ m^{2}s^{-1} (left), whereas in $D_{thermo} = 10^{-4}$ m^{2}s^{-1} (right) the efficiency is 0 in these hexagons.

Similar features are seen when comparing other simulations with the same spin-up and fertilization moment, but employing either of these two thermocline eddy diffusivities (10^{-5} or 10^{-4} m^{2}s^{-1}). The patterns observed in the fertilization simulations with thermocline diffusivities of $3 \cdot 10^{-5}$ and $6 \cdot 10^{-5}$ m^{2}s^{-1} are positioned intermediate to the simulations characterized by the extreme thermocline diffusivities. The patterns of all 32 simulations are presented in Appendix E.2.

This section analysed the outcomes of two distinct fertilization simulations with each one of the extreme thermocline diffusivities (10^{-5} and 10^{-4} m^{2}s^{-1}). The variation in distribution and magnitude is evident among these patterns of long-term carbon sequestration, nitrogen perturbation offset and C_{LT}/N. Also, for specific zones (hexagons) the relative differences in offset and subsequently C_{LT}/N efficiency are substantial. However, the carbon sequestration and efficiency values for both simulations are within the same range, and the observed local value differences regarding carbon sequestration and efficiency are generally less pronounced than the factor 10 difference between these extreme diffusivity values themselves.
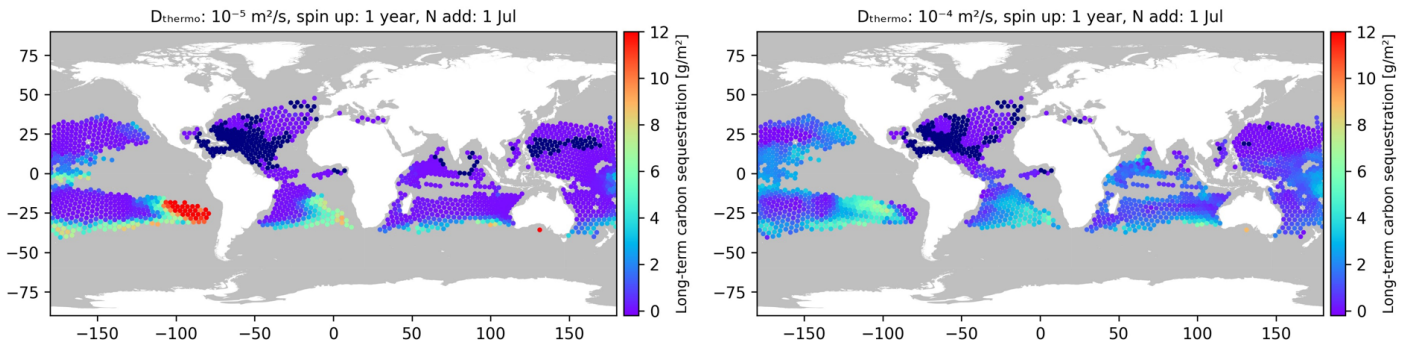
Figure 5.2: Long-term carbon sequestration of the simulations characterized by a baseline simulation spin-up of 1 full year, nitrogen additions are performed on the 1st of July and a D_{thermo} of 10^{-5} m^{2}s^{-1} (left) and D_{thermo} of 10^{-4} m^{2}s^{-1} (right). In the dark blue hexagons no nitrogen addition took place, since there was no nitrogen limitation in their mixed layers at the moment of fertilization.
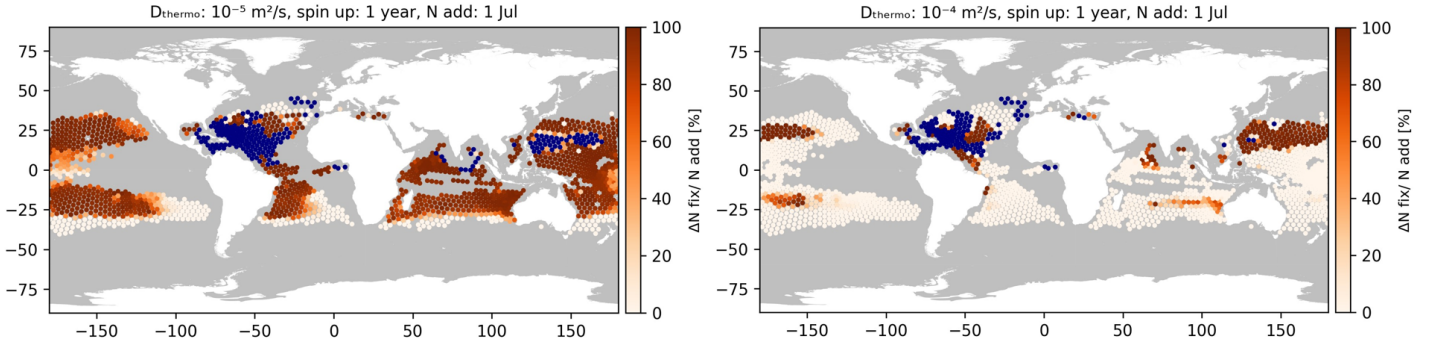
Figure 5.3: Normalized offset of the added nitrogen from reduced nitrogen fixation, calculated by $\frac{Nfix,BS - Nfix,FS}{Nadd} * 100\%$, of the simulations characterized by a baseline simulation spin-up of 1 full year, nitrogen additions are performed on the 1st of July and a D_{thermo} of 10^{-5} m^{2}s^{-1} (left) and D_{thermo} of 10^{-4} m^{2}s^{-1} (right). In the dark blue hexagons no nitrogen addition took place, since there was no nitrogen limitation in their mixed layers at the moment of fertilization.
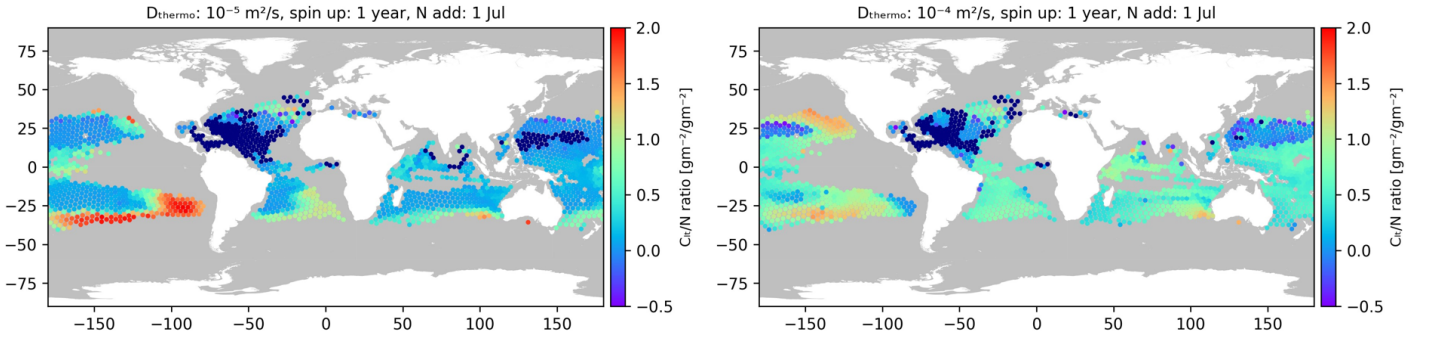
Figure 5.4: Ratio of long-term C sequestration per unit N added [g m^{-2}/g m^{-2}] of the simulations characterized by a baseline simulation spin-up of 1 full year, nitrogen additions are performed on the 1st of July and a D_{thermo} of 10^{-5} m^{2}s^{-1} (left) and D_{thermo} of 10^{-4} m^{2}s^{-1} (right). In the dark blue hexagons no nitrogen addition took place, since there was no nitrogen limitation in their mixed layers at the moment of fertilization.

5.3. Aggregated outcome of global one-off nitrogen fertilization

An aggregated outcome is obtained from a series of simulations, aiming to derive a 'final estimate' of the fertilization results. These values are subsequently used in Chapters 7 and 8 to evaluate the feasibility and overall potential of one-off nitrogen fertilization as global CDR technique. An aggregated outcome for the long-term carbon sequestration resulting from one-off nitrogen fertilization (achieved within a 5-year period following the fertilization) and the required nitrogen is obtained by averaging the results of the one-off fertilizations performed in July (green bars Figure 5.1). These 8 fertilization simulations, chosen for their highest globally integrated sequestration values, also exhibit a slightly lower global C_{LT}/N value compared to other seasons for most D_{thermo} values, offering a conservative efficiency estimate.

In this calculation, hexagons with a C_{LT}/N ratio smaller than 0.3 [g m^{-2}/g m^{-2}] are excluded from these simulations. Hexagons exhibiting an efficiency below the established threshold are observed across extensive areas in all 8 simulations (see Appendix E.2.3). Although this somewhat arbitrarily chosen threshold introduces an element of subjectivity, it allows us to exclude hexagons where the addition of nitrogen had a minimal sequestration effect and are thus not of interest for the CDR approach. The hexagons that are still included in at least 5 of these 8 simulations are highlighted blue in Figure 5.5 (C_{LT}/N>0.3). The red hexagons are excluded (C_{LT}/N<0.3). Using this threshold, hexagons in which in the majority of the 8 simulations a substantial or complete offsetting feedback of the added nitrogen occurs are now excluded (compare 5.5 with the patterns of reduced nitrogen fixation offset from these 8 simulations in Appendix E.2.2). Also hexagons that experienced no nitrogen limitation in their mixed layers are disregarded.

Excluding these 'low-efficiency' hexagons from the 8 simulations yields the integrated long-term carbon sequestration, C_{LT}/N, and normalized offset from reduced nitrogen fixation fall within the ranges of 0.14 - 0.18 Gt, 0.6 - 1.04, and 1% - 17%, respectively, across all 8 simulations.

Averaging the outcomes of these 8 July addition simulations results in the aggregated outcome of the fertilization. It is determined that one-off fertilizing 0.20 Gt of nitrogen results in the long-term carbon sequestration of 0.16 Gt of carbon after 5 years, which implies a C_{LT} efficiency of 0.8. This averaged outcome is associated with a normalized offset from reduced nitrogen fixation of 6%.
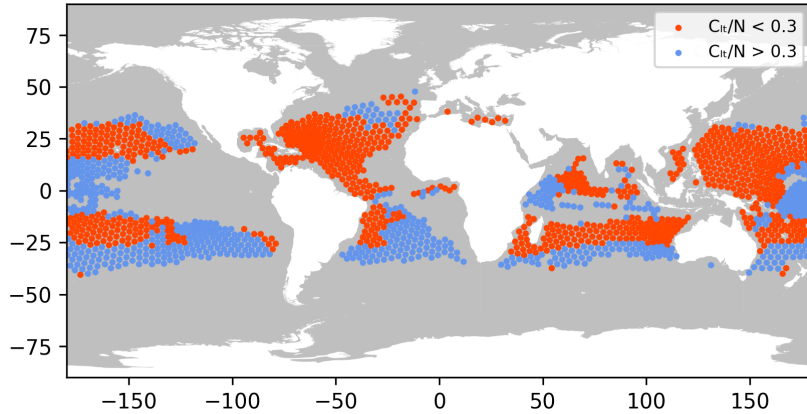
Figure 5.5: Hexagons included (blue) and excluded (red) from the one-off fertilization results in at least 5 of the 8 fertilization simulations in which nitrogen was added in July based on C_{LTy}/N efficiency threshold of 0.3. Using this threshold excludes hexagons where the addition of nitrogen had a minimal sequestration effect.

5.4. Carbon sequestration in 50-year simulation

The focus of this thesis is on the long-term carbon sequestration reached within 5 years after the one-off fertilization. But as discussed in section 3.4, one extended fertilization simulation of 50 years was performed, and its corresponding baseline simulation. For this longer simulation a thermocline diffusivity of $3 \cdot 10^{-5}$ m^{2}s^{-1} and 1-year baseline simulation spin-up was used, and nitrogen additions were conducted at the start of July.

After 50 years, the 0.22 Gt of nitrogen added in the simulation has resulted in the long-term sequestration of 0.33 Gt of carbon. The normalized offset from reduced nitrogen fixation is 31% and the C_{LT}/N efficiency ratio is 1.5. For comparison, 5 years after the fertilization 0.17 Gt of long-term carbon storage is reached. After 5 years the normalized offset is 26% and C_{LT}/N is 0.79.

The patterns of the carbon sequestration, C_{LT}/N ratio and normalized offset are similar for the 5 and 50 year time frame, but locally higher sequestration values and efficiencies are found after 50 years, and for additional hexagons the nitrogen addition is fully offset by decreased N fixation (compare Figure E.13 with the associated figures of the effects after 5 years in Appendixes E.2.1, E.2.3 and E.2.2).
Larger carbon sequestration and efficiency ratio are expected, due to the extended period for the fertilized nitrogen together with CO_2 to be incorporated into organic matter, exported to depth and remineralized (but without long-term storage), diffuse to the upper ocean and subsequently be reused in organic matter production. Figure 5.6 shows the evolution of the globally integrated cumulative long-term carbon storage from the one-off fertilization over the 50 years of simulation. The depicted curve shows an initial phase of rapid growth in cumulative carbon sequestration (within the first 5-10 years), followed by a gradual decline in the rate of increase, resulting in progressively slower annual increase.

In essence, the long-term carbon sequestration resulting from the one-off fertilization after 50 years is approximately twice the quantity achieved within the initial 5 years.
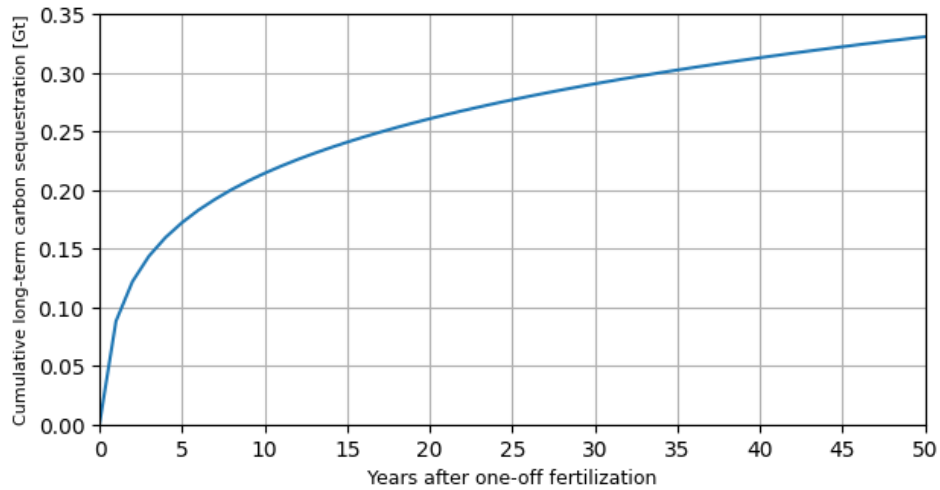
Figure 5.6: Temporal evolution of the globally integrated cumulative long-term carbon storage from the one-off fertilization over the 50 years of the extended simulation.

In summary, this chapter presented an analysis of the results from the one-off nitrogen fertilization on a global scale. The globally integrated effects of the 32 simulations are examined and compared, with an additional exploration of spatial patterns in two distinct simulations. An aggregated outcome is derived, serving as a basis for assessing the feasibility and overall potential of one-off nitrogen fertilization as a global CDR strategy. The single extended simulation indicated that the long-term carbon storage after a 50-year period is twice as high as after the initial 5 years.

6 | High-potential locations for delivery

The previous chapter examined the one-off ocean nitrogen fertilization simulations on a global scale. Field trials and initial implementation of ocean nitrogen fertilization would start at specific locations. The choice of these sites is influenced not just by their carbon storage potential but also by practical considerations. The aim of this chapter is to identify high-potential locations for ocean nitrogen fertilization to which the delivery of the nitrogen is considered to be energetically and economically viable. A 'high-potential' location is here defined as a location with a combination of a relatively large absolute carbon sequestration capacity and a large C_{LT}/N efficiency ratio.

6.1. Identify locations

A crucial factor in evaluating the potential and viability of ocean nitrogen fertilization is the transportation of nutrients. Shipping traffic can play a vital role in delivering nutrients to fertilization sites. Hence, this section aims to pinpoint locations with the largest potential, taking into account both carbon sequestration capabilities and geographical suitability.

The delivery of nutrients can not only carry significant economic costs, but also contributes to carbon emissions, offsetting the carbon dioxide removal achieved through ocean fertilization. Hence, the aim is to locate regions with significant carbon sequestration potential that coincide with high-intensity mobilisation routes. This alignment allows for the transportation of nitrogen on routes the ships would have navigated regardless (but empty), thereby limiting additional financial expenses and emissions for these trips.

Figure 6.1 shows the vessel density map of the Automatic Identification System (AIS, a vessel tracking system). Different colours indicate a different density, with the red colour indicating the highest density. Seven high-intensity mobilisation routes for different basins, that overlap with the regions in the model computations, are marked by the black lines in Figure 6.1.
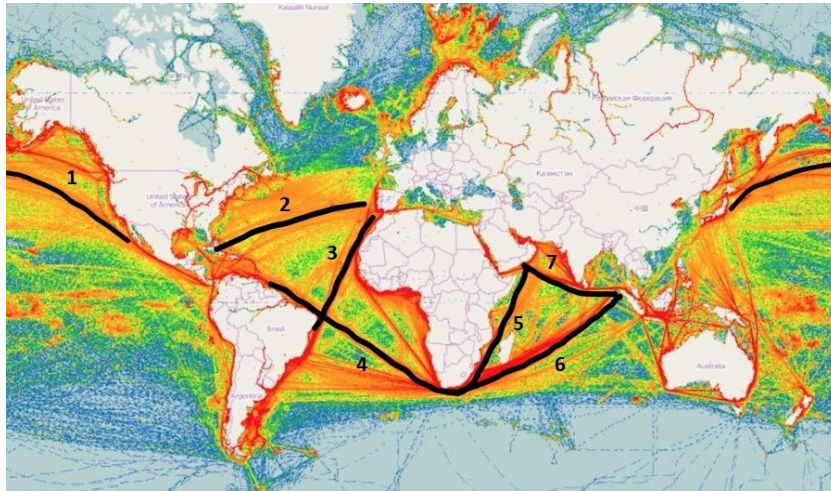
Figure 6.1: Global Automatic Identification System (AIS) density map showing the intensity of global vessel traffic. The colour scheme indicates varying levels of density, with green representing the lowest, orange indicating medium, and red signifying the highest vessel concentrations. The main (high-intensity) mobilisation routes are marked by the black lines. Figure adapted from openweathermap.org

For each of the seven mobilisation routes, the hexagon with the highest potential is sought to be identified. In this analysis, the average results from the nitrogen additions conducted at the start of the winter (January) and summer (July) season are employed, each comprising 8 simulations. The average results of these specific fertilization simulations are used, as the largest absolute sequestration potential is found for the Northern (Southern) Hemisphere in the fertilizations performed in January (July) (Figure 5.1a).

In Figure 6.2, the long-term carbon storage (upper figures) and the C_{LT}/N ratio (lower figures) of these averaged nitrogen additions are displayed. The left column figures are from the averaged nitrogen additions in January, and the right column from July. The transparent black lines in the upper figures represent the mobilisation routes. For each route the location with the largest potential for one-off nitrogen fertilization and the associated timing is identified, and presented as an open circle in the respective column in Figure 6.2. For each hexagon identified, the (averaged) long-term carbon sequestration, required nitrogen and C_{LT}/N are provided in Table 6.1. For mobilisation route 3 (between South America and West Africa/South Europe), no noteworthy fertilization location is found.
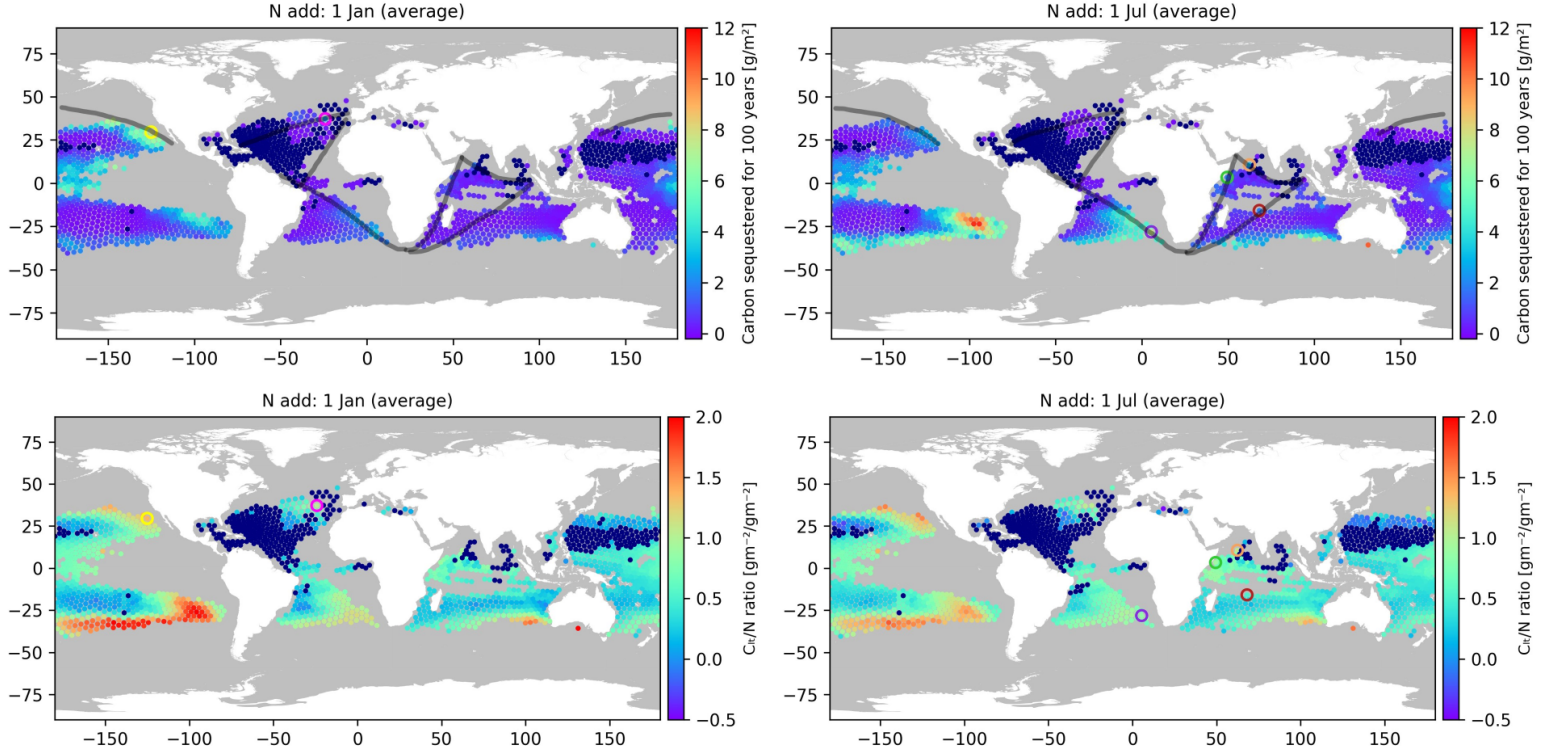
Figure 6.2: The long-term carbon sequestration (upper figures) and C_{LT}/N (lower figures) from the averaged nitrogen fertilizations performed at the start of January and July. The left column figures are from the averaged nitrogen additions in January and the right column figures are from the averaged nitrogen additions in July. The black lines in the upper figures represent the mobilisation routes. For each mobilisation route the location with the largest potential for one-off nitrogen fertilization and the associated timing is identified, and presented as an open circle in the respective column. In the dark blue hexagons no nitrogen addition took place, since there was no nitrogen limitation in their mixed layers at the moment of fertilization.

Mobilisation Route	Colour	Lat, Lon	Month	Long-term C seq [g/m^2]	N added [g/m^2]	C_{LT}/N
1	Yellow	29.6° N, 125.1° W	Jan	7.93	5.78	1.37
2	Pink	37.2° N, 24.2° W	Jan	2.45	2.42	1.01
3	-	-	-	-	-	-
4	Purple	28.2° S, 5.4° E	Jul	7.74	9.07	0.88
5	Green	3.3° N, 49.4° E	Jul	1.79	1.96	0.91
6	Red	15.9° S, 68.1° E	Jul	1.84	3.67	0.5
7	Orange	10.6° N, 62.4° E	Jul	3.01	2.76	1.09

Table 6.1: Details of the highest potential (averaged) nitrogen fertilization locations displayed in Figure 6.2 that overlap with global shipping high-intensity mobilisation route. The latitude and longitude represent the mid point of each hexagon. The month specified represents the timing at which nitrogen fertilization was done.

In summary, specific locations are identified where the delivery of nitrogen is expected to be most feasible. Chapter 7 further assesses the commercial viability of implementing a one-off fertilization at one of these identified locations.

7 | Analysis on feasibility

In this chapter, an initial analysis is made of the feasibility of one-off nitrogen fertilization within the global CDR context and its prospects as a potential business opportunity. Section 7.1 explores the global perspective by examining different fertilizers, as it is anticipated to represent the primary challenge in this context. In section 7.2, the delivery emissions and costs associated with implementing the strategy at a single location are determined and balanced against the carbon storage and financial gains.

7.1. Global CDR perspective: use and impact of fertilizer

In section 5.3, a global aggregated outcome of the one-off nitrogen fertilization simulations was derived. This analysis obtained that one-off fertilizing the remaining ocean areas (C_{LT}/N > 0.3) with 0.20 Gt of nitrogen results in the long-term storage of 0.16 Gt of carbon within a 5-year period following the fertilization. This means that the addition of 1 kg of nitrogen (on average) results in the long-term storage of 0.8 kg of carbon after 5 years. This amount of carbon is equivalent to 2.95 kg of CO_2. Therefore, 2.95 kg CO_2 is stored per kg of nitrogen. However, it is crucial to note that (bio-available) nitrogen is not available as a pure product; it must be either industrially produced or obtained from natural (by)products. Below the availability and impact of two different fertilizers is discussed.

7.1.1. Urea

A widely used nitrogen fertilizer is urea ($(NH_2)_2CO$), which has a nitrogen content of 46% (University of Minnesota Extension, 2021). Using the aggregated efficiency, this implies that each kilogram of added urea results in the long-term storage of 1.37 kg of CO_2 (within 5 years following the fertilization). However, the production of urea is CO_2 emission-intensive due to the use of natural gas for the production of ammonia, an intermediate product in the production of urea. Additionally, carbon captured in urea is released upon application. Research by Hoxha, Christensen, et al. (2019) indicates that the total CO_2 footprint varies between 1.484 and 3.002 kg per kg of urea, depending on the continent of production. Consequently, with the current production methods, the use of urea for one-off nitrogen fertilization results in a negative carbon storage. In other words, the CO_2 emissions from current urea production and carbon release during application outweigh the long-term CO_2 sequestration achieved by enhancing the biological carbon pump.

Urea might one day hold the potential for 'green' production methods through the integration of renewables and CO_2 from carbon capture. This approach could substantially diminish the carbon footprint associated with urea production, consequently leading to a positive CDR capacity for ocean nitrogen fertilization using urea. The eventual efficiency hinges on the degree of sustainability in its production processes. However, it is already a considerable challenge for the current urea production to transition to green methods. To achieve the long-term storage of 0.59 Gt of CO_2, 0.43 Gt of urea would be required. This is more than twice the amount of urea currently produced each year (Statista, 2023).

7.1.2. Manure

Instead of producing urea, animal manure ('waste' urea) could be used as fertilizer. Manure can be considered as a 'waste stream', and it not associated with additional CO_2 emissions that offset the stored CO_2 by ocean fertilization. However, manure, when not further processed, contains only a very small percentage of nitrogen. While it depends on the animal, (solid) manure has a nitrogen content of 0.6% (Grönroos et al., 2009). This implies that the addition of 1 kg of manure to the remaining ocean area results in 0.018 kg of CO_2 storage. A very low, but positive efficiency.

Using the nitrogen content in the global manure production of Chávez-Fuentes et al. (2017), and assuming that 30% of this manure is not reused on a global scale (in Europe it is 10% (Köninger et al., 2021)), it is estimated that the globally unused manure contains 0.045 Gt of N. This is nearly a quarter of the amount of nitrogen of the aggregated fertilization outcome, suggesting considerable promise as a potential fertilizer source. Nevertheless, the global logistics of collection of this manure presents considerable challenges. Moreover, it is argued that this unused manure should be utilised in agriculture itself to enhance its circularity (e.g. Leenstra et al. (2019)).

In summary, the potential use of urea and manure as fertilizers is elucidated in this section, shedding light on their effects on carbon sequestration potential and efficiency. Furthermore, the global availability and challenges associated with their utilisation are addressed.

7.2. Assessment of viability for commercial implementation

This section examines for one of the identified locations in Chapter 6 if the one-off nitrogen fertilization can be viable for commercial implementation. The assessment involves determining the price per net stored tonne of CO_2, and subsequently comparing it to the current market price of a carbon credit. Carbon credits enable companies to (mandatory or voluntary) reduce their carbon footprint, and one credit represents one tonne of CO_2 (Climate Trade, 2023). The example assessment focuses on the mobilisation for a (future) Van Oord project, and therefore their vessel (capacity, consumption and cost) data and route is used. All details and calculations are given below, but first relevant assumptions are presented.

Assumptions

- For this assessment manure is used as fertilizer. As discussed in the previous section, the CO_2 emissions associated with the current urea production already outweigh the CO_2 sequestered, and urea is therefore not a viable option. For this calculation it is assumed that the manure is free, and no processing of manure takes place.
- For this assessment, the assumption is made that the vessel is not scheduled for use at the time of application. Consequently, there are no extra costs associated with the usage time of the vessel (which can be very high), only for the additional fuel.

Mobilisation route for project: the Netherlands - Suriname

This example calculation focuses on a dredging project of Van Oord regarding a port in Suriname. For this project the vessel has to mobilise from Rotterdam to Suriname, exactly crossing the identified hexagon of route 2 (pink circle in Figure 6.2). The mobilisation and the specific location are presented in Figure 7.1. The (fertilization) details of this hexagon, as presented in Table 6.1, are repeated below. The (otherwise empty) vessel can therefore transport manure towards this location and apply it to sequester CO_2 using this CDR strategy.

Lat, Lon:	37.2° N, 24.2° W
Long-term C seq [g/m^2]:	2.45
N added [g/m^2]:	2.42
C_{LT}/N:	1.01
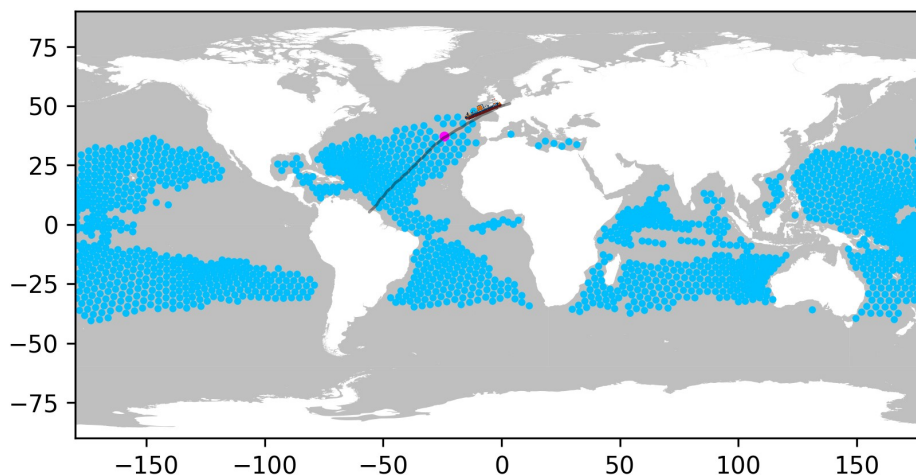
Figure 7.1: Mobilisation of an otherwise empty vessel from the Netherlands to Suriname, crossing the 'high-potential' hexagon at 37.2° N, 24.2° W.

CO$_2$ sequestration potential of one vessel
For this calculation the XL vessel of Van Oord is used, which has a capacity of 20,000 m^3. Assuming that manure has a density of 1000 kg/m^3 (Wang et al., 2019) results in that this vessel can transport 20,000 tonnes of manure. This amount of manure has a total nitrogen content of 120 tonnes. At this location the C$_{LT}$/N efficiency is 1.01, which implies that 121.1 tonnes carbon can be sequestered, which is equivalent to *444.1 tonnes CO$_2$*

Additional fuel consumption: emissions and costs
When a vessel speed of 12 knots is applied, the difference in fuel consumption between a loaded and empty ship is 289 L/h. The distance from the Netherlands to the hexagon is 2700 km. Upon computing the area that can be fertilized with the aforementioned quantity of nitrogen and considering a swath width of 600 m (as used in an iron fertilization experiment (Lawrence, 2014)), it is noted that no additional distance is required to be covered for the distribution of the manure itself. Travelling a distance of 2700 km with this speed takes 121 hours, and thus 34969 liter of additional fuel (MGO) is required. This is equal to 30 tonnes fuel.

3.15 tonnes of CO$_2$ are emitted per tonne fuel (International Maritime Organization, 2015), which results in the emission of *94.5 tonnes CO$_2$*. This implies a net positive CDR, since more CO$_2$ is stored than emitted.

The fuel costs amount to 778 euros per tonne, resulting in total costs of *23,340 euros*

Price per net tonne CO$_2$ sequestered versus price of carbon credit
The net CO$_2$ sequestration equals 349.6 tonnes, resulting in a cost of 67 euros per tonne of CO$_2$ sequestered. Comparatively, the current European carbon credit price stands at 74 euros per tonne of CO$_2$ (CarbonCredits.com, 2023).

This initial assessment indicates that costs of purchasing a carbon credit exceed the cost of implementing one-off nitrogen fertilization for this particular case. Consequently, it implies that one-off nitrogen fertilization using manure can be a viable commercial CDR approach.

Part III

Synthesis

8 | Discussion

This chapter discusses the results presented in Part II. The main results are interpreted in section 8.1. Section 8.2 addresses the limitations of this study. The implications of the findings are discussed in section 8.3. First, a recap of the study's objective is provided.

The objective of this thesis is to quantify the CDR potential of one-off ocean nitrogen fertilization achieved within a 5-year period following the fertilization, addressing both the global CDR perspective and the potential for commercial implementation.

8.1. Interpretation of the results

Sub-questions 3 and 4, as stated in 1.4, are explored by referring to the main findings of Part II. First, the global carbon sequestration outcomes from the simulations (Chapter 5) are interpreted in 8.1.1. Then the overall global carbon sequestration potential from one-off ocean nitrogen fertilization is evaluated by combining the findings from Chapter 5 and 7 (section 8.1.2). The 'high-potential' locations identified for transportation, along with the viability assessment conducted for one of them, are discussed in 8.1.3.

8.1.1. Global long-term carbon sequestration from the simulations

This thesis finds that the global long-term carbon sequestration of one-off nitrogen fertilization achieved within a 5-year period following the addition, ranges between 0.07 and 0.18 Gt for the 32 simulations. This spread can mainly be attributed to the different seasons of nitrogen addition. The 8 simulations in which nitrogen was added on the 1st of July were characterized by the highest absolute sequestration, but also the largest nitrogen inputs and mostly slightly lower C_{LT}/N ratios compared to other seasons.

Various thermocline diffusivities were employed in the simulations to assess their impact on the fertilization outcomes. The range between the most extreme diffusivity values spanned a factor of 10. When comparing the globally integrated long-term carbon sequestration and the global C_{LT}/N ratio of nitrogen fertilization simulations that shared the same nitrogen addition timing and spin-up but differed in thermocline diffusivity (called a set in chapter 5), the observed variations were at most a factor 2 and 1.7, respectively. Regarding the C_{LT}/N ratios of a set, the lowest values were mostly found for simulations with 10^{-4} m^{2}s^{-1} as thermocline diffusivity. In contrast, the differences in the normalized offset of the nitrogen addition (perturbation) caused by reduced nitrogen fixation were more significant within a set. The variation in offset was expected, given the significant differences in nitrogen fixation between the baseline simulations (D.1 to D.4).

While direct comparisons between the C_{LT}/N ratios of different thermocline diffusivity simulations may not be straightforward, as they are also associated with different nitrogen inputs, it is remarkable that the C_{LT}/N efficiency ratios differ at most by a factor of 1.7 within a set and that C_{LT}/N is generally lowest for the highest diffusivity. This is in light of the substantial differences in normalized offsetting feedback due to decreased N fixation and the clear reduction in offset with higher thermocline diffusivity. This suggests that for higher thermocline diffusivities other factors may exert a dominant influence on regulating the C_{LT}/N ratio. We speculate that in the simulations with a higher thermocline eddy diffusivity the nitrogen addition may lead to a considerable decrease in upward flux of nitrogen (due to the decrease in nutrient gradient) which would otherwise have occurred 'naturally'. This speculation could potentially be supported by the observations made when comparing the spatial patterns of two simulations with each one of the extreme used thermocline diffusivities. Specific zones

(e.g. small region in South Eastern Pacific) that exhibit no offset from reduced nitrogen fixation in both simulations reveal pronounced variations in C_{LT}/N efficiency. For these zones a relatively large efficiency was observed in $D_{thermo} = 10^{-5}$ m^2s^{-1}, while minimal efficiency was found in $D_{thermo} = 10^{-4}$ m^2s^{-1}, which might suggest that for the higher diffusivity a decreased upward 'natural' nitrogen flux plays a major role.

Regarding the different spin-up times, a smaller normalized offset due to reduced nitrogen fixation was found for the simulations adopting 4 full years of baseline simulation spin-up compared to 1 year. This observation aligns with our expectations, considering the annual reduction in N fixation noted in the baseline simulations. For the simulations employing the two lowest thermocline diffusivities (10^{-5} and $3\cdot10^{-5}$ m^2s^{-1}) higher C_{LT}/N ratio for the 4 years spin-up simulations were concurrently observed, while for the two higher diffusivities this was (mostly) not found. This is in line with the suggestion made above that another factor than the offset by reduced N fixation mainly regulates the C_{LT}/N ratio for higher D_{thermo} values.

In none of the 32 fertilization simulations a nitrogen limitation was found in the mixed layers in (a part of) the Western Tropical North Atlantic. While phosphorous is often considered to be depleted alongside nitrogen in this region (Ammerman et al., 2003; Moore et al., 2013) (see Figure 1.5), it is remarkable that no nitrogen limitation at all was observed in the mixed layer. This might imply that the lateral surface supply of phosphorous is dominant in this region, which is also stated by Letscher et al. (2016).

A global aggregated ('final estimate') outcome of nitrogen fertilization was derived by averaging over the 8 fertilizations performed in July while excluding locations with a C_{LT}/N efficiency below 0.3. After exclusion of these 'low-efficiency' hexagons, the long-term carbon sequestration, C_{LT}/N efficiency and normalized offset from reduced nitrogen fixation of these simulations ranged between 0.14 Gt - 0.18 Gt, 0.6 - 1.04 and 1% - 17%, respectively. After averaging the aggregated outcome was obtained. It was found that 5 years after the one-off fertilization with 0.20 Gt of nitrogen, a long-term carbon storage of 0.16 Gt is reached, and 6% of this nitrogen perturbation is decreased due to reduced nitrogen fixation. These values imply that (on average) for every kg of nitrogen added, 0.8 kg of long-term carbon storage is achieved within a 5-year period after fertilization. Translated to CO_2, this equates to 2.95 kg. To put this into perspective, if all the added nitrogen would have led to long-term carbon storage, 1 kg of fertilized nitrogen results in 5.68 kg of carbon sequestration. Reviewing Figure 5.5, less than half of the hexagons initially considered in the model computations are retained. This subset of hexagons represents approximately 15% of the global ocean. It is suggested that the excluded hexagons, labeled 'low-efficiency', can be largely disregarded in future nitrogen fertilization research. However, the Western Tropical North Atlantic could be considered, as the absence of nitrogen limitation is likely inaccurate.

Because of the scarcity of research into carbon sequestration with (one-off) ocean nitrogen fertilization and the specific research set-up to identify (only) the long-term sequestration, it is difficult to make direct comparisons with existing literature. However, the findings are in line with that the BCP is mostly associated with storage timescales shorter than 100 years, since the aggregated values reveal that only 14% (0.8/5.68*100%) of the nitrogen's total long-term carbon storage potential is reached after 5 years. In the extended simulation, cumulative long-term carbon sequestration from nitrogen addition is approximately twice as high after 50 years compared to after 5 years, but this is still far from the full efficiency. It is likely to take on the order of thousands of years before all nitrogen (simultaneously) contributes to long-term carbon storage, as the organic matter flux to the seafloor becomes significant on that timescale (Sigman & Hain, 2012).

8.1.2. Evaluation of the overall global long-term carbon sequestration potential from one-off nitrogen fertilization

First of all, it is crucial to assess how the aggregated outcome from the one-off nitrogen fertilization contributes to global CDR targets. The derived 0.16 Gt of long-term carbon sequestration is equivalent to 0.59 Gt of CO_2. This value represents 8% of the annual global CO_2 removal target, and a doubling is predicted after 50 years. While this denotes a noteworthy contribution, it underscores the need for

repeated additions, for example on an annual basis, to make this approach truly impactful in the context of a global CDR strategy.

With this in mind, the overall global carbon sequestration potential from nitrogen fertilization can be addressed by considering the (necessary) use of a fertilizer, focusing on the fertilizers urea and manure as discussed in Chapter 7. Considering the current urea production methods, the application of nitrogen fertilization with urea is not a feasible option. The CO_2 emissions related to the urea production and application outweigh the long-term CO_2 storage achieved through this approach. In a future scenario with sustainable urea production, leading to a significant reduction in its carbon footprint, utilising urea for ocean nitrogen fertilization would yield a net positive carbon storage. However, leveraging the limited renewable resources (International Energy Agency, 2021) to (minimally) triple the global urea production in order to achieve the 0.59 Gt of CO_2 storage on a yearly basis is not anticipated to be a priority in meeting the goals of the Paris Agreement. In light of these considerations, the present global carbon sequestration potential of one-off nitrogen fertilization with urea is negative, and is expected to persist at a low level in the future.

In section 7.1 it was determined that a quarter of 0.20 Gt of nitrogen (the aggregated nitrogen amount) is yearly available in unused manure worldwide. While with this amount of nitrogen available in this 'waste stream' (at least) 2% of the annual CDR target can be achieved, the associated global logistic challenges raise concerns about prioritizing manure use for a global CDR technique. It is also essential to note that this surplus nitrogen should be used more efficiently in agriculture to address the planetary boundary for nitrogen use exceedance, as emphasized by Schulte-Uebbing et al. (2022). In consideration of these factors, the global carbon sequestration potential using manure for one-off fertilization is also deemed low.

Given the CO_2 footprint of current urea and the 'limited' global (additional) availability of 'green' nitrogen fertilizers, the evaluation points to a low overall global carbon sequestration potential for the one-off nitrogen fertilization approach.

8.1.3. Viable locations for commercial implementation

Transportation by vessels involves both financial expenses and CO_2 emissions. Limiting these aspects is crucial to make the delivery of the nitrogen viable (for commercial implementation). The considered approach is to use vessels that would have navigated without cargo otherwise. Therefore, for the high-intensity mobilisation routes of global shipping (which also overlap with those of Van Oord), the location and timing of the highest-potential nitrogen fertilization experiment were identified using averaged simulation outcomes. A 'high-potential' location was defined as a location with a combination of a relatively large absolute carbon sequestration and a large C_{LT}/N.

The majority of the identified locations demonstrate a C_{LT}/N efficiency larger than the obtained global aggregated efficiency. However, most locations are not necessarily characterized by a high absolute carbon sequestration when compared to globally observed values, with the exception of for example the hexagon en route from North America to Asia. Furthermore, the South Eastern Pacific, which can be identified as the highest potential region from a BCP carbon storage perspective, is not crossed by a major global shipping route.

A feasibility assessment involving a Van Oord vessel crossing one of the identified locations revealed that implementing one-off nitrogen fertilization using (the free waste steam) manure presents a viable business opportunity. The amount of CO_2 that can be sequestered substantially surpasses the (additional) emissions from vessel transportation. The eventual cost per net tonne of stored CO_2 on the other hand relatively closely aligns with the current carbon credit price. Costs could be lower if manure collection occurred en route (instead of at the departure location), reducing additional fuel needs. However, the observed proximity in pricing primarily suggests that the implementation of the strategy is economically viable only under the assumption of zero additional costs for vessel usage, as applied in the assessment. If the vessel operates on a tight schedule and the high usage costs need to be paid, the CDR strategy might not be economically feasible compared to the current carbon credit price. Nevertheless, the carbon credit price is expected to rise significantly in the coming decade(s) (Surname et al., 2022),

meaning that there is more leeway for operational costs.

8.2. Limitations of the study

This study is not without constraints and limitations. These inherent limitations stem from the necessary assumptions and choices made mostly related to the model framework and experimental design to facilitate this relatively concise study. This section addresses the main limitations, and discusses their potential impact on the (simulation) results.

8.2.1. Model framework set-up

Here the key limitations from the used model framework are discussed, which mainly arose from aspects of the marine ecosystem and physical model.

Marine ecosystem model

In this thesis, the marine ecosystem model of Keller et al. (2012) was used. This model incorporates the dynamics of the nitrogen cycle and competition for phosphorus, which are essential when studying nitrogen fertilization. However, it has to be noted that this model offers a relatively idealized representation of reality. Contrarily, a higher model complexity does not necessarily increase the performance, as emphasized by Kriest et al. (2010).

Nevertheless, it is important to acknowledge that the model uses an iron mask to constrain phytoplankton growth, and does not include the iron cycle and associated feedbacks. This means that a higher NPP, an observed result from nitrogen fertilization (since the additional remineralization implies additional production), does not lead to a lower iron concentration. In (sub)tropical oceans, which are the regions primarily included in the simulations, it is often observed that iron is the next limiting nutrient after nitrogen or even co-limiting with nitrogen (see Figure 1.5) (Browning & Moore, 2023; Browning et al., 2017). This co-limitation is for example found in proximity to the high potential carbon sequestration regions in the South Eastern Pacific and Atlantic. Hence, the long-term carbon sequestration results on the hexagonal and global scale may be overestimated by not accounting for the iron cycle in the ecosystem model.

To provide a conservative estimate of the effect on the aggregated carbon sequestration value, it is assumed that if the iron cycle had been incorporated, the carbon sequestration in the hexagons within these South Eastern Pacific and Atlantic Ocean areas (20° - 35° S, 75° - 100°W and 20° - 35° S, 5° W - 10° E) would be only 50% of what was found. When this storage reduction is taken into account when determining the aggregated long-term carbon sequestration value, it yields 0.15 Gt instead of the 0.16 Gt presented in sections 5.3 and 8.1.1.

Furthermore, this marine ecosystem model is normally embedded in the UVic 3D ocean model, and therefore validated inside that specific ocean model. While it should be possible to use the ecosystem model separate from UVic ESCM, employed biochemical parameters are often connected to the model it is built in. Due to this connection, there is a risk that using the ecosystem model independently could introduce inaccuracies into our results.

Physical model

The only physical transport mechanism included in the model to simulate nutrient supply is vertical eddy diffusion. For this physical model the stratified ocean was considered as a three-layer system consisting of the surface mixed layer, the thermocline layer and the deep ocean layer. Each layer is characterized by its own constant eddy diffusivity. For the mixed layer and the deep ocean their global average values were used, and for the thermocline a range of diffusivities was used to account for some uncertainty and assess the sensitivity of the results to this selection. This physical model set-up is a highly idealized representation of the vertical eddy diffusion in reality, for example because eddy diffusivities are highly variable in both time and space. Also, regarding the baseline simulations the different thermocline diffusivities resulted in significant differences in ecosystem productivity. However, it is found that the global carbon sequestration results from simulations employing a different thermocline diffusivity differ at most a factor 2, while the diffusivities differ at most a factor 10. Local differences in magnitude are overall also less pronounced than this tenfold factor. This suggests that in the context of this study, where fertilization and baseline simulations are compared to assess the impact of nitrogen

fertilization, the thermocline diffusivity does not appear to have a first order effect, at least on short timescales.

A limitation inherent to solely including 1D vertical diffusion in the physical model, is the necessity to exclude oceanic regions where horizontal surface transport (advection) is believed to play a dominant role in nutrient supply. Consequently, a filtering criterion was applied that resulted in the exclusion of 969 hexagons that would otherwise have passed the remaining filtering criteria. When surface advection was introduced as a transport mechanism, resulting in the inclusion of more hexagons in the fertilization simulations, the global carbon sequestration from the one-off nitrogen fertilization might be substantially higher, but also requiring larger nitrogen inputs. Of the 969 excluded hexagons, half of them overlap with areas prone to nitrogen fixation or denitrification (compare Figures 1.6 and 2.8). These areas would not significantly contribute to the carbon sequestration potential because the added nitrogen fertilizer would be offset due to reduced fixation, or the hexagons would be excluded upfront. The other half of the hexagons could contribute to the carbon sequestration potential. Hence, it is estimated that the global carbon sequestration has the potential to double. For the overall evaluation, it is more of interest whether the global efficiency might (substantially) increase. However, given the sequestration fractions of the respective areas as shown in Figure 1.3, it is assumed that the global efficiency would remain relatively comparable.

For the hexagons that did meet the inclusion criteria (nutrient gradient smaller than the global median, see section 2.5), it is relevant to explore the potential impact on the carbon sequestration outcomes if advection would have been included. Assuming an average speed of ocean surface currents of 10 cm/s (The European Space Agency, 2012), and a hexagon diagonal of 332 km, the water renewal time of a hexagon is 38 days. Because the nitrogen is fertilized all at once, and most of the added nitrogen is likely recycled in the upper ocean (multiple times) before it is exported to the interior, it is plausible that part of the nitrogen fertilized to a hexagon circulates to other hexagons within the 5 year time frame. If the added nitrogen from hexagons with little/no offset due to reduced N fixation circulates to hexagons where this offset can be substantial, the (global) carbon sequestration might decrease. But the opposite can also occur (fertilized nitrogen circulates from regions with high N fixation offset to regions with low/no N fixation offset). Considering that subtropical gyres exhibit surface convergence (inward currents toward the center) and nitrogen fixation offsets are larger in the centers (see Figure D.1 and Figures in E.2.2), it is speculated that the likelihood of a decrease in carbon sequestration is higher. The horizontal transport can also lead to the production of organic matter in another location or the transportation of it to another zone, which can influence the amount and duration of the carbon storage.

It is also noteworthy that the regions with high carbon sequestration potential in the North and South Eastern Pacific, as well as identified 'high-potential' implementation hexagons close to the Arabian Sea, are located in proximate to oxygen minimum zones, where denitrification actively takes place. Although the main current direction around the equatorial Pacific is westward (Ocean Motion NASA, 2023), part of the nitrogen added to these different regions could reach the OMZs and potentially result in a localized net fixed nitrogen loss, thereby it might diminish the carbon sequestration.

To investigate these effects on the local nitrogen additions in detail, research with a 3D ocean model is essential and extended simulations are necessary, given that the impact of denitrification becomes evident over a longer time scale.

No CO_2 air-ocean transfer

In order for ocean nitrogen fertilization to lead to climate change mitigation, the export of carbon from the surface ocean to the interior must result in the oceanic uptake of CO_2 from the atmosphere. CO_2 can only be taken up in the surface ocean. The transfer efficiency is determined by the residence time of fertilised water in the surface ocean and the transfer time of CO_2 to cross the air-ocean interface. This aspect is not included in this study. Prior research indicates that the residence time considerably surpasses the transfer time (Lawrence, 2014), thus all carbon exported out of the surface ocean will eventually be compensated by the uptake of CO_2 from the atmosphere. However, the transfer time can extend over several months (Jones et al., 2014), and raises the possibility that not all the long-term exported carbon (away from the surface ocean) is already compensated by the uptake of carbon dioxide from the atmosphere in the surface ocean.

8.2.2. Experimental design
In this thesis, the choice of a highly specific experimental design influences and constrains the results. Notably, this includes considerations related to nitrogen fertilization quantities. While increasing the nitrogen input might have raised the (global) carbon sequestration value, it would also have required a greater quantity of nitrogen. The C_{LT}/N ratio might be lower than the current aggregated efficiency when larger quantities of nitrogen would be used, as the July addition simulations with notably higher nitrogen inputs than other seasons generally exhibited a slightly lower efficiency.

Start baseline simulations
Because of time considerations, only four baseline simulations were performed, each starting on the 1st of January. This means that the state variables in each baseline simulation were initialised with the climatologies of the corresponding season. When the baseline simulations would have started in a different season, this could potentially have altered the results. This is because the amount of nutrients in the water column is not necessarily the same in each season, whereas the 1DV model keeps the total phosphorus content within a hexagon constant during the simulations. A different baseline simulation starting moment could therefore have led to a different P to N ratio in the mixed layer at the moment of fertilization. Consequently, the total carbon sequestration might have been either higher or lower. However, the efficiency is likely to be similar.

8.2.3. Global carbon sequestration analysis
In the analysis of globally integrated carbon sequestration values (as presented in Chapter 5), the focus was on individual fertilization simulations. Also, when establishing the aggregated fertilization outcome in section 5.3, the average of the fertilizations conducted in July was used. However, if the most favorable moment (highest C_{LT}/N efficiency) of nitrogen addition was selected for each hexagon individually and these results were then combined to calculate global fertilization values, a potentially larger global carbon storage efficiency might have been uncovered. Upon examining the figures in Appendix E.2, it is estimated that the enhanced efficiency is not expected to exceed a 15-20 % increase.

In retrospect, the limitations and their impacts outlined in this section broadly fall into two main categories: (1) considerations that could potentially enhance the long-term carbon sequestration value while requiring a larger nitrogen input and (2) aspects that may lead to different sequestration efficiencies given the current nitrogen inputs. Focusing on the limitations falling into the second category and considering the efficiency spread of the July addition simulations used to derive the aggregated outcome (see 8.1.1), it is suggested that the aggregated 'final estimate' C_{LT}/N efficiency of the remaining ocean regions, currently at 0.8 (indicating 0.8 kg of long-term carbon sequestration reached within 5 years per kg N added), may exhibit a maximum variation of up to 50% increase or decrease. This means that even when the efficiency exhibits the (unlikely) maximum increase, the CO_2 footprint of the current urea production is only a bit lower or still outweighs the long-term CO_2 sequestration that can be achieved (depending on the continent of production).
The local (hexagonal) efficiency range is influenced by the geographic location. In terms of the commercial viability of a location for implementing ocean nitrogen fertilization, even a subtle change might determine whether it is viable or not, particularly in the context of current carbon credit prices. This underscores the need for further research using a less idealized model, aiming to yield more precise values for carbon sequestration in the specific locations of interest.
The initial quantification provided in this study, while inherently constrained in scope and subject to certain limitations, serves as a valuable addition to the scarcity of research in the domain of ocean nitrogen fertilization. This study offers insights into the carbon dioxide removal potential of this strategy, laying the groundwork for further research.

8.3. Potential implications & further research
The findings and evaluations of this thesis indicate that ocean nitrogen fertilization has very limited potential to serve as a large-scale global carbon dioxide removal strategy. In principle, the nitrogen fertilization 'itself' demonstrates an effective carbon sequestration efficiency (2.95 kg CO_2 per kg N). However, the high and challenging-to-reduce carbon footprint of current urea production, coupled with

challenges in collecting manure and the priority of utilising it in agriculture rather than directing it for carbon removal, implies that ocean nitrogen fertilization is not a feasible global CDR approach.

It is crucial to note, however, that no single technique alone has the capacity to remove the necessary amounts of CO_2 from the atmosphere (as outlined in e.g. Meyer-Ohlendorf (2021)). To contextualize the 0.59 Gt of CO_2 sequestration in terms of an alternative CDR technique as reforestation for example, approximately 26.8 billion trees would need to be planted to reach this amount of sequestration (using Moseman and Harvey (2022)). This is less than 1% of the 3 trillion trees the Earth currently hosts (Crowther et al., 2015), but more than 14 times the number of trees currently planted each year (Kilgore, 2023). And also forestation faces its own set of challenges (e.g. Doelman et al. (2020) and Peborgh (2021)). Consequently, this underscores the continued importance for governmental and scientific bodies to explore global CDR strategies and their possible implementation, as the deployment of CDR technologies is inevitable if we aim to achieve the goals of the Paris Agreement.

Although ocean nitrogen fertilization is not a feasible global CDR technique, this study reveals that one-off nitrogen fertilization can be viable for commercial implementation. Consequently, in the presence of surplus manure with no agricultural purpose, such surplus could be utilised by (maritime) companies to implement nitrogen fertilization as a CDR method, thereby offsetting their hard-to-abate emissions and advancing toward their climate-neutral goals. The findings from this thesis offer guidance for identifying optimal locations to carry out these nitrogen fertilization additions. However, given the uncertainties and limitations inherent in the idealized model, as discussed in 8.2, more realistic modelling studies are necessary for an accurate assessment of carbon sequestration from nitrogen additions.

Furthermore, beyond the carbon sequestration aspect, it is crucial to consider the potential (negative) side effects of ocean fertilization to evaluate it as a CDR strategy. Fertilization alters natural processes in the marine ecosystem, introducing modifications that may be perceived as unacceptable from an ecological and/or ethical standpoint, as introduced in section 1.1.5. Some of these impacts are highlighted below. It needs to be noted that these side effects are regarding ocean fertilization in general, not specifically the single one-off fertilization performed here:

- Ocean fertilization can lead to changes in the oceanic ecosystem structure and loss of biodiversity (National Academies of Sciences & Medicine, 2022). Fertilization would probably stimulate the production of a single/few phytoplankton type(s). This would lead to loss of biodiversity and it can modify the biological carbon pump and its sinking of organic matter. Also toxic algae blooms can occur (Glibert et al., 2008; Lampitt et al., 2008).

- Ocean fertilization can lead to the increased production of N_2O (Matear & Elliott, 2004; Secretariat of the Convention on Biological Diversity, 2009). N_2O is produced as a result of incomplete denitrification (at the interface between suboxic and anoxic waters) (Freing et al., 2012). As ocean fertilization enhances the export of organic matter, it leads to a larger oxygen consumption in the ocean interior, resulting in decreased oxygen concentrations. This can contribute to the increased emission of N_2O. N_2O is a very strong greenhouse gas and has almost 300 times the global warming potential of CO_2 (Liang et al., 2015). It can therefore strongly offset the desired effect of ocean fertilization.

- The potential increase of low-oxygen zones described above, which are also called 'dead-zones', can also lead to a loss of biodiversity and fisheries, since most organisms need oxygen to survive (McCormack et al., 2016).

- Because ocean fertilization aims to increase the amount of CO_2 stored in the ocean, it has the potential to accelerate ocean acidification on longer time scales. Ocean acidification reduces calcification of organisms like corals and specific plankton types (Van de Waal et al., 2013). Fertilization can therefore have severe effects on the ocean ecosystem. This may also shift phytoplankton communities which has important implications for sinking organic matter. How the marine environment would exactly be affected by the change in pH is uncertain, but it can have significant effects on both the ecosystem and the carbon cycle (Lampitt et al., 2008).

Some of the aforementioned side effects can be linked to a reduction of the carbon sequestration potential due to modification of the BCP or the emission of another greenhouse gas. A comprehensive assessment is thus imperative before seriously considering the implementation of ocean nitrogen fertilization.

9 | Conclusions and recommendations

The conclusions from this study are presented in section 9.1. Furthermore, section 9.2 elaborates on the recommendations for further directions.

9.1. Conclusions

To limit global warming to well below 2 °C, the IPCC emphasizes the need for carbon dioxide removal alongside emissions reductions. This thesis investigated ocean nitrogen fertilization as CDR strategy, a research domain which so far has received little attention. The aim was to provide an initial rough quantification of the CDR potential of one-off ocean nitrogen fertilization achieved within a 5-year period after the addition, to evaluate its potential as a global CDR technique and for commercial implementation. The scope was narrowed to the use of an idealized 1DV model framework. To achieve this research objective multiple sub-questions were formulated, which are answered step-wise below.

1. How to establish a 1DV model framework with the minimal processes of ocean productivity and the biological carbon pump to assess the carbon sequestration from ocean nitrogen fertilization?
The essential processes to be included in the model framework are phytoplankton productivity, organic matter transfer through the ecosystem, sinking and remineralization at depth, and nutrient (re)supply. Specifically for nitrogen fertilization, the inclusion of processes from the nitrogen cycle is crucial. This was achieved by coupling an existing marine biochemical ecosystem model with the set-up 1DV physical circulation model. In the physical model vertical eddy diffusion served as the exclusive transport mechanism, considering the stratified ocean as a three-layer system – the surface mixed layer, the thermocline and the deep ocean – each assigned a constant eddy diffusivity. The layer boundaries were determined using oceanographic conditions. Global average eddy diffusivity values were used for the mixed layer and deep ocean, while four different values were employed for the thermocline to address uncertainty and yield sensitivity information. The long-term sequestration storage could be derived by post-processing the remineralization output with sequestration timescale fractions. To implement the model equations, the global ocean was discretized into 1DV hexagonal columns ($87 \cdot 10^3$ km^2 each), excluding half due to incompatibility with 1DV modelling. Regions not relevant for nitrogen fertilization were also excluded from the framework, with the primary criterion being the exclusion of areas where nitrogen is not the first limiting nutrient.

2. How to design the experimental set-up for the one-off nitrogen additions and associated simulations?
To assess the impact of one-off nitrogen fertilization, conducting simulations without (baseline simulations) and with nitrogen additions (fertilization simulations) was required. Four baseline simulations, one per thermocline diffusivity, of the BCP were performed to serve as model spin-up and as a basis for comparison (control simulation). In the fertilization simulations, nitrogen was added as a one-off pulse to all the included hexagons. Specifically, the chosen approach involved fully replenishing the nitrogen limitation in the mixed layer of each hexagon. The fertilization was conducted at four different moments (beginning of January, April, July, and October) to account for potential differences in nitrogen limitation associated with each season. Since in none of the baseline simulations a steady state was reached, a spin-up of 1 year and 4 years was adopted. In total, 8 fertilization simulations

per thermocline diffusivity were executed, resulting in 32 simulations each of 5-year duration. This experimental design plan facilitated a comprehensive assessment of the long-term carbon sequestration achieved within the initial 5 years after the addition. Additionally, a single 50-year simulation was performed to assess the long-term carbon storage after an extended period.

3. What is the global long-term carbon sequestration potential resulting from the nitrogen fertilization?
The simulations revealed a global long-term carbon sequestration achieved within 5 years after the fertilization ranging between 0.07 and 0.18 Gt. The efficiency of unit mass carbon sequestered per unit mass nitrogen added varied from 0.57 to 0.97. The spread in absolute sequestration values could mainly be attributed to the different seasons of nitrogen addition. The differences in carbon sequestration and the efficiency between simulations with varying diffusivity were generally less than twofold, suggesting that the thermocline diffusivity does not have a first-order effect on the results of this particular study. An aggregated outcome was derived by averaging over the fertilizations performed in July (which were characterized by a large absolute sequestration), while excluding hexagons with a low sequestration efficiency as these contribute insignificantly to CDR. This analysis leaves us with approximately 15% of the global ocean area. One-off fertilization of this area with 0.20 Gt of nitrogen yields 0.59 Gt of long-term CO_2 sequestration after 5 years, with 6% of the nitrogen addition offset due to reduced nitrogen fixation. Consequently, this implies (an average) sequestration of 2.95 kg of CO_2 per kg of nitrogen. The extended simulation suggested a potential doubling of the carbon sequestration over a 50-year period.
0.59 Gt of CO_2 represents 8% of annual global CO_2 removal target. Hence, e.g. annual repetition of the fertilization is required for this approach to be impactful in the context of a global CDR strategy, even accounting for the doubling effect after 50 years. The evaluation of the overall sequestration potential must account for fertilizers. The current carbon footprint of urea surpasses the sequestration capacity, yielding a negative CDR potential. In a future with sustainable urea production, using urea for ocean nitrogen fertilization could offer net positive carbon storage. Yet, tripling global urea production to reach 0.59 Gt of CO_2 sequestration yearly is not considered a priority in reaching the goals of the Paris Agreement given the limited availability of renewable resources. A quarter of the 0.20 Gt of nitrogen is available in unused manure. However, its collection poses substantial challenges, and it is preferable for agricultural use. In conclusion, the consideration of fertilizers reveals the low global long-term carbon sequestration potential from nitrogen fertilization.

4. To which locations is the delivery of the nitrogen energetically and economically viable?
'High-potential' locations were pinpointed that align with shipping mobilisation routes. Executing one-off nitrogen fertilization at these locations effectively limits financial expenses and emissions for transportation, as the delivery can be conducted by vessels that would have navigated the routes regardless but then in empty state. A feasibility assessment was conducted for one of these locations, indicating that fertilizing this site using manure is indeed commercially viable for implementation. The quantity of carbon dioxide that can be sequestered substantially exceeds the (additional) emissions from vessel transportation, and the cost per net tonne of CO_2 sequestered is lower than the current price of a carbon credit.

With the sub-questions answered, the main objective of this thesis can be addressed.

To quantify the CDR potential of one-off ocean nitrogen fertilization achieved within a 5-year period following the fertilization

Based on the findings of this study, it can be concluded that nitrogen fertilization has very limited potential to serve as a large-scale global carbon dioxide removal strategy. Nevertheless, this initial assessment of this study showed the viability of one-off nitrogen fertilization for commercial implementation. Consequently, when surplus manure lacks an agricultural purpose, (maritime) companies could leverage this surplus for nitrogen fertilization as a CDR method to become climate neutral. It is crucial to emphasize that this could be implemented in addition to substantial emissions reductions, not as a substitute. The outcomes of this study justify further detailed research into strategic nitrogen fertilization for company-level CDR. The insights provided by this thesis offer valuable guidance in pinpointing optimal locations for the focus of this further research.

9.2. Recommendations

A base is created for follow-up studies regarding this CDR strategy. This section presents important recommendations that follow from the discussions in Chapter 8 and the conclusions from the previous section, guiding the future directions of this study and extending to broader considerations.

9.2.1. Modelling studies

The initial quantification presented in this thesis highlights the potential of ocean nitrogen fertilization for company-level CDR. However, to enhance the accuracy of sequestration results, additional modelling studies are required. It is recommended that a climate model (e.g. UVic ESCM) is used. In this way, multiple limitations discussed in 8.2 can be addressed. With the integration of a 3D ocean circulation, the role of advection and other transport mechanisms in the conveyance of fertilized nitrogen and organic matter can be investigated, revealing insights in their effects on the nitrogen cycle and carbon sequestration. Furthermore, employing a climate model allows for the examination of changes in atmospheric CO_2 concentrations, which represent the ultimate objective of ocean fertilization and was not explicitly included in this thesis. We propose utilizing a marine biochemical model featuring dynamic iron cycling and a N_2O parameterization. Additionally, the inclusion of more phytoplankton groups is advised, considering that fertilization may induce a shift in species composition, potentially altering the BCP. One possible option is to use the ecosystem model of Kvale et al. (2021) combined with the N_2O parameterization provided by Landolfi et al. (2017). The nitrogen fertilization simulations need to focus only on (a few) strategic locations, in other words locations that align with mobilisation routes, and it is relevant to study their combined and individual effects.

9.2.2. Extended feasibility assessment

In the further investigation of the company-level CDR potential through nitrogen fertilization, a detailed analysis of the quantity and geographic distribution of 'purposeless' manure is imperative. Furthermore, in this study's preliminary evaluation of the commercial viability of nitrogen fertilization using manure, only ocean vessel transport was taken into account. However, the entire operational cycle involves additional stages, such as the collection, inland transport, and storage of the manure. For a comprehensive assessment of the energetic and economic viability of nitrogen fertilization, it is essential to map the costs and emissions associated with each facet of the process. Additionally, designing an efficient framework for the entire operational cycle is crucial.

Moreover, exploring the possibility of developing a nutrient-dense(r) fertilizer from the manure is of interest, as it has the potential to increase the carbon sequestration efficiency per unit mass of fertilizer. However, this process must be evaluated considering associated emissions and costs, making it meaningful only if it results in an overall decrease in the costs per net tonne of stored CO_2.

9.2.3. Field experiments

To date, no field experiments involving nitrogen fertilization have been conducted. Investigating the impact of nitrogen fertilization on ecosystem structure requires field experiments (Secretariat of the Convention on Biological Diversity, 2009). Also, manure, when unprocessed, contains more than nitrogen alone and its effects on the ocean need to be examined. Furthermore, for fertilization to enhance carbon sequestration, it must result in an increased carbon export flux to the deep ocean, a phenomenon that necessitates in-situ verification.
The field trials can start with offshore mesocosm experiments. Mesocosms are container-based systems and using those offshore provides a representative open ocean environment. These mesocosm experiments offer a means to quantify the influence of the fertilizer additions on species composition, nutrient and carbon removal, nitrogen fixation and organic matter production (Lampitt et al., 2008).
Subsequently, larger scale 'real' field experiments need be performed, to again monitor ecological and biochemical responses, but also to quantify the export flux. These can start by doing field experiments in the core of an eddy. Eddies tend to isolate their interior waters from the surrounding waters and are subject to high vertical coherence, providing ideal test conditions. Monitoring needs to be sufficiently long and sediment traps, autonomous ocean vehicles and underwater video profilers can be used to measure the export flux and biomass changes (National Academies of Sciences & Medicine, 2022; Smetacek & Naqvi, 2008; Yoon et al., 2018). Furthermore, monitoring can be done using satellite observations.

References

Ammerman, J. W., Hood, R. R., Case, D. A., & Cotner, J. B. (2003). Phosphorus deficiency in the atlantic: An emerging paradigm in oceanography. *Eos, Transactions American Geophysical Union*, *84*(18), 165–170.

Baker, C. A., Martin, A. P., Yool, A., & Popova, E. (2022). Biological carbon pump sequestration efficiency in the north atlantic: A leaky or a long-term sink? *Global Biogeochemical Cycles*, *36*(6), e2021GB007286.

Benson, B. B., & Krause Jr, D. (1984). The concentration and isotopic fractionation of oxygen dissolved in freshwater and seawater in equilibrium with the atmosphere 1. *Limnology and oceanography*, *29*(3), 620–632.

Blackwell, M., Darch, T., & Haslam, R. (2019). Phosphorus use efficiency and fertilizers: Future opportunities for improvements. *Frontiers of Agricultural Science and Engineering-FASE*, *6*(4), 332–340.

Boettcher, M., Chai, F., Cullen, J., Goeschl, T., Lampitt, R., Lenton, A., Oschlies, A., Rau, G., Rickaby, R., Ricke, K., et al. (2019). High level review of a wide range of proposed marine geoengineering techniques.

Boyd, P. W., Claustre, H., Levy, M., Siegel, D. A., & Weber, T. (2019). Multi-faceted particle pumps drive carbon sequestration in the ocean. *Nature*, *568*(7752), 327–335.

Brewin, R. J., Sathyendranath, S., Platt, T., Bouman, H., Ciavatta, S., Dall'Olmo, G., Dingle, J., Groom, S., Jönsson, B., Kostadinov, T. S., et al. (2021). Sensing the ocean biological carbon pump from space: A review of capabilities, concepts, research gaps and future developments. *Earth-Science Reviews*, *217*, 103604.

Bristow, L. A., Mohr, W., Ahmerkamp, S., & Kuypers, M. M. (2017). Nutrients that limit growth in the ocean. *Current Biology*, *27*(11), R474–R478.

Brodsky, I. (2018). *H3: Uber's hexagonal hierarchical spatial index*. Retrieved July 18, 2023, from https://www.uber.com/en-NL/blog/h3/

Browning, T. J., Achterberg, E. P., Rapp, I., Engel, A., Bertrand, E. M., Tagliabue, A., & Moore, C. M. (2017). Nutrient co-limitation at the boundary of an oceanic gyre. *Nature*, *551*(7679), 242–246.

Browning, T. J., & Moore, C. M. (2023). Global analysis of ocean phytoplankton nutrient limitation reveals high prevalence of co-limitation. *Nature Communications*, *14*(1), 5014.

CarbonCredits.com. (2023). *Live carbon prices today*. Retrieved November 28, 2023, from https://carboncredits.com/carbon-prices-today/

Chávez-Fuentes, J., Capobianco, A., Barbušová, J., & Hutňan, M. (2017). Manure from our agricultural animals: A quantitative and qualitative analysis focused on biogas production. *Waste and Biomass Valorization*, *8*, 1749–1757.

Christina, L., & Passow, U. (2007). Factors influencing the sinking of poc and the efficiency of the biological carbon pump. *Deep Sea Research Part II: Topical Studies in Oceanography*, *54*(5-7), 639–658.

Chu, P. C., & Fan, C. (2019). Global ocean synoptic thermocline gradient, isothermal-layer depth, and other upper ocean parameters. *Scientific Data*, *6*(1), 119.

Climate Trade. (2023). *Everything you need to know about carbon credits.* Retrieved November 26, 2023, from https://climatetrade.com/everything-you-need-to-know-about-carbon-credits/

Crowther, T. W., Glick, H. B., Covey, K. R., Bettigole, C., Maynard, D. S., Thomas, S. M., Smith, J. R., Hintler, G., Duguid, M. C., Amatulli, G., et al. (2015). Mapping tree density at a global scale. *Nature*, *525*(7568), 201–205.

De Vries, T. (2022). The ocean carbon cycle. *Annual Review of Environment and Resources*, *47*, 317–341.

De Vries, T., Primeau, F., & Deutsch, C. (2012). The sequestration efficiency of the biological pump. *Geophysical Research Letters*, *39*(13).

Doelman, J. C., Stehfest, E., van Vuuren, D. P., Tabeau, A., Hof, A. F., Braakhekke, M. C., Gernaat, D. E., van den Berg, M., van Zeist, W.-J., Daioglou, V., et al. (2020). Afforestation for climate change mitigation: Potentials, risks and trade-offs. *Global Change Biology*, *26*(3), 1576–1591.

Evans, G. T., & Garçon, V. (1997). One-dimensional models of water column biogeochemistry. *JGOFS report*, *23*(97), 85.

Fiedler, P. C. (2010). Comparison of objective descriptions of the thermocline. *Limnology and Oceanography: Methods*, *8*(6), 313–325.

Freing, A., Wallace, D. W., & Bange, H. W. (2012). Global oceanic production of nitrous oxide. *Philosophical Transactions of the Royal Society B: Biological Sciences*, *367*(1593), 1245–1255.

Friedlingstein, P., Jones, M. W., O'Sullivan, M., Andrew, R. M., Bakker, D. C., Hauck, J., Le Quéré, C., Peters, G. P., Peters, W., Pongratz, J., et al. (2022). Global carbon budget 2021. *Earth System Science Data*, *14*(4), 1917–2005.

Galbraith, E. D., Gnanadesikan, A., Dunne, J. P., & Hiscock, M. R. (2010). Regional impacts of iron-light colimitation in a global biogeochemical model. *Biogeosciences*, *7*(3), 1043–1064.

Garcia, H., Weathers, K., Paver, C., Smolyar, I., Boyer, T., Locarnini, M., Zweng, M., Mishonov, A., Baranova, O., Seidov, D., et al. (2019a). World ocean atlas 2018, volume 3: Dissolved oxygen, apparent oxygen utilization, and dissolved oxygen saturation.

Garcia, H., Weathers, K., Paver, C., Smolyar, I., Boyer, T., Locarnini, M., Zweng, M., Mishonov, A., Baranova, O., Seidov, D., et al. (2019b). World ocean atlas 2018. vol. 4: Dissolved inorganic nutrients (phosphate, nitrate and nitrate+ nitrite, silicate).

GEBCO Compilation Group. (2023). GEBCO 2023 Grid. https://doi.org/doi:10.5285/f98b053b-0cbc-6c23-e053-6c86abc0af7b

Glibert, P. M., Azanza, R., Burford, M., Furuya, K., Abal, E., Al-Azri, A., Al-Yamani, F., Andersen, P., Anderson, D. M., Beardall, J., et al. (2008). Ocean urea fertilization for carbon credits poses high ecological risks. *Marine Pollution Bulletin*, *56*(6), 1049–1056.

Goreau, T. (2023). *A letter from 200+ world scientists on advancing responsible research and development of ocean-based carbon dioxide removal*. Retrieved September 12, 2023, from https://www.globalcoral.org/a-letter-from-200-world-scientists-on-advancing-responsible-research-and-development-of-ocean-based-carbon-dioxide-removal/

Grönroos, J., Mattila, P., Regina, K., Nousiainen, J., Perälä, P., Saarinen, K., & Mikkola-Pusa, J. (2009). Development of the ammonia emission inventory in finland. revised model for agriculture.

Gruber, N. (2008). The marine nitrogen cycle: Overview and challenges. *Nitrogen in the marine environment*, *2*, 1–50.

Gruber, N. (2019). Consistent patterns of nitrogen fixation identified in the ocean.

Gupta, M., Williams, R. G., Lauderdale, J. M., Jahn, O., Hill, C., Dutkiewicz, S., & Follows, M. J. (2022). A nutrient relay sustains subtropical ocean productivity. *Proceedings of the National Academy of Sciences*, *119*(41), e2206504119.

Harrison, D. P. (2017). Global negative emissions capacity of ocean macronutrient fertilization. *Environmental Research Letters*, *12*(3), 035001.

Heinze, C., Meyer, S., Goris, N., Anderson, L., Steinfeldt, R., Chang, N., Le Quere, C., & Bakker, D. C. (2015). The ocean carbon sink–impacts, vulnerabilities and challenges. *Earth System Dynamics*, *6*(1), 327–358.

Hoxha, A., Christensen, B., et al. (2019). The carbon footprint of fertiliser production: Regional reference values. *Proceedings-International Fertiliser Society*, (805), 1–20.

International Energy Agency. (2021). Electricity market report.

International Maritime Organization. (2015). Third imo greenhouse gas study 2014.

IPCC. (2022). Summary for policymakers. In P. Shukla, J. Skea, R. Slade, A. A. Khourdajie, R. van Diemen, D. McCollum, M. Pathak, S. Some, P. Vyas, R. Fradera, M. Belkacemi, A. Hasija, G. Lisboa, S. Luz, & J. Malley (Eds.), *Climate change 2022: Mitigation of climate change*. Cambridge University Press. https://doi.org/10.1017/9781009157926.001

Iversen, M. H. (2023). Carbon export in the ocean: A biologist's perspective. *Annual Review of Marine Science*, *15*, 357–381.

Jones, D. C., Ito, T., Takano, Y., & Hsu, W.-C. (2014). Spatial and seasonal variability of the air-sea equilibration timescale of carbon dioxide. *Global Biogeochemical Cycles*, *28*(11), 1163–1178.

Jurado, E., Dijkstra, H. A., & van der Woerd, H. J. (2012). Microstructure observations during the spring 2011 stratiphyt-ii cruise in the northeast atlantic. *Ocean Science*, *8*(6), 945–957.

Keller, D. P., Oschlies, A., & Eby, M. (2012). A new marine ecosystem model for the university of victoria earth system climate model. *Geoscientific Model Development*, *5*(5), 1195–1220.

Kiel Institute for the World Economy. (2023). *New eu project launched to evaluate mechanisms for using the ocean to remove atmospheric co2.* Retrieved September 12, 2023, from https://www.ifw-kiel.de/publications/news/new-eu-project-launched-to-evaluate-mechanisms-for-using-the-ocean-to-remove-atmospheric-co2/

Kilgore, G. (2023). *How many trees are planted each year? full list by country, type, year.* Retrieved November 2, 2023, from https://8billiontrees.com/trees/how-many-trees-are-planted-each-year/

Köninger, J., Lugato, E., Panagos, P., Kochupillai, M., Orgiazzi, A., & Briones, M. J. (2021). Manure management and soil biodiversity: Towards more sustainable food systems in the eu. *Agricultural Systems*, *194*, 103251.

Kriest, I., Khatiwala, S., & Oschlies, A. (2010). Towards an assessment of simple global marine biogeochemical models of different complexity. *Progress in Oceanography*, *86*(3-4), 337–360.

Kvale, K., Keller, D. P., Koeve, W., Meissner, K. J., Somes, C. J., Yao, W., & Oschlies, A. (2021). Explicit silicate cycling in the kiel marine biogeochemistry model version 3 (kmbm3) embedded in the uvic escm version 2.9. *Geoscientific Model Development*, *14*(12), 7255–7285.

Kwon, E. Y., Primeau, F., & Sarmiento, J. L. (2009). The impact of remineralization depth on the air–sea carbon balance. *Nature Geoscience*, *2*(9), 630–635.

Lampitt, R. S., Achterberg, E. P., Anderson, T. R., Hughes, J., Iglesias-Rodriguez, M., Kelly-Gerreyn, B. A., Lucas, M., Popova, E., Sanders, R., Shepherd, J., et al. (2008). Ocean fertilization: A potential means of geoengineering? *Philosophical Transactions of the Royal Society A: Mathematical, Physical and Engineering Sciences*, *366*(1882), 3919–3945.

Landolfi, A., Dietze, H., Koeve, W., & Oschlies, A. (2013). Overlooked runaway feedback in the marine nitrogen cycle: The vicious cycle. *Biogeosciences*, *10*(3), 1351–1363.

Landolfi, A., Somes, C. J., Koeve, W., Zamora, L. M., & Oschlies, A. (2017). Oceanic nitrogen cycling and n2o flux perturbations in the anthropocene. *Global Biogeochemical Cycles*, *31*(8), 1236–1255.

Laufkötter, C., John, J. G., Stock, C. A., & Dunne, J. P. (2017). Temperature and oxygen dependence of the remineralization of organic matter. *Global Biogeochemical Cycles*, *31*(7), 1038–1050.

Lawrence, M. W. (2014). Efficiency of carbon sequestration by added reactive nitrogen in ocean fertilisation. *International Journal of Global Warming*, *6*(1), 15–33.

Le Moigne, F. A. (2019). Pathways of organic carbon downward transport by the oceanic biological carbon pump. *Frontiers in Marine Science*, *6*, 634.

Lebling, K., Northrop, E., McCormick, C., & Bridgwater, L. (2022). Towards responsible and informed ocean-based carbon dioxide removal: Research and governance priorities.

Leenstra, F., Vellinga, T., Neijenhuis, F., de Buisonjé, F., & Gollenbeek, L. (2019). *Manure: A valuable resource* (tech. rep.). Wageningen UR Livestock Research.

Letscher, R. T., Primeau, F., & Moore, J. K. (2016). Nutrient budgets in the subtropical ocean gyres dominated by lateral transport. *Nature Geoscience*, *9*(11), 815–819.

Lévy, M., Bopp, L., Karleskind, P., Resplandy, L., Éthé, C., & Pinsard, F. (2013). Physical pathways for carbon transfers between the surface mixed layer and the ocean interior. *Global Biogeochemical Cycles*, *27*(4), 1001–1012.

Liang, L., Eberwein, J., Allsman, L., Grantz, D., & Jenerette, G. (2015). Regulation of co2 and n2o fluxes by coupled carbon and nitrogen availability. *Environmental Research Letters*, *10*(3), 034008.

Locarnini, M., Mishonov, A., Baranova, O., Boyer, T., Zweng, M., Garcia, H., Seidov, D., Weathers, K., Paver, C., Smolyar, I., et al. (2018). World ocean atlas 2018, volume 1: Temperature.

Lohmann, R., Jurado, E., Dijkstra, H. A., & Dachs, J. (2013). Vertical eddy diffusion as a key mechanism for removing perfluorooctanoic acid (pfoa) from the global surface oceans. *Environmental pollution*, *179*, 88–94.

Matear, R. J., & Elliott, B. (2004). Enhancement of oceanic uptake of anthropogenic co2 by macronutrient fertilization. *Journal of Geophysical Research: Oceans*, *109*(C4).

McConnaughey, B. H. (1984). Coastal waters habitatcoastal waters habitat. In *Beaches and coastal geology* (pp. 322–324). Springer US. https://doi.org/10.1007/0-387-30843-1_126

McCormack, C. G., Born, W., Irvine, P. J., Achterberg, E. P., Amano, T., Ardron, J., Foster, P. N., Gattuso, J.-P., Hawkins, S. J., Hendy, E., et al. (2016). Key impacts of climate engineering on biodiversity and ecosystems, with priorities for future research. *Journal of Integrative Environmental Sciences*, *13*(2-4), 103–128.

McKie, R. (2023). *Scientists warn of 'phosphogeddon' as critical fertiliser shortages loom.* Retrieved September 28, 2023, from https://www.theguardian.com/environment/2023/mar/12/scientists-warn-of-phosphogeddon-fertiliser-shortages-loom

Meyer-Ohlendorf, N. (2021). Carbon dioxide removal strategy for the eu.

Moore, C., Mills, M., Arrigo, K., Berman-Frank, I., Bopp, L., Boyd, P., Galbraith, E., Geider, R., Guieu, C., Jaccard, S., et al. (2013). Processes and patterns of oceanic nutrient limitation. *Nature geoscience*, *6*(9), 701–710.

Moseman, A., & Harvey, C. (2022). *How many new trees would we need to offset our carbon emissions?* Retrieved October 16, 2023, from https://climate.mit.edu/ask-mit/how-many-new-trees-would-we-need-offset-our-carbon-emissions

Mulder, C., & Hendriks, A. J. (2014). Half-saturation constants in functional responses. *Global Ecology and Conservation*, *2*, 161–169.

NASA Ocean Biology Processing Group. (2022). Aqua modis level 3 mapped chlorophyll data, version r2022.0. https://doi.org/10.5067/AQUA/MODIS/L3M/CHL/2022

National Academies of Sciences, E., & Medicine. (2019). *Negative emissions technologies and reliable sequestration: A research agenda.* The National Academies Press. https://doi.org/10.17226/25259

National Academies of Sciences, E., & Medicine. (2022). *A research strategy for ocean-based carbon dioxide removal and sequestration.* The National Academies Press. https://doi.org/10.17226/26278

National Oceanic and Atmospheric Administration. (2022). *Carbon dioxide now more than 50 % higher than pre-industrial levels.* Retrieved March 27, 2023, from https://www.noaa.gov/news-release/carbon-dioxide-now-more-than-50-higher-than-pre-industrial-levels

NOAA. (2022). *Geoengineering as a response to climate change the london convention and london protocol.* Retrieved October 28, 2023, from https://www.noaa.gov/geoengineering-as-response-to-climate-change-london-convention-and-london-protocol

NOAA National Centers for Environmental Information. (2021). *New climatologies added to world ocean atlas.* Retrieved July 17, 2023, from https://www.ncei.noaa.gov/news/new-climatologies-added-world-ocean-atlas

Nowicki, M., DeVries, T., & Siegel, D. A. (2022). Quantifying the carbon export and sequestration pathways of the ocean's biological carbon pump. *Global Biogeochemical Cycles*, *36*(3), e2021GB007083.

Ocean Motion NASA. (2023). *Wind driven surface currents: Equatorial currents background.* Retrieved November 7, 2023, from https://oceanmotion.org/html/background/equatorial-currents.htm

Okin, G. S., Baker, A. R., Tegen, I., Mahowald, N. M., Dentener, F. J., Duce, R. A., Galloway, J. N., Hunter, K., Kanakidou, M., Kubilay, N., et al. (2011). Impacts of atmospheric nutrient deposition on marine productivity: Roles of nitrogen, phosphorus, and iron. *Global Biogeochemical Cycles*, *25*(2).

Omand, M. M., D'Asaro, E. A., Lee, C. M., Perry, M. J., Briggs, N., Cetinić, I., & Mahadevan, A. (2015). Eddy-driven subduction exports particulate organic carbon from the spring bloom. *Science*, *348*(6231), 222–225.

Paytan, A., & McLaughlin, K. (2007). The oceanic phosphorus cycle. *Chemical reviews*, *107*(2), 563–576.

Peborgh, J. V. (2021). *Cdr deep dives: Forest-based solutions.* Retrieved November 2, 2023, from https://jvanpeborgh.medium.com/cdr-deep-dives-forest-based-solutions-511bec9018c2

Poulsen, C., McGarragh, G., Thomas, G., Stengel, M., Christensen, M., Povey, A., Proud, S., Carboni, E., Hollmann, R., & Grainger, D. (2022). Surface radiation budget, cci icdr product version 3.1 [Accessed on 13-06-2023].

Rapp, B. E. (2017). Chapter 9 - fluids. In B. E. Rapp (Ed.), *Microfluidics: Modelling, mechanics and mathematics* (pp. 243–263). Elsevier. https://doi.org/https://doi.org/10.1016/B978-1-4557-3141-1.50009-5

Redfield, A. C. (1958). The biological control of chemical factors in the environment. *American scientist*, *46*(3), 230A–221.

Romero, E., Tenorio-Fernandez, L., Portela, E., Montes-Aréchiga, J., & Sánchez-Velasco, L. (2022). Improving the thermocline calculation over the global ocean. *EGUsphere*.

Sathyendranath, S., Stuart, V., Nair, A., Oka, K., Nakane, T., Bouman, H., Forget, M.-H., Maass, H., & Platt, T. (2009). Carbon-to-chlorophyll ratio and growth rate of phytoplankton in the sea. *Marine Ecology Progress Series*, *383*, 73–84.

Schmittner, A., Oschlies, A., Giraud, X., Eby, M., & Simmons, H. L. (2005). A global model of the marine ecosystem for long-term simulations: Sensitivity to ocean mixing, buoyancy forcing, particle sinking, and dissolved organic matter cycling. *Global Biogeochemical Cycles*, *19*(3).

Schoffman, H., Lis, H., Shaked, Y., & Keren, N. (2016). Iron–nutrient interactions within phytoplankton. *Frontiers in plant science*, *7*, 1223.

Schulte-Uebbing, L., Beusen, A., Bouwman, A., & De Vries, W. (2022). From planetary to regional boundaries for agricultural nitrogen pollution. *Nature*, *610*(7932), 507–512.

Secretariat of the Convention on Biological Diversity. (2009). *Scientific synthesis of the impacts of ocean fertilization on marine biodiversity*. desLibris.

Siegel, D. A., De Vries, T., Doney, S., & Bell, T. (2021). Assessing the sequestration time scales of some ocean-based carbon dioxide reduction strategies. *Environmental Research Letters*, *16*(10), 104003.

Siegel, D. A., De Vries, T., Cetinić, I., & Bisson, K. M. (2023). Quantifying the ocean's biological pump and its carbon cycle impacts on global scales. *Annual Review of Marine Science*, *15*, 329–356.

Sigman, D. M., & Hain, M. P. (2012). The biological productivity of the ocean. *Nature Education Knowledge*, *3*(10), 21.

Smetacek, V., & Naqvi, S. (2008). The next generation of iron fertilization experiments in the southern ocean. *Philosophical Transactions of the Royal Society A: Mathematical, Physical and Engineering Sciences*, *366*(1882), 3947–3967.

Smith, E. L. (1936). Photosynthesis in relation to light and carbon dioxide. *Proceedings of the National Academy of Sciences*, *22*(8), 504–511.

Somes, C. J., Landolfi, A., Koeve, W., & Oschlies, A. (2016). Limited impact of atmospheric nitrogen deposition on marine productivity due to biogeochemical feedbacks in a global ocean model. *Geophysical Research Letters*, *43*(9), 4500–4509.

Statista. (2023). *Production of urea worldwide in 2021, by region*. Retrieved October 10, 2023, from https://www.statista.com/statistics/1287037/global-urea-production-by-region/#:~:text=The%20global%20production%20of%20urea,to%20produce%20complex%20NPK%20fertilizers.

Strandberg, G., & Lind, P. (2021). The importance of horizontal model resolution on simulated precipitation in europe–from global to regional models. *Weather and Climate Dynamics*, *2*(1), 181–204.

Surname, W. < I., Surname, I., & Surname, I. (2022). *Carbon credits volume will be 40x more, prices will be* 150/*Tonby*2035. Retrieved November 30, 2023, from https://carboncredits.com/carbon-credits-volume-increase-prices-rise-2035/

Sylvera. (2022). *Permanence in carbon credits: Why it matters, and how to evaluate it*. Retrieved October 28, 2023, from https://www.sylvera.com/blog/permanence-carbon-credits

Talley, L. (2012). Dynamics v: Rotation and wind stress (ekman layers) and other mixed layer topics.

The European Space Agency. (2012). *Surface current speed*. Retrieved October 16, 2023, from https://www.esa.int/ESA_Multimedia/Images/2012/05/Surface_current_speed

Tivig, M., Keller, D. P., & Oschlies, A. (2021). Riverine nitrogen supply to the global ocean and its limited impact on global marine primary production: A feedback study using an earth system model. *Biogeosciences*, *18*(19), 5327–5350.

Tyrrell, T. (1999). The relative influences of nitrogen and phosphorus on oceanic primary production. *Nature*, *400*(6744), 525–531.

University of Minnesota Extension. (2021). *Fertilizer urea*. Retrieved October 10, 2023, from https://extension.umn.edu/nitrogen/fertilizer-urea

U.S. Environmental Protection Agency. (2023). *U.s. environmental protection agency*. Retrieved July 6, 2023, from https://www.epa.gov/national-aquatic-resource-surveys/indicators-zooplankton

Van de Waal, D. B., John, U., Ziveri, P., Reichart, G.-J., Hoins, M., Sluijs, A., & Rost, B. (2013). Ocean acidification reduces growth and calcification in a marine dinoflagellate. *Plos one*, *8*(6).

Wang, H., Aguirre-Villegas, H. A., Larson, R. A., & Alkan-Ozkaynak, A. (2019). Physical properties of dairy manure pre-and post-anaerobic digestion. *Applied Sciences*, *9*(13), 2703.

Wanninkhof, R. (1992). Relationship between wind speed and gas exchange over the ocean. *Journal of Geophysical Research: Oceans*, *97*(C5), 7373–7382.

Waterhouse, A. F., MacKinnon, J. A., Nash, J. D., Alford, M. H., Kunze, E., Simmons, H. L., Polzin, K. L., St. Laurent, L. C., Sun, O. M., Pinkel, R., et al. (2014). Global patterns of diapycnal mixing from measurements of the turbulent dissipation rate. *Journal of Physical Oceanography*, *44*(7), 1854–1872.

Weaver, A. J., Eby, M., Wiebe, E. C., Bitz, C. M., Duffy, P. B., Ewen, T. L., Fanning, A. F., Holland, M. M., MacFadyen, A., Matthews, H. D., et al. (2001). The uvic earth system climate model: Model description, climatology, and applications to past, present and future climates. *Atmosphere-Ocean*, *39*(4), 361–428.

Webb, P. (2022). *Introduction to oceanography*. Libretexts.

Williamson, P., Boyd, P. W., Harrison, D. P., Reynard, N., & Mashayek, A. (2022). Feasibility of using biologically-based processes in the open ocean and coastal seas for atmospheric co2 removal. In *Greenhouse gas removal technologies* (pp. 291–350). Royal Society of Chemistry.

World Ocean Atlas. (2018). *Data access: Statistical mean of mixed layer depth on 1° grid for all decades*. Retrieved June 2, 2023, from https://www.ncei.noaa.gov/access/world-ocean-atlas-2018/bin/woa18.pl?parameter=M

Yang, S., & Gruber, N. (2016). The anthropogenic perturbation of the marine nitrogen cycle by atmospheric deposition: Nitrogen cycle feedbacks and the 15n haber-bosch effect. *Global Biogeochemical Cycles*, *30*(10), 1418–1440.

Yao, W., Kvale, K. F., Achterberg, E., Koeve, W., & Oschlies, A. (2019). Hierarchy of calibrated global models reveals improved distributions and fluxes of biogeochemical tracers in models with explicit representation of iron. *Environmental Research Letters*, *14*(11), 114009.

Yoon, J.-E., Yoo, K.-C., Macdonald, A. M., Yoon, H.-I., Park, K.-T., Yang, E. J., Kim, H.-C., Lee, J. I., Lee, M. K., Jung, J., et al. (2018). Reviews and syntheses: Ocean iron fertilization experiments–past, present, and future looking to a future korean iron fertilization experiment in the southern ocean (kifes) project. *Biogeosciences*, *15*(19), 5847–5889.

Zehr, J. P., & Ward, B. B. (2002). Nitrogen cycling in the ocean: New perspectives on processes and paradigms. *Applied and environmental microbiology*, *68*(3), 1015–1024.

Zijlema, M. (2021). Computational modelling of flow and transport.

Zweng, M., Seidov, D., Boyer, T., Locarnini, M., Garcia, H., Mishonov, A., Baranova, O., Weathers, K., Paver, C., Smolyar, I., et al. (2019). World ocean atlas 2018, volume 2: Salinity.

A | Light limiting growth of phytoplankton

The phytoplankton growth rate as a function of sunlight is described by the curve of Smith (1936):

$$J_I = \frac{J^{max}\alpha I}{[(J^{max})^2 + (\alpha I)^2]^{1/2}} \tag{A.1}$$

where J^{max} is the maximum potential growth rate, α is the initial slope of the photosynthesis versus irradiance (P-I) curve and I is the downward shortwave radiation in the spectral domain relevant for photosynthesis (400-700 nm). Equation A.1 implies that the light limited growth rate (J_I) is J^{max} as $I \to \infty$ and αI is the growth rate as $I \to 0$.

To determine the irradiance at depth z, light attenuation needs to be taken into account. The following formulation is used:

$$I(z) = I_{z=0}PARe^{-k_w\tilde{z}-k_c\int_0^{\tilde{z}}(P_O+P_D)}) \tag{A.2}$$

here $I_{z=0}$ denotes the downward shortwave radiation at the sea surface, PAR stands for photosynthetically active radiation, and k_w and k_c are light attenuation coefficients by water and biomass, respectively. The light attenuation through sea ice is not considered in the developed model, since oceanic regions where sea ice occurs are filtered out of model computations. $\tilde{z}$ is the effective vertical coordinate, which is determined according to Snell's law relating the angle of incidence in air θ to the angle of incidence in water θ_0. This gives: $\tilde{z} = \frac{z}{cos(\theta_0)} = \frac{z}{\sqrt{1-sin^2(\theta)/1.33^2}}$. The angle of incidence $\theta = \phi - \delta$ is a function of latitude and declination. The declination is dependent on the fraction of the year f and the Earth's obliquity ε, for which 23° is used:

$$\delta = \varepsilon\frac{\pi}{180°}sin[(f - 0.22)2\pi] \tag{A.3}$$

At the equinoxes on 21 March ($f=0.22$) and 21 September, $\theta = \phi$, and at summer (winter) solstice the angle of incidence is at its minimum (maximum) $\phi \pm \delta$ (Schmittner et al., 2005).

When studying phytoplankton productivity on seasonal to annual timescales, the day-night cycle of the irradiance is a nuisance and is therefore preferably averaged over if possible (Evans & Garçon, 1997). Equation A.1 is therefore combined with a triangular shaped diurnal cycle, with fractional day length D and total light L during the day, to get the average light-limited growth in a grid layer during the day:

$$\begin{aligned}J_I^{ave} &= \frac{1}{\Delta Z * 24h}\int_{z-\Delta z/2}^{z+\Delta z/2}\int_{0h}^{24h}J_I dzdt \\ &= \frac{G_D}{(k_w + k_c(P_O + P_D))\Delta Z}\left[\Phi\left(\frac{2G_I}{G_D}\right) - \Phi\left(\frac{2G_I}{G_D}e^{-(k_w+k_c(P_O+P_D))\Delta Z}\right)\right]\end{aligned} \tag{A.4}$$

If light is so high that photosynthesis is saturated when there is any daylight, then the daily growth rate is $G_D = J^{max}D$. If light is so low that photosynthesis is in the linear range, growth in a day is $G_I = \alpha L_{z-\Delta z/2}$, where the total light L is evaluated at the top of the layer $z - \Delta z/2$. The function $\Phi(u) = ln\left(u + \sqrt{1 + u^2}\right) - \frac{\sqrt{1+u^2}-1}{u}$ (Evans & Garçon, 1997).

B | Marine biochemical model parameters

The parameters of the marine ecosystem model.

Parameter	Symbol	Value	Unit
Phytoplankton (P_O, P_D)			
Maximum growth rate at 0 °C	a	0.6	d^{-1}
Half-sat constant for NO_3 uptake	k_N	0.7	mmol N m^{-3}
Half-sat constant for PO_4 uptake	k_P	0.04375	mmol P m^{-3}
Ordinary phytoplankton mortality rate	m_{P_O}	0.03	d^{-1}
Diazotroph mortality rate	m_{P_D}	0.0012	d^{-1}
Fast recycling term	$\mu_{P,0}^*$	0.0012	d^{-1}
Diazotroph's handicap	c_D	0.4	Dimensionless
Half-sat constant for P_O Fe limitation	$k_{Fe}^{P_O}$	0.05	nmol Fe m^{-3}
Half-sat constant for P_D Fe limitation	$k_{Fe}^{P_D}$	0.406	nmol Fe m^{-3}
Zooplankton (Z)			
Maximum grazing rate at 0 °C	μ_Z^θ	0.668	d^{-1}
Maximum growth rate parameters	b	1.066	Dimensionless
	c	1.0	(°C)$^{-1}$
Growth efficiency coefficient	ω	0.4	Dimensionless
Assimilation efficiency coefficient	γ	0.7	Dimensionless
Mortality rate	m_Z	0.06	d^{-1}
Preference for grazing on P_O	ψ_{P_O}	0.3	Dimensionless
Preference for grazing on P_D	ψ_{P_D}	0.1	Dimensionless
Preference for grazing on $Detr$	ψ_{Detr}	0.3	Dimensionless
Preference for self-predation	ψ_Z	0.3	Dimensionless
Half-sat constant for grazing	k_{graze}	0.15	mmol N m^{-3}
Particulate detritus ($Detr$)			
Remineralization rate at 0 °C	μ_{D0}	0.055	d^{-1}
Sinking speed of $Detr$ at surface	$w_{D,0}$	14	m d^{-1}
Depth dependent sinking speed slope	m_w	0.062	d^{-1}
Mole ratios			
Mole C:P ratio of organic matter	$R_{C:P}$	106	Dimensionless
Mole C:N ratio of organic matter	$R_{C:N}$	6.625	Dimensionless
Mole N:P ratio of organic matter	$R_{N:P}$	16	Dimensionless
Mole O:N ratio	$R_{O:N}$	9.54	Dimensionless
Mole O:P ratios of organic matter	$R_{O:P}$	152.64	Dimensionless
Other coefficients			
E-folding temperature C	T_b	15.65	°C
Initial slope of the P-I curve C	α	0.1	(W m^{-2})$^{-1}$ d^{-1}
Fraction of photosynthetically active radiation	PAR	0.43	Dimensionless
Light attenuation due to water	k_w	0.04	m^{-1}
Light attenuation through phytoplankton	k_c	0.047	m^{-1} (mmol N m^{-3})$^{-1}$

Table B.1: Marine biochemical model parameters

C | Location filtering

This Appendix shows the outcomes of the individual filtering processes discussed in section 2.5.

C.1. No nitrogen limitation
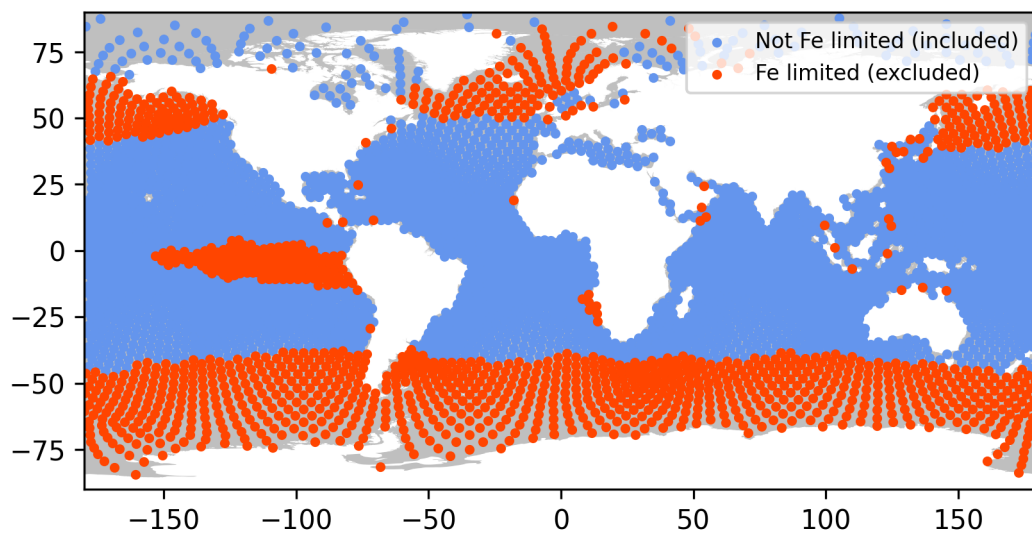
Figure C.1: Outcome of the filtering process excluding hexagons that are iron limited. Red hexagons are filtered out based on the criteria that their nitrate concentration at 10m depth is larger than 4 μM
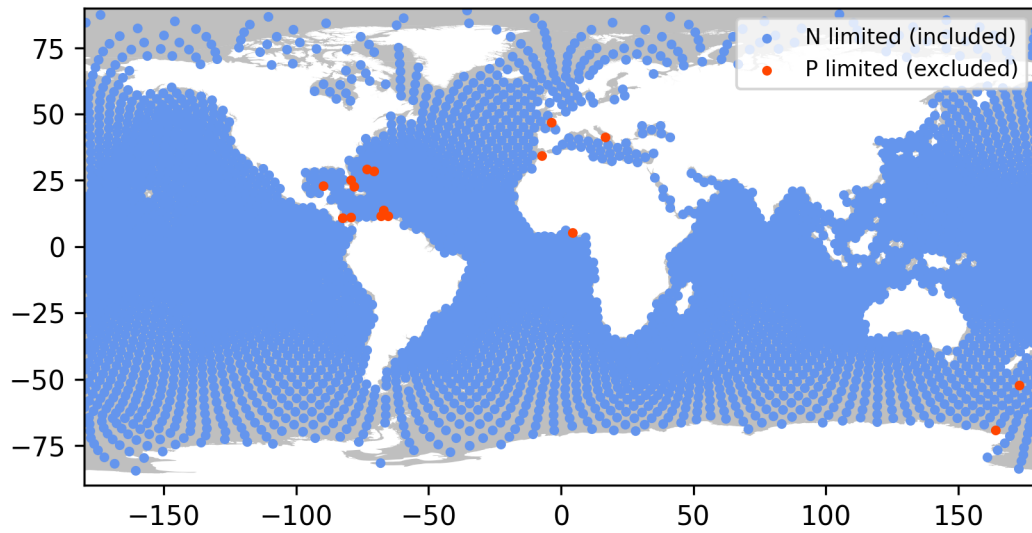
Figure C.2: Outcome of the filtering process excluding hexagons that are phosphate limited. Red hexagons are filtered out because they have a shortage of phosphate compared to nitrate in the upper 100m using the Redfield ratio.

C.2. Bathymetry
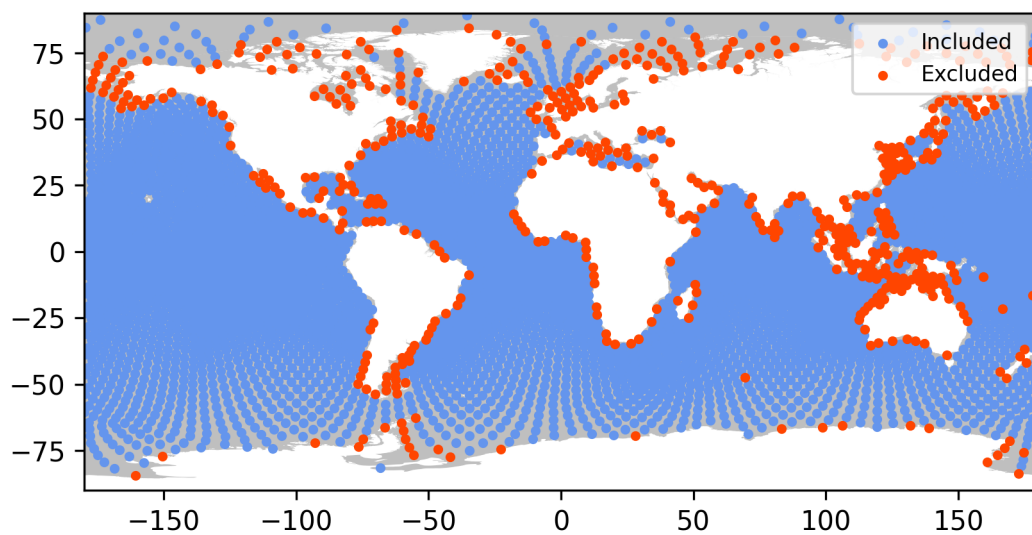
Figure C.3: Outcome of the bathymetry filtering step. Red hexagons are filtered out because their median bed level is above -500m and/or the 90th percentile of the bed level is larger than 0m

C.3. Horizontal surface transport
C.3.1. Phosphate
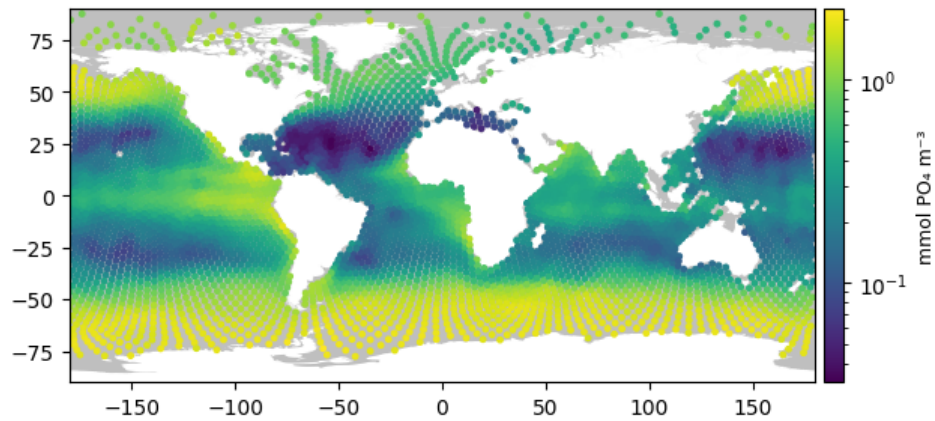
Figure C.4: The average annual phosphate concentrations in the upper 100m of ocean.
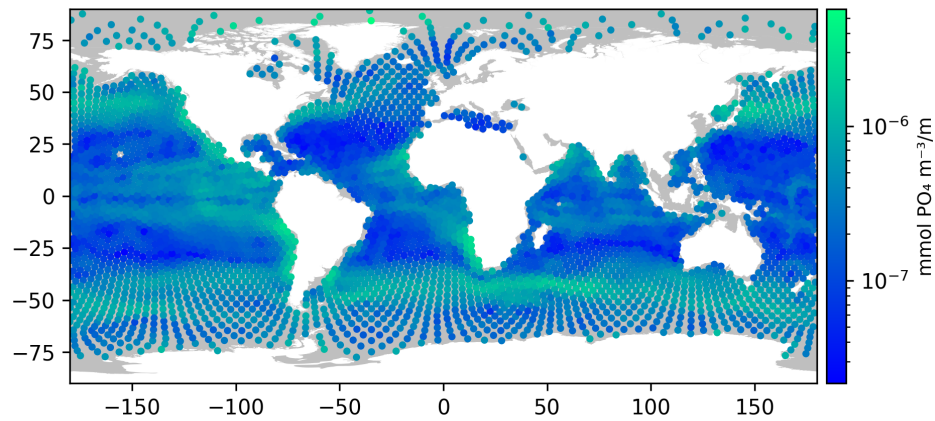
Figure C.5: The average annual horizontal phosphate gradients in the upper 100m.
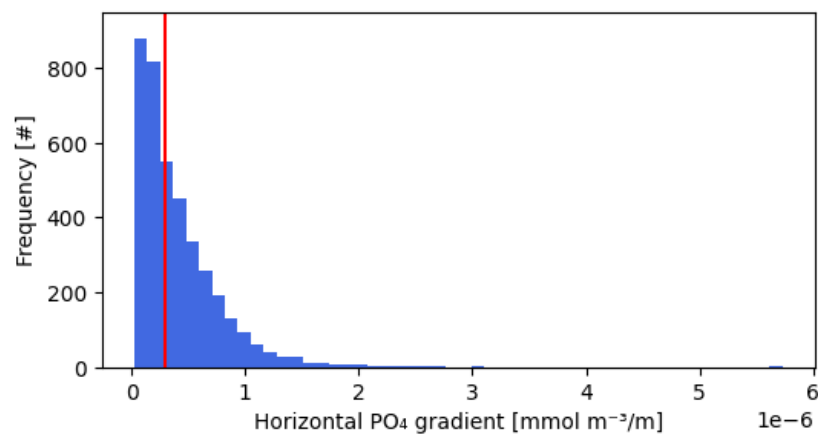
Figure C.6: Distribution of the average annual horizontal phosphate gradients in the upper 100m. The red line indicates the median of the gradients, which is at $2.988 \cdot 10^{-7} \ \frac{mmol \ m^{-3}}{m}$.

C.3.2. Nitrate
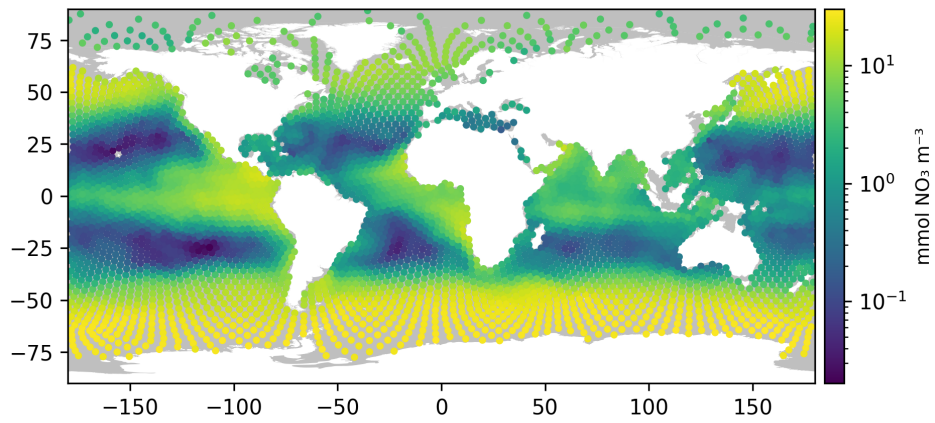
Figure C.7: The average annual nitrate concentrations in the upper 100m of ocean.
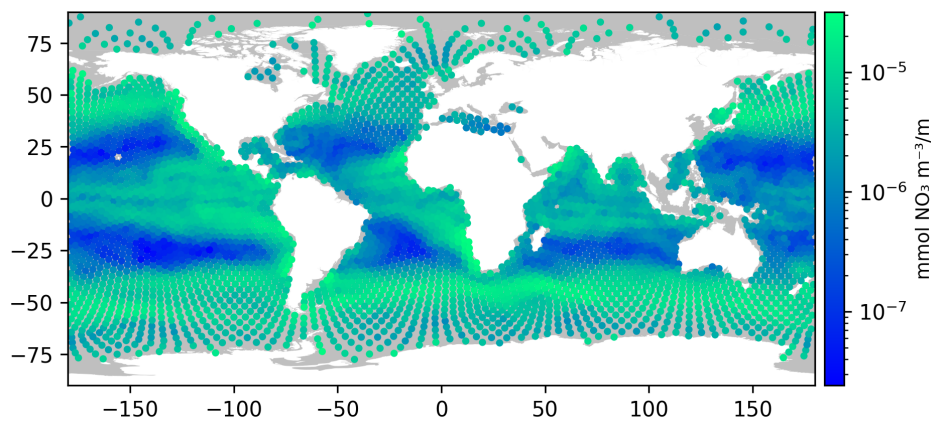
Figure C.8: The average annual horizontal nitrate gradients in the upper 100m.
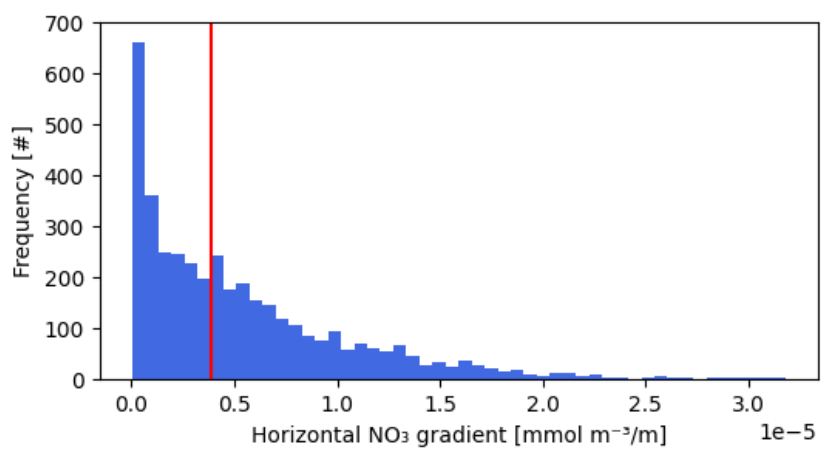
Figure C.9: Distribution of the average annual horizontal nitrate gradients in the upper 100m. The red line indicates the median of the gradients, which is at $3.906 \cdot 10^{-6} \ \frac{mmol \ m^{-3}}{m}$.
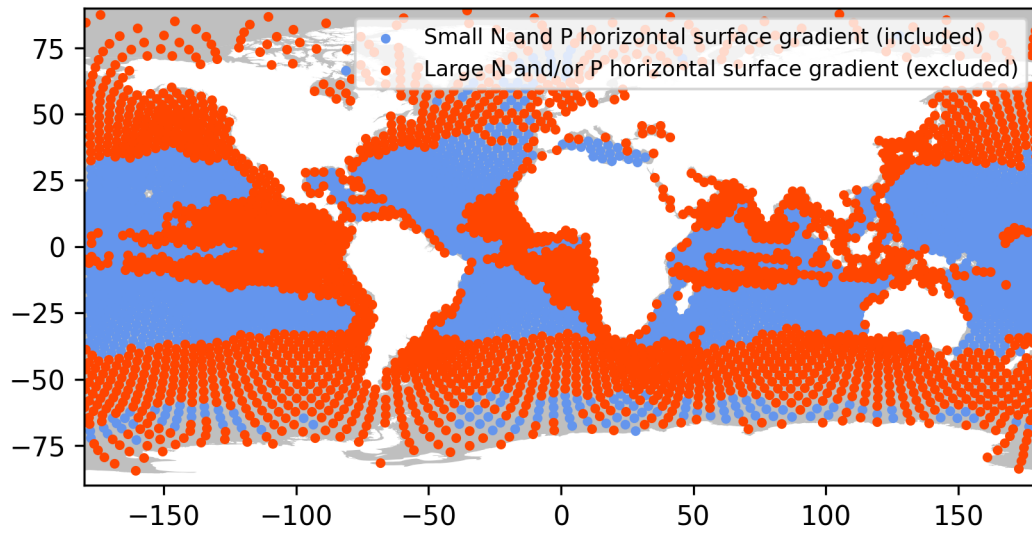
Figure C.10: Outcome of the filtering step excluding hexagons for which the supply of surface nutrients is expected to be predominantly horizontal. Red hexagons are filtered out because their annual average horizontal surface gradient in phosphate and/or nitrate is larger than the median $2.988 \cdot 10^{-7} \; \frac{mmol \, m^{-3}}{m}$ and $3.906 \cdot 10^{-6} \; \frac{mmol \, m^{-3}}{m}$, respectively.

D | Results baseline simulations

Simulation year	NPP [Gt C yr^{-1}]	N fixation [Tg N yr^{-1}]	Denitrification [Tg N yr^{-1}]
1	7.96	154.01	0.91
2	4.75	78.01	2.04
3	3.78	57.38	2.13
4	3.24	45.84	2.08
5	2.91	39.04	2.03
6	2.68	33.93	1.99
7	2.51	30.46	1.92
8	2.38	27.85	1.85
9	2.29	25.81	1.77
10	2.21	24.12	1.72

Table D.1: Yearly global outputs of baseline simulation with a thermocline diffusivity of 10^{-5} m^{2}s^{-1}

Simulation year	NPP [Gt C yr^{-1}]	N fixation [Tg N yr^{-1}]	Denitrification [Tg N yr^{-1}]
1	9.73	139.21	0.7
2	7.34	66.9	1.79
3	6.75	51.12	2.3
4	6.47	41.92	2.44
5	6.33	36.04	2.5
6	6.24	31.72	2.5
7	6.21	28.74	2.47
8	6.19	26.22	2.42
9	6.19	24.46	2.37
10	6.21	22.9	2.33

Table D.2: Yearly global outputs of baseline simulation with a thermocline diffusivity of $3*10^{-5}$ m^{2}s^{-1}

Simulation year	NPP [Gt C yr^{-1}]	N fixation [Tg N yr^{-1}]	Denitrification [Tg N yr^{-1}]
1	12.44	118.34	0.49
2	11.75	46.03	1.18
3	12.02	33.0	1.82
4	12.4	26.14	2.28
5	12.77	21.65	2.56
6	13.15	18.83	2.77
7	13.49	16.73	2.94
8	13.84	15.34	3.09
9	14.16	13.94	3.2
10	14.47	13.26	3.28

Table D.3: Yearly global outputs of baseline simulation with a thermocline diffusivity of $6*10^{-5}$ m^{2}s^{-1}

Simulation year	NPP [Gt C yr^{-1}]	N fixation [Tg N yr^{-1}]	Denitrification [Tg N yr^{-1}]
1	16.27	95.22	0.35
2	18.59	22.31	0.72
3	20.58	13.0	1.02
4	22.31	9.84	1.29
5	23.79	8.15	1.64
6	25.08	6.79	2.03
7	26.22	6.38	2.37
8	27.24	5.55	2.66
9	28.17	5.57	2.93
10	28.99	4.83	3.15

Table D.4: Yearly global outputs of baseline simulation with a thermocline diffusivity of 10^{-4} m^{2}s^{-1}
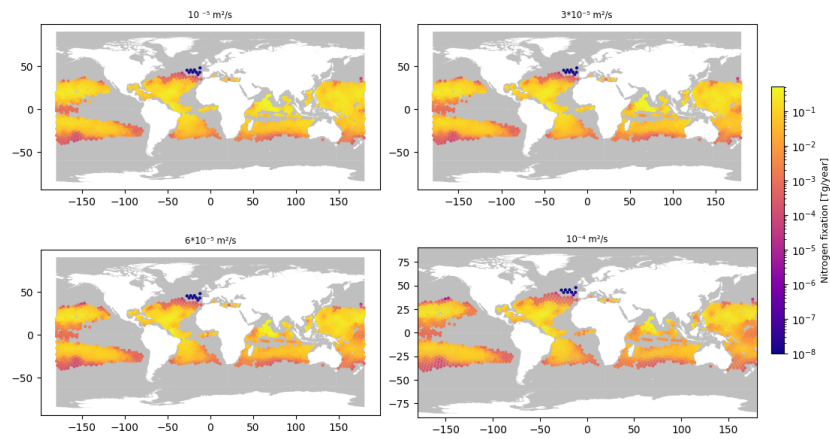
(a) Simulation year 1
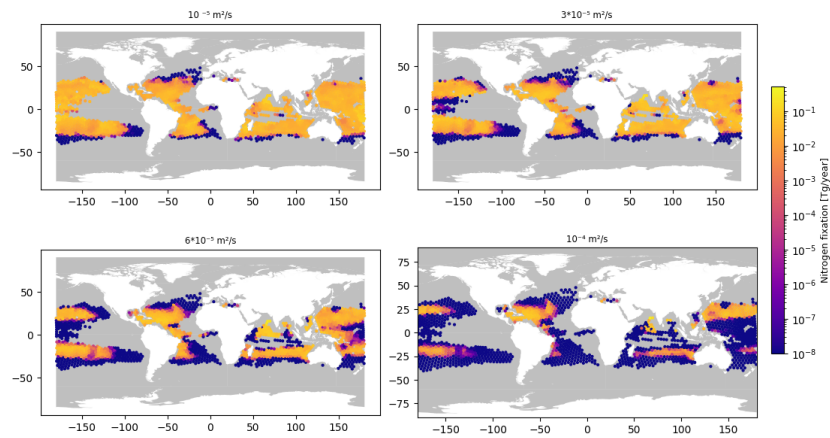
(b) Simulation year 5
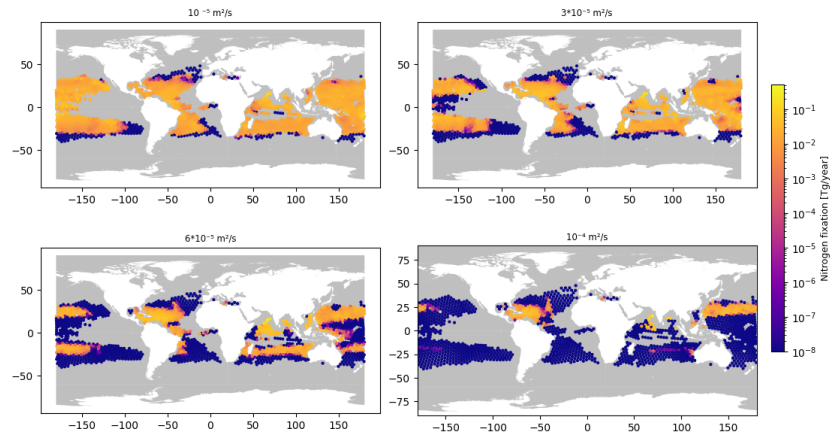
(c) Simulation year 10

Figure D.1: Amount of nitrogen fixation in the baseline simulations in simulation year 1, 5 and 10. The titles above the maps indicate the thermocline diffusivity of the simulation.

E | One-off nitrogen fertilization results on global scale

E.1. Overview

Dthermo [m^2/s]	Spin-up	N add moment	Long-term C sequestration [Gt]	Long-term C sequestration NH [Gt]	Long-term C sequestration SH [Gt]
10^{-5}	1 year	1 Jan	0.08	0.03	0.05
10^{-5}	1 year	1 Apr	0.11	0.02	0.09
10^{-5}	1 year	1 Jul	0.15	0.01	0.14
10^{-5}	1 year	1 Oct	0.1	0.01	0.08
10^{-5}	4 years	1 Jan	0.07	0.02	0.05
10^{-5}	4 years	1 Apr	0.1	0.01	0.08
10^{-5}	4 years	1 Jul	0.14	0.01	0.13
10^{-5}	4 years	1 Oct	0.09	0.01	0.08
$3 \cdot 10^{-5}$	1 year	1 Jan	0.11	0.05	0.06
$3 \cdot 10^{-5}$	1 year	1 Apr	0.13	0.04	0.1
$3 \cdot 10^{-5}$	1 year	1 Jul	0.17	0.02	0.15
$3 \cdot 10^{-5}$	1 year	1 Oct	0.12	0.03	0.09
$3 \cdot 10^{-5}$	4 years	1 Jan	0.11	0.05	0.06
$3 \cdot 10^{-5}$	4 years	1 Apr	0.13	0.04	0.1
$3 \cdot 10^{-5}$	4 years	1 Jul	0.17	0.03	0.14
$3 \cdot 10^{-5}$	4 years	1 Oct	0.12	0.03	0.09
$6 \cdot 10^{-5}$	1 year	1 Jan	0.13	0.06	0.07
$6 \cdot 10^{-5}$	1 year	1 Apr	0.15	0.05	0.1
$6 \cdot 10^{-5}$	1 year	1 Jul	0.18	0.03	0.15
$6 \cdot 10^{-5}$	1 year	1 Oct	0.14	0.04	0.09
$6 \cdot 10^{-5}$	4 years	1 Jan	0.13	0.06	0.07
$6 \cdot 10^{-5}$	4 years	1 Apr	0.15	0.05	0.1
$6 \cdot 10^{-5}$	4 years	1 Jul	0.18	0.04	0.14
$6 \cdot 10^{-5}$	4 years	1 Oct	0.14	0.05	0.09
10^{-4}	1 year	1 Jan	0.13	0.06	0.07
10^{-4}	1 year	1 Apr	0.15	0.05	0.1
10^{-4}	1 year	1 Jul	0.18	0.04	0.14
10^{-4}	1 year	1 Oct	0.14	0.05	0.09
10^{-4}	4 years	1 Jan	0.13	0.07	0.06
10^{-4}	4 years	1 Apr	0.14	0.05	0.09
10^{-4}	4 years	1 Jul	0.17	0.04	0.12
10^{-4}	4 years	1 Oct	0.13	0.05	0.08

Table E.1: Part 1: Overview of globally integrated results from the one-off nitrogen fertilization in all 32 fertilization simulations

Dthermo [m²/s]	Spin-up	N add mo-ment	N added [Gt]	N added NH [Gt]	N added SH [Gt]	C_{LT}/N ratio	ΔN fix/ N add [%]	ΔN fix [Gt]	#hexa with-out N lim
10^{-5}	1 year	1 Jan	0.13	0.06	0.08	0.59	55.25	0.07	128
10^{-5}	1 year	1 Apr	0.15	0.04	0.11	0.73	44.76	0.06	196
10^{-5}	1 year	1 Jul	0.19	0.03	0.17	0.78	37.26	0.07	198
10^{-5}	1 year	1 Oct	0.12	0.03	0.09	0.79	43.63	0.05	204
10^{-5}	4 years	1 Jan	0.08	0.03	0.05	0.83	42.49	0.03	299
10^{-5}	4 years	1 Apr	0.1	0.02	0.08	0.93	32.4	0.03	324
10^{-5}	4 years	1 Jul	0.14	0.01	0.13	0.96	25.06	0.04	323
10^{-5}	4 years	1 Oct	0.09	0.02	0.07	0.97	33.4	0.03	332
$3 \cdot 10^{-5}$	1 year	1 Jan	0.15	0.07	0.08	0.72	38.37	0.06	136
$3 \cdot 10^{-5}$	1 year	1 Apr	0.17	0.05	0.12	0.8	30.54	0.05	159
$3 \cdot 10^{-5}$	1 year	1 Jul	0.22	0.03	0.18	0.79	25.72	0.06	160
$3 \cdot 10^{-5}$	1 year	1 Oct	0.15	0.04	0.11	0.85	29.75	0.04	163
$3 \cdot 10^{-5}$	4 years	1 Jan	0.12	0.05	0.06	0.91	24.36	0.03	230
$3 \cdot 10^{-5}$	4 years	1 Apr	0.14	0.04	0.1	0.92	19.88	0.03	239
$3 \cdot 10^{-5}$	4 years	1 Jul	0.19	0.03	0.16	0.88	15.76	0.03	239
$3 \cdot 10^{-5}$	4 years	1 Oct	0.13	0.04	0.09	0.95	20.13	0.03	243
$6 \cdot 10^{-5}$	1 year	1 Jan	0.17	0.08	0.09	0.75	21.77	0.04	119
$6 \cdot 10^{-5}$	1 year	1 Apr	0.19	0.06	0.13	0.79	16.29	0.03	138
$6 \cdot 10^{-5}$	1 year	1 Jul	0.25	0.04	0.21	0.74	12.65	0.03	139
$6 \cdot 10^{-5}$	1 year	1 Oct	0.17	0.05	0.12	0.81	14.45	0.02	147
$6 \cdot 10^{-5}$	4 years	1 Jan	0.17	0.08	0.09	0.8	10.75	0.02	182
$6 \cdot 10^{-5}$	4 years	1 Apr	0.19	0.06	0.14	0.79	9.14	0.02	188
$6 \cdot 10^{-5}$	4 years	1 Jul	0.25	0.05	0.21	0.72	6.78	0.02	188
$6 \cdot 10^{-5}$	4 years	1 Oct	0.18	0.06	0.12	0.79	8.79	0.02	188
10^{-4}	1 year	1 Jan	0.19	0.09	0.1	0.68	9.54	0.02	107
10^{-4}	1 year	1 Apr	0.21	0.07	0.15	0.69	6.42	0.01	123
10^{-4}	1 year	1 Jul	0.28	0.06	0.22	0.63	4.48	0.01	124
10^{-4}	1 year	1 Oct	0.2	0.07	0.13	0.68	4.79	0.01	124
10^{-4}	4 years	1 Jan	0.21	0.1	0.1	0.63	3.57	0.01	159
10^{-4}	4 years	1 Apr	0.23	0.08	0.15	0.63	2.61	0.01	164
10^{-4}	4 years	1 Jul	0.3	0.07	0.23	0.57	2.27	0.01	163
10^{-4}	4 years	1 Oct	0.22	0.08	0.14	0.61	2.64	0.01	163

Table E.2: Part 2: Overview of globally integrated results from the one-off nitrogen fertilization in all 32 fertilization simulations. ΔN fix follows from: nitrogen fixation baseline simulation - nitrogen fixation fertilization simulation. The last column presents the amount of hexagons in a fertilization that at the moment of the nitrogen addition (start of simulation) experienced no nitrogen limitation in their mixed layer

E.2. Spatial patterns

E.2.1. Long-term carbon sequestration achieved 5 years after the fertilization

D_{thermo}: 10^{-5} m²/s, spin up: 1 year

D_{thermo}: 10^{-5} m²/s, spin up: 4 years

Figure E.1: Long-term carbon sequestration [g m^{-2}] from fertilization in simulations with a thermocline diffusivity of 10^{-5} m²s^{-1}. Top and bottom four figures are associated with 1 or 4 full years of baseline simulation spin-up, respectively. The titles above each figure represent the timing of the nitrogen addition, the integrated global long-term carbon sequestration from the fertilization, and the total amount of nitrogen added. The dark blue hexagons had no nitrogen limitation in their mixed layer at the moment of fertilization, so no nitrogen addition took place.

Figure E.2: Long-term carbon sequestration [g m^{-2}] from fertilization in simulations with a thermocline diffusivity of $3 \cdot 10^{-5}$ m^{2}s^{-1}. Top and bottom four figures are associated with 1 or 4 full years of baseline simulation spin-up, respectively. The titles above each figure represent the timing of the nitrogen addition, the integrated global long-term carbon sequestration from the fertilization, and the total amount of nitrogen added. The dark blue hexagons had no nitrogen limitation in their mixed layer at the moment of fertilization, so no nitrogen addition took place.
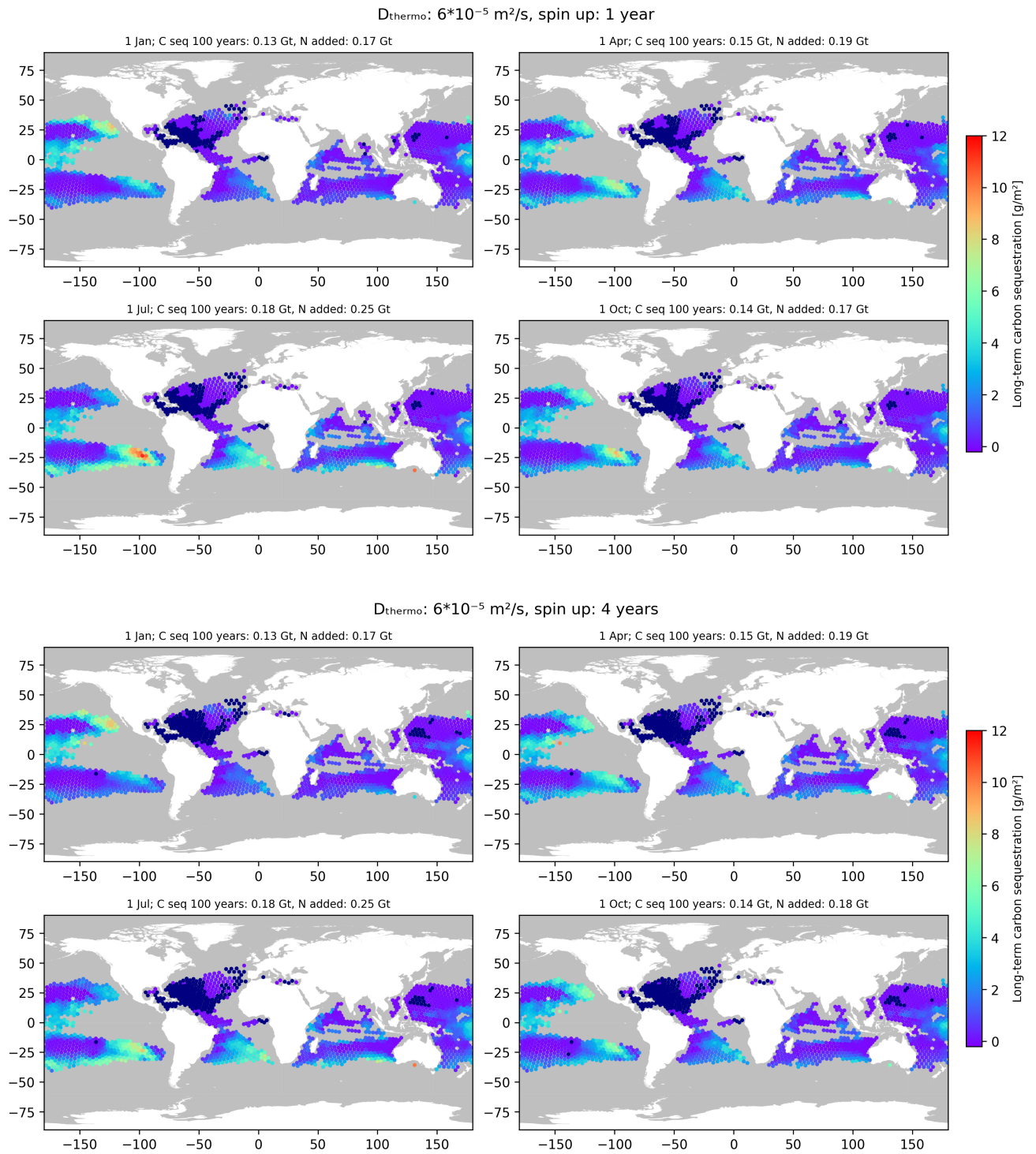
Figure E.3: Long-term carbon sequestration [g m^{-2}] from fertilization in simulations with a thermocline diffusivity of $6 \cdot 10^{-5}$ m^{2}s^{-1}. Top and bottom four figures are associated with 1 or 4 full years of baseline simulation spin-up, respectively. The titles above each figure represent the timing of the nitrogen addition, the integrated global long-term carbon sequestration from the fertilization, and the total amount of nitrogen added. The dark blue hexagons had no nitrogen limitation in their mixed layer at the moment of fertilization, so no nitrogen addition took place.
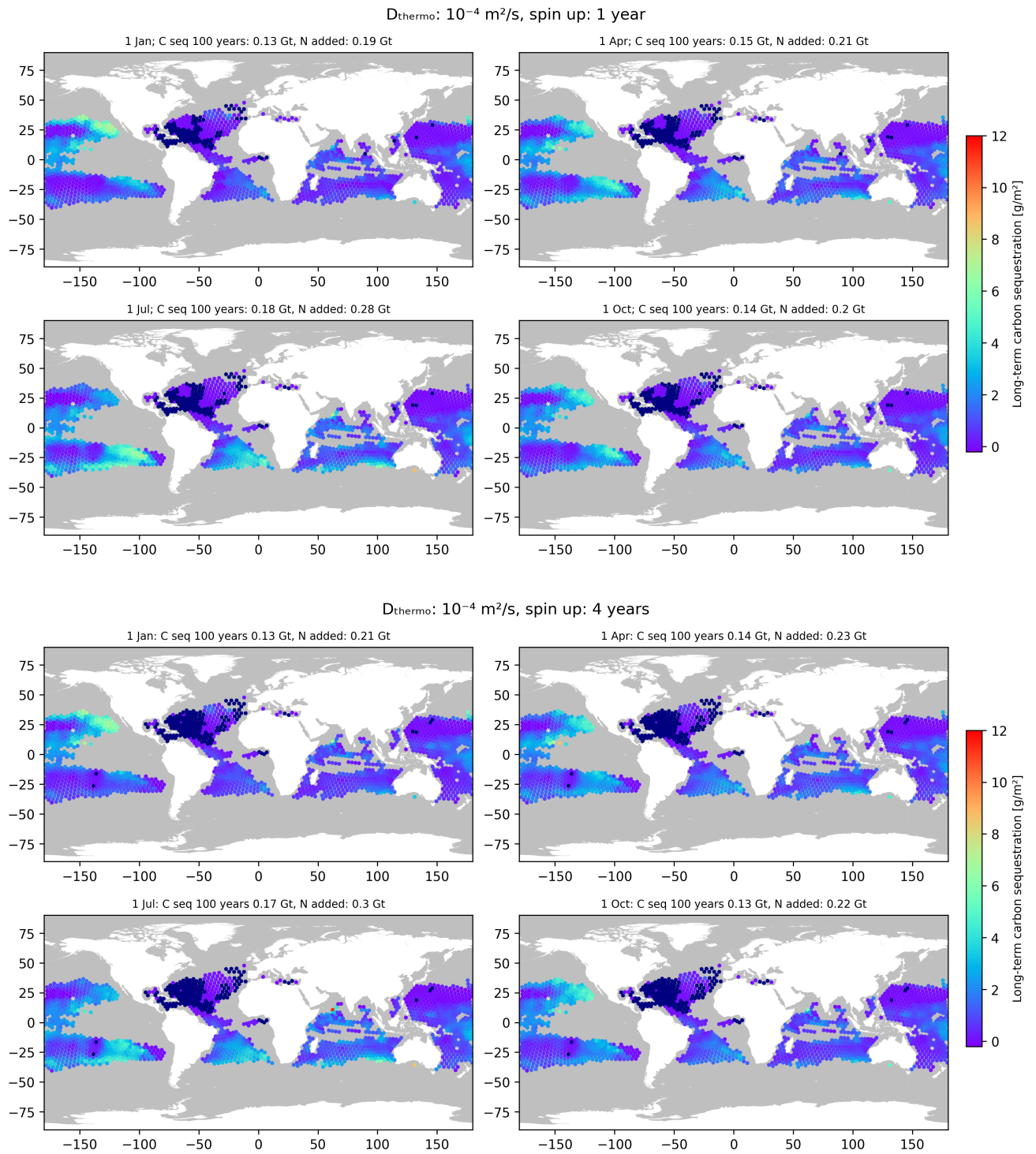
Figure E.4: Long-term carbon sequestration [g m^{-2}] from fertilization in simulations with a thermocline diffusivity of 10^{-4} m^{2}s^{-1}. Top and bottom four figures are associated with 1 or 4 full years of baseline simulation spin-up, respectively. The titles above each figure represent the timing of the nitrogen addition, the integrated global long-term carbon sequestration from the fertilization, and the total amount of nitrogen added. The dark blue hexagons had no nitrogen limitation in their mixed layer at the moment of fertilization, so no nitrogen addition took place.

E.2.2. Normalized offset from reduced nitrogen fixation

D_{thermo}: 10^{-5} m²/s, spin up: 1 year

D_{thermo}: 10^{-5} m²/s, spin up: 4 years
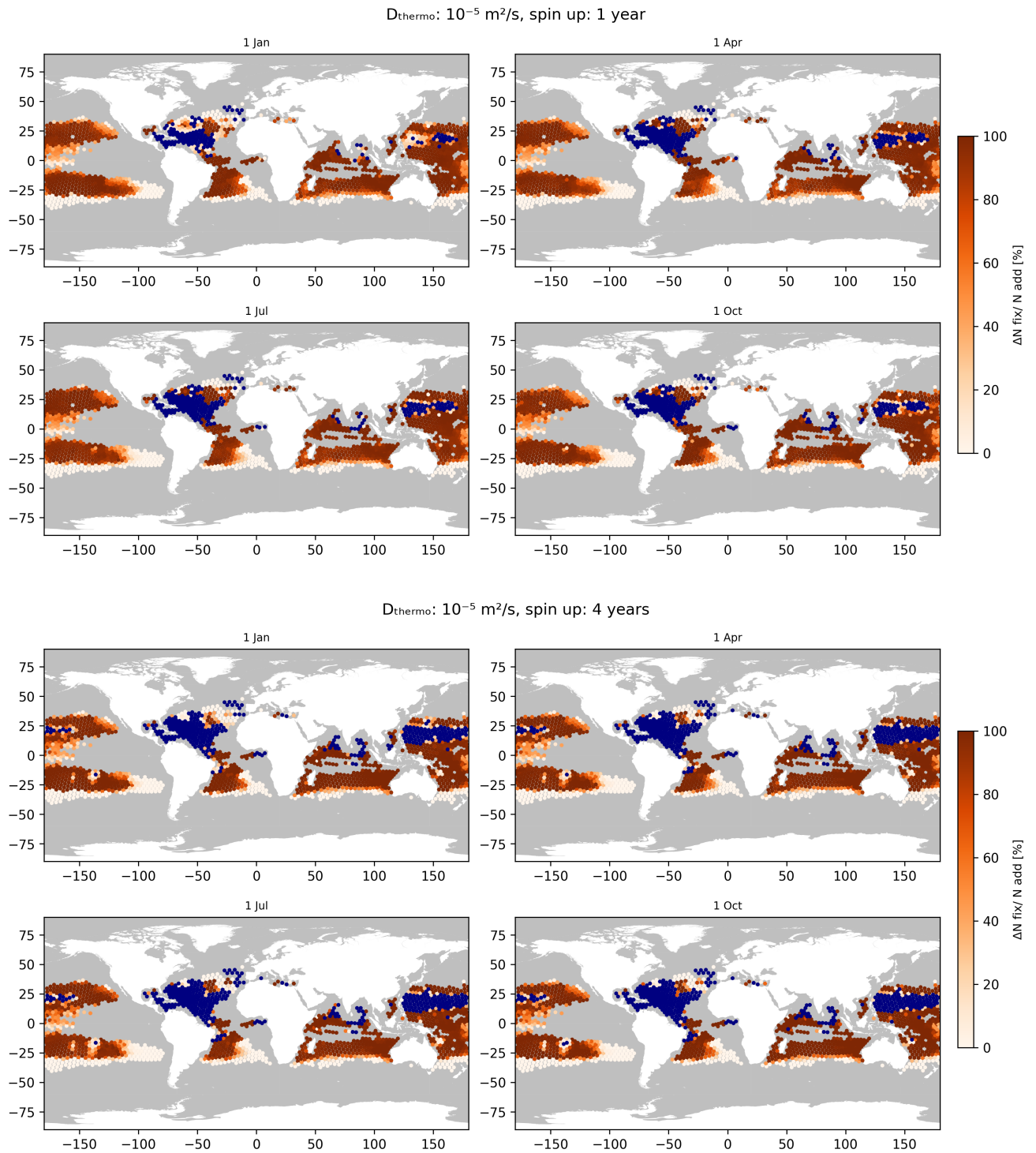
Figure E.5: Normalized offset [%] of the added nitrogen from reduced nitrogen fixation (calculated by $\frac{Nfix,BS - Nfix,FS}{Nadd} * 100\%$) in simulations with a thermocline diffusivity of 10^{-5} m²s⁻¹. Top and bottom four figures are associated with 1 or 4 full years of baseline simulation spin-up, respectively. The dark blue hexagons had no nitrogen limitation in their mixed layer at the moment of fertilization, so no nitrogen addition took place.
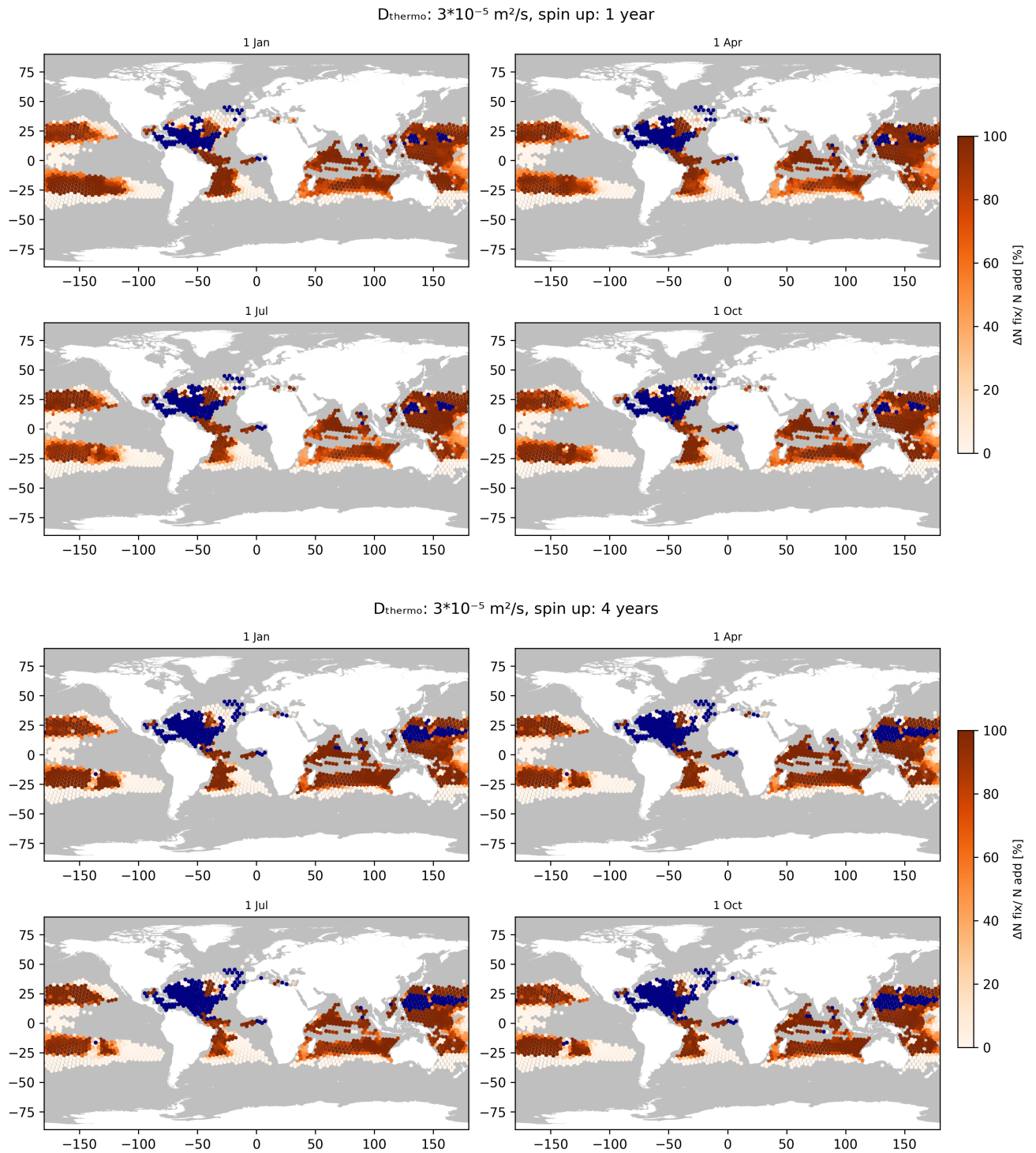
Figure E.6: Normalized offset [%] of the added nitrogen from reduced nitrogen fixation (calculated by $\frac{Nfix,BS-Nfix,FS}{Nadd} * 100\%$) in simulations with a thermocline diffusivity of $3 \cdot 10^{-5}$ m²s⁻¹. Top and bottom four figures are associated with 1 or 4 full years of baseline simulation spin-up, respectively. The dark blue hexagons had no nitrogen limitation in their mixed layer at the moment of fertilization, so no nitrogen addition took place.
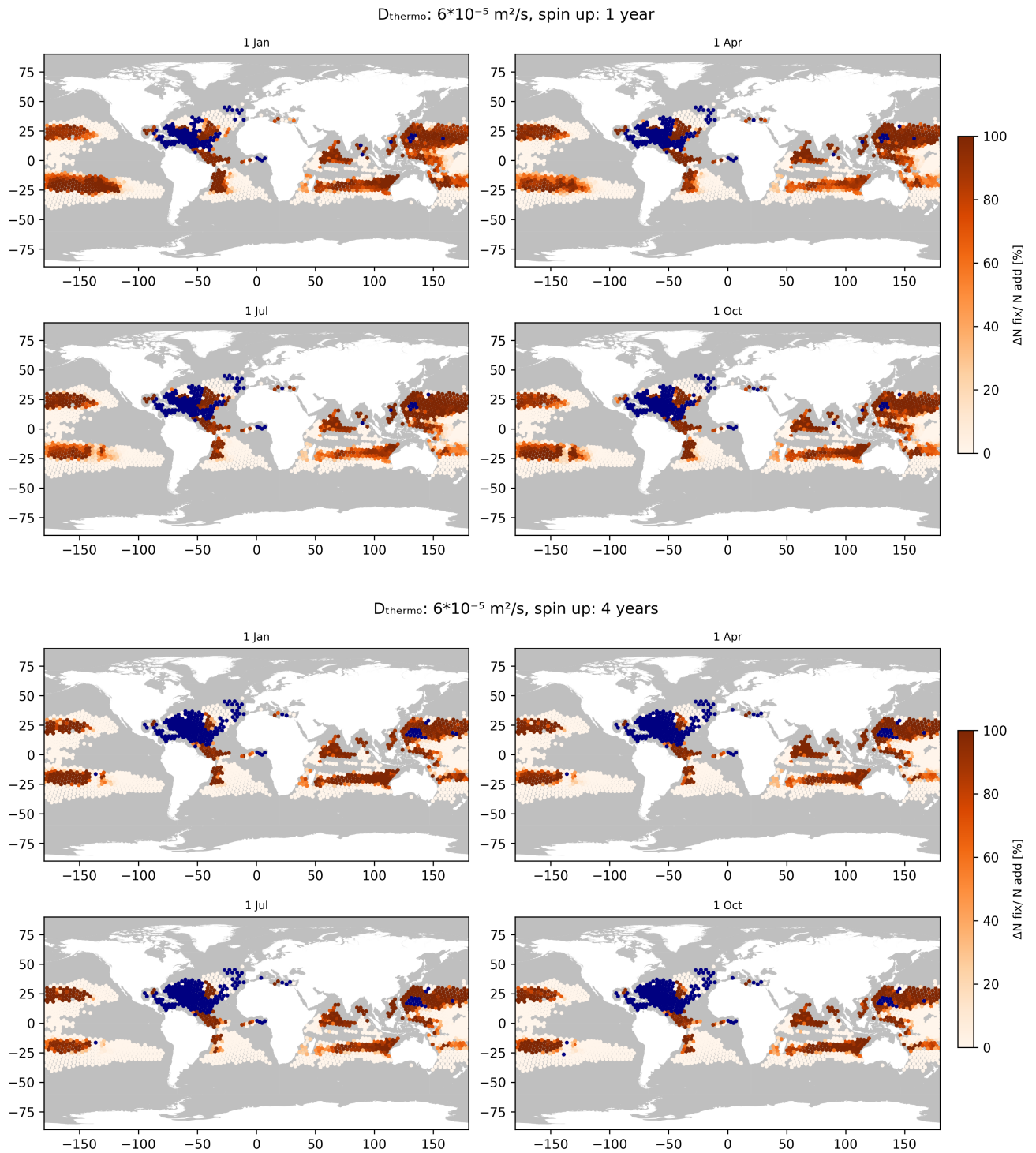
Figure E.7: Normalized offset [%] of the added nitrogen from reduced nitrogen fixation (calculated by $\frac{Nfix,BS-Nfix,FS}{Nadd} * 100\%$) in simulations with a thermocline diffusivity of $6 \cdot 10^{-5}$ m^{2}s^{-1}. Top and bottom four figures are associated with 1 or 4 full years of baseline simulation spin-up, respectively. The dark blue hexagons had no nitrogen limitation in their mixed layer at the moment of fertilization, so no nitrogen addition took place.
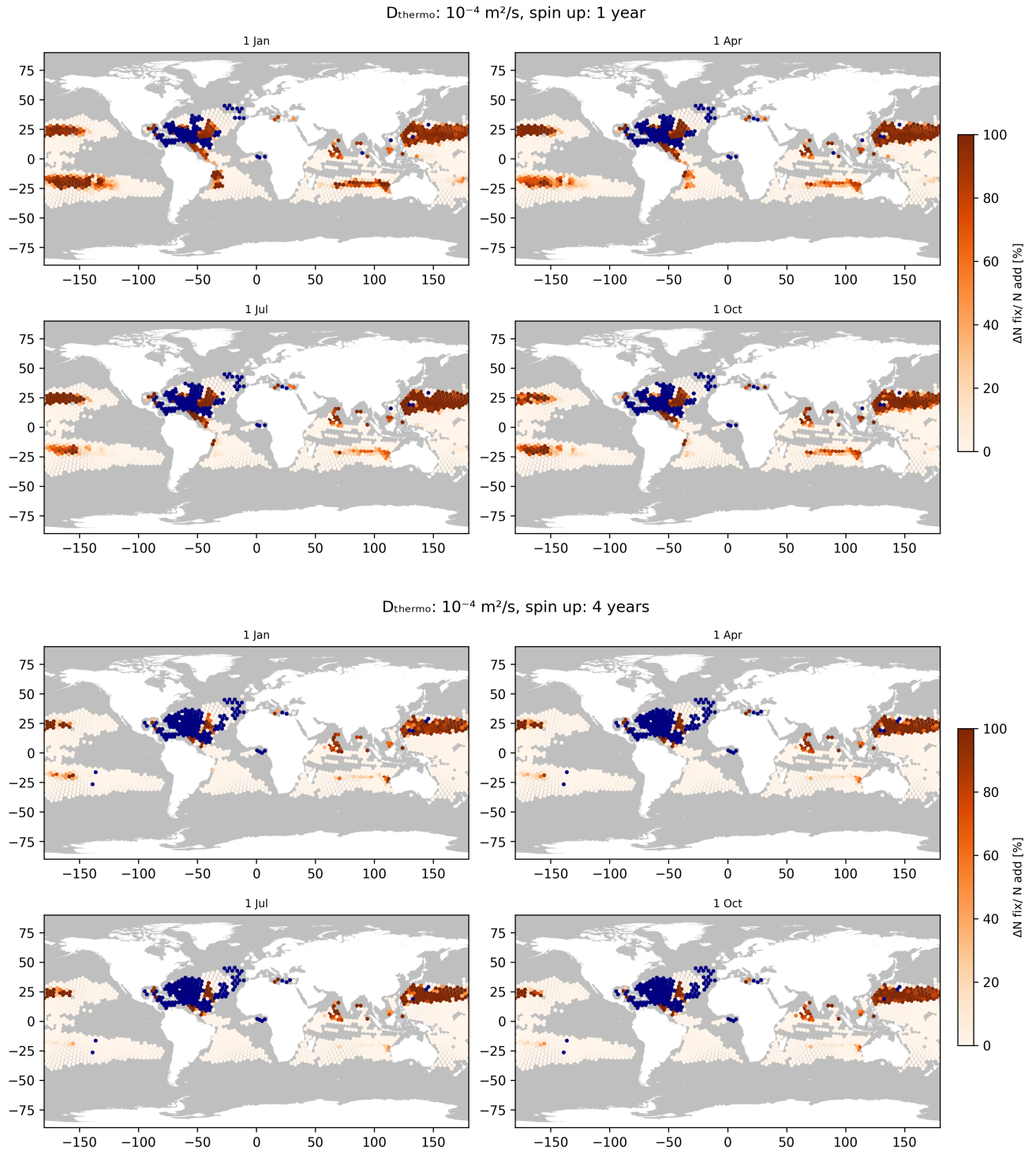
Figure E.8: Normalized offset [%] of the added nitrogen from reduced nitrogen fixation (calculated by $\frac{Nfix,BS - Nfix,FS}{Nadd} * 100\%$) in simulations with a thermocline diffusivity of 10^{-4} m^{2}s^{-1}. Top and bottom four figures are associated with 1 or 4 full years of baseline simulation spin-up, respectively. The dark blue hexagons had no nitrogen limitation in their mixed layer at the moment of fertilization, so no nitrogen addition took place.

E.2.3. C_{LT}/N ratio
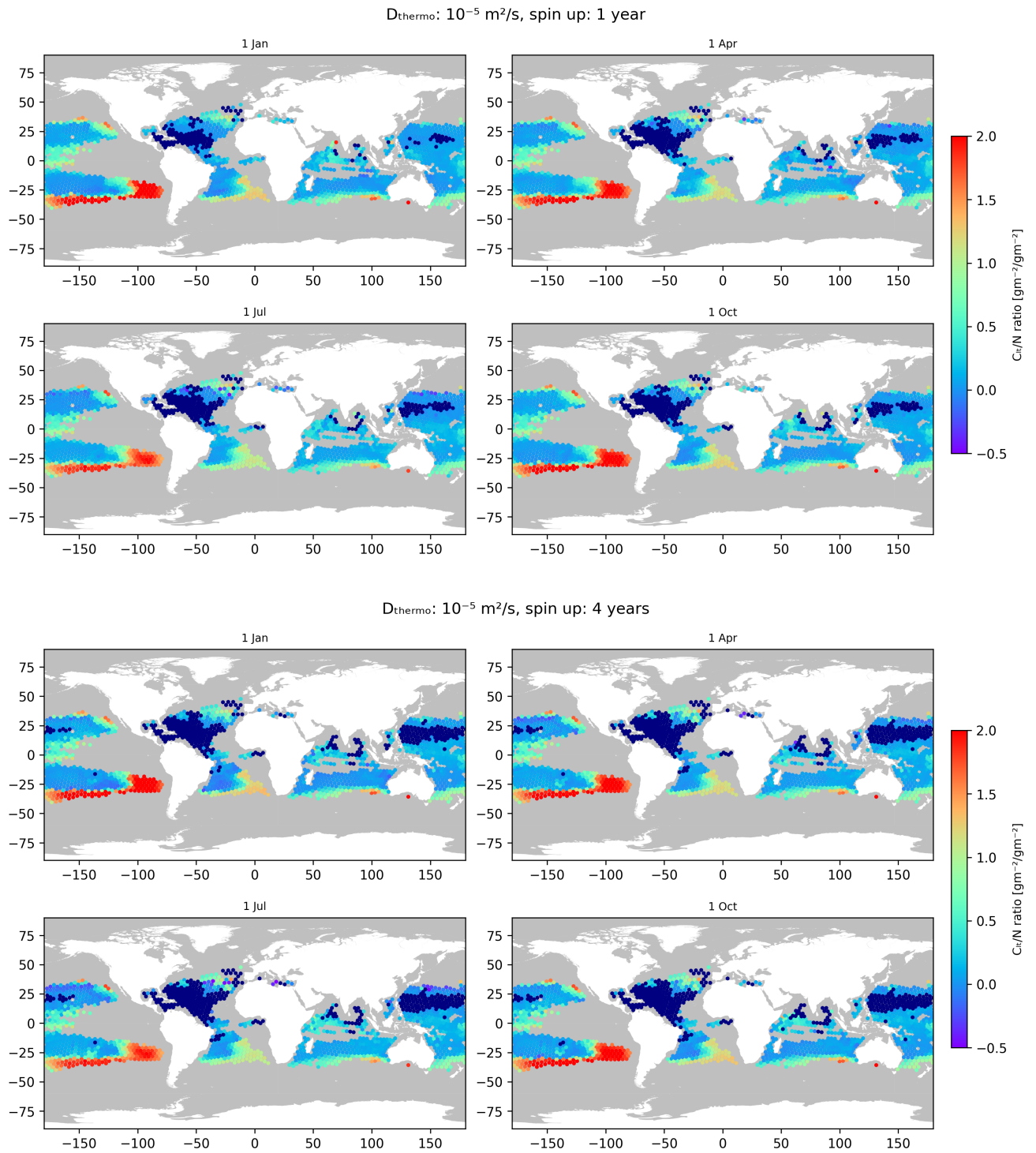
Figure E.9: Ratio of long-term C sequestration per unit N added [g m^{-2}/g m^{-2}] from fertilization in simulations with a thermocline diffusivity of 10^{-5} m^{2}s^{-1}. Top and bottom four figures are associated with 1 or 4 full years of baseline simulation spin-up, respectively. The dark blue hexagons had no nitrogen limitation in their mixed layer at the moment of fertilization, so no nitrogen addition took place.
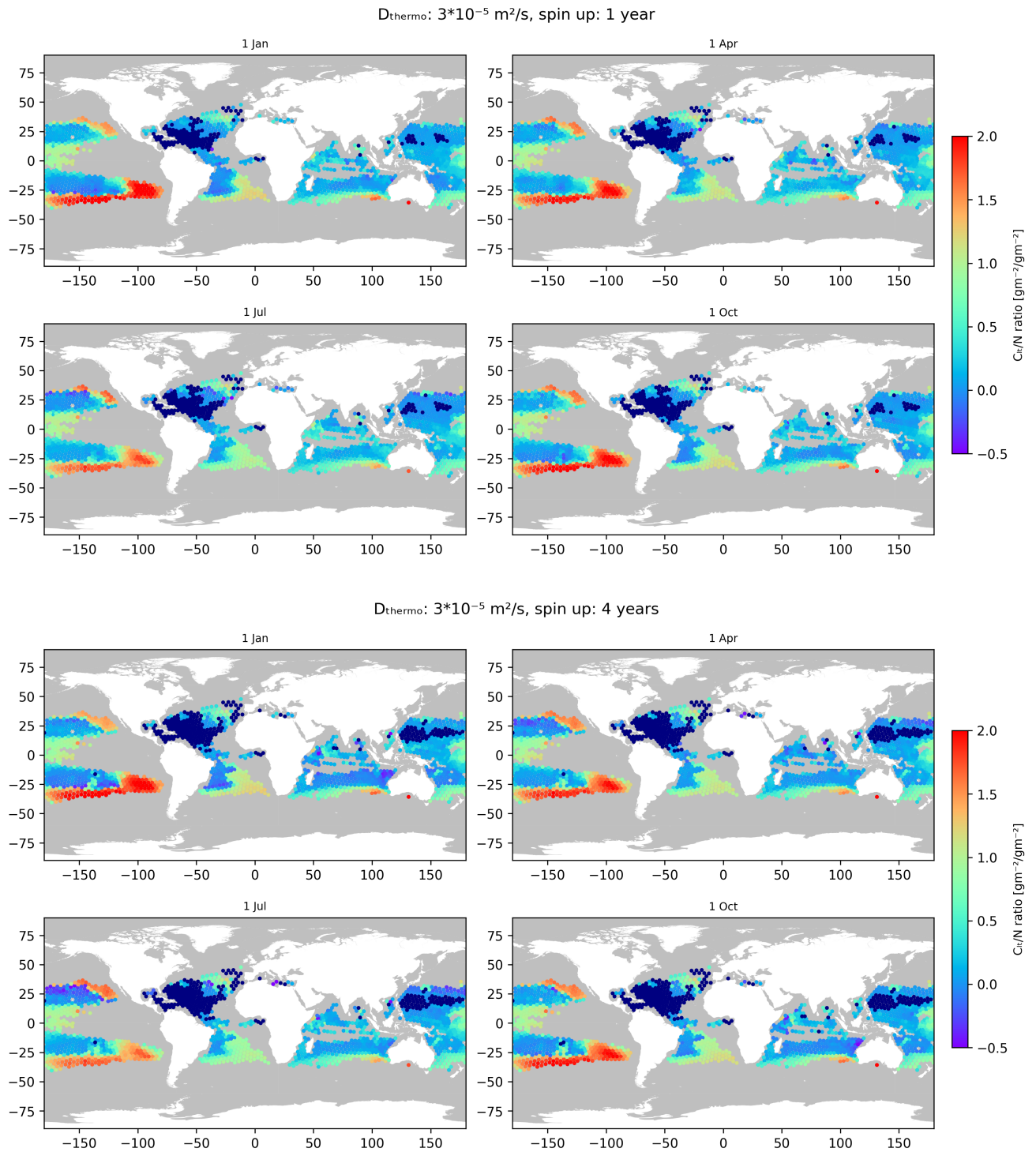
Figure E.10: Ratio of long-term C sequestration per unit N added [g m^{-2}/g m^{-2}] from fertilization in simulations with a thermocline diffusivity of $3 \cdot 10^{-5}$ m^{2}s^{-1}. Top and bottom four figures are associated with 1 or 4 full years of baseline simulation spin-up, respectively. The dark blue hexagons had no nitrogen limitation in their mixed layer at the moment of fertilization, so no nitrogen addition took place.
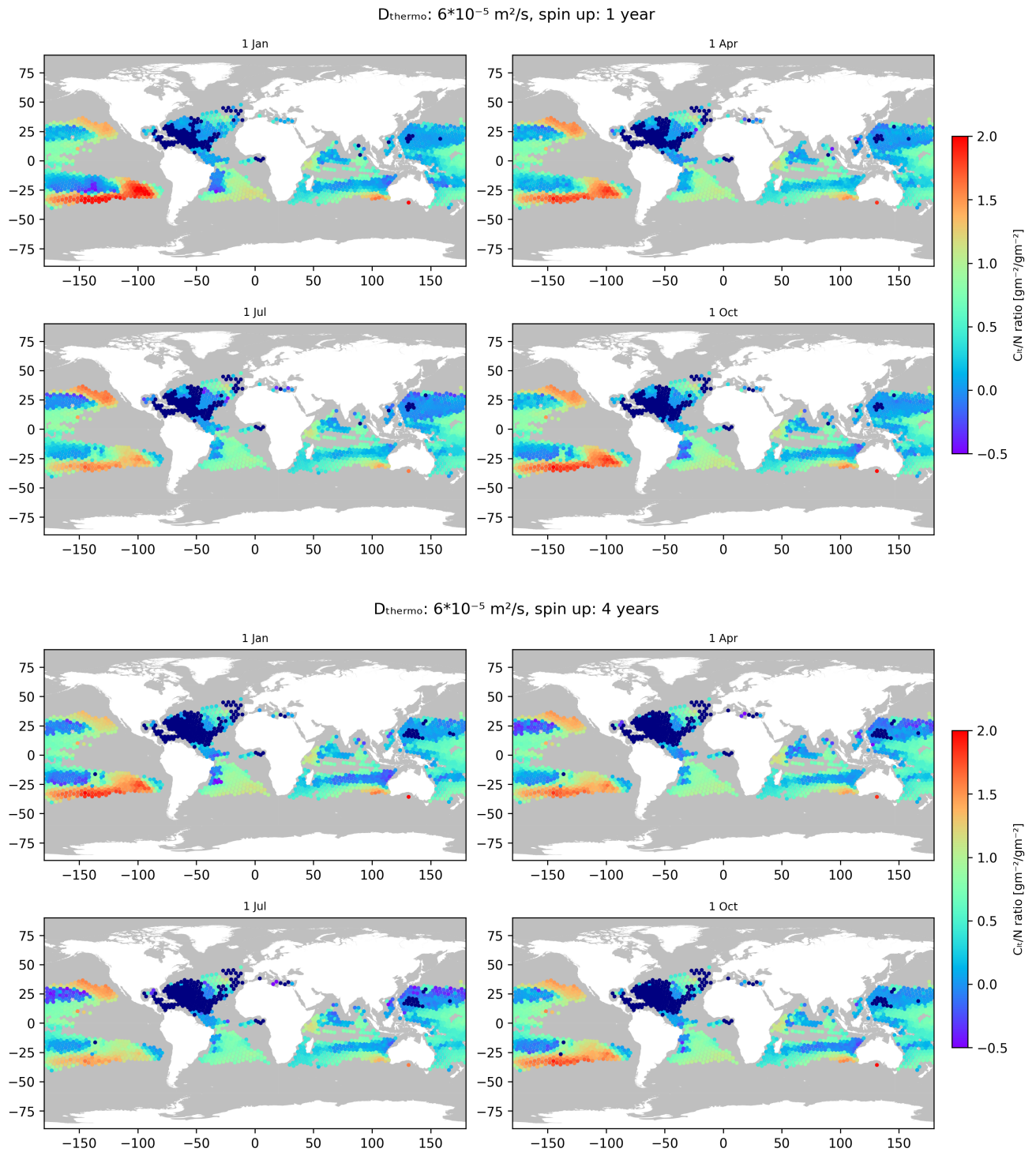
Figure E.11: Ratio of long-term C sequestration per unit N added [g m^{-2}/g m^{-2}] from fertilization in simulations with a thermocline diffusivity of $6 \cdot 10^{-5}$ m^{2}s^{-1}. Top and bottom four figures are associated with 1 or 4 full years of baseline simulation spin-up, respectively. The dark blue hexagons had no nitrogen limitation in their mixed layer at the moment of fertilization, so no nitrogen addition took place.
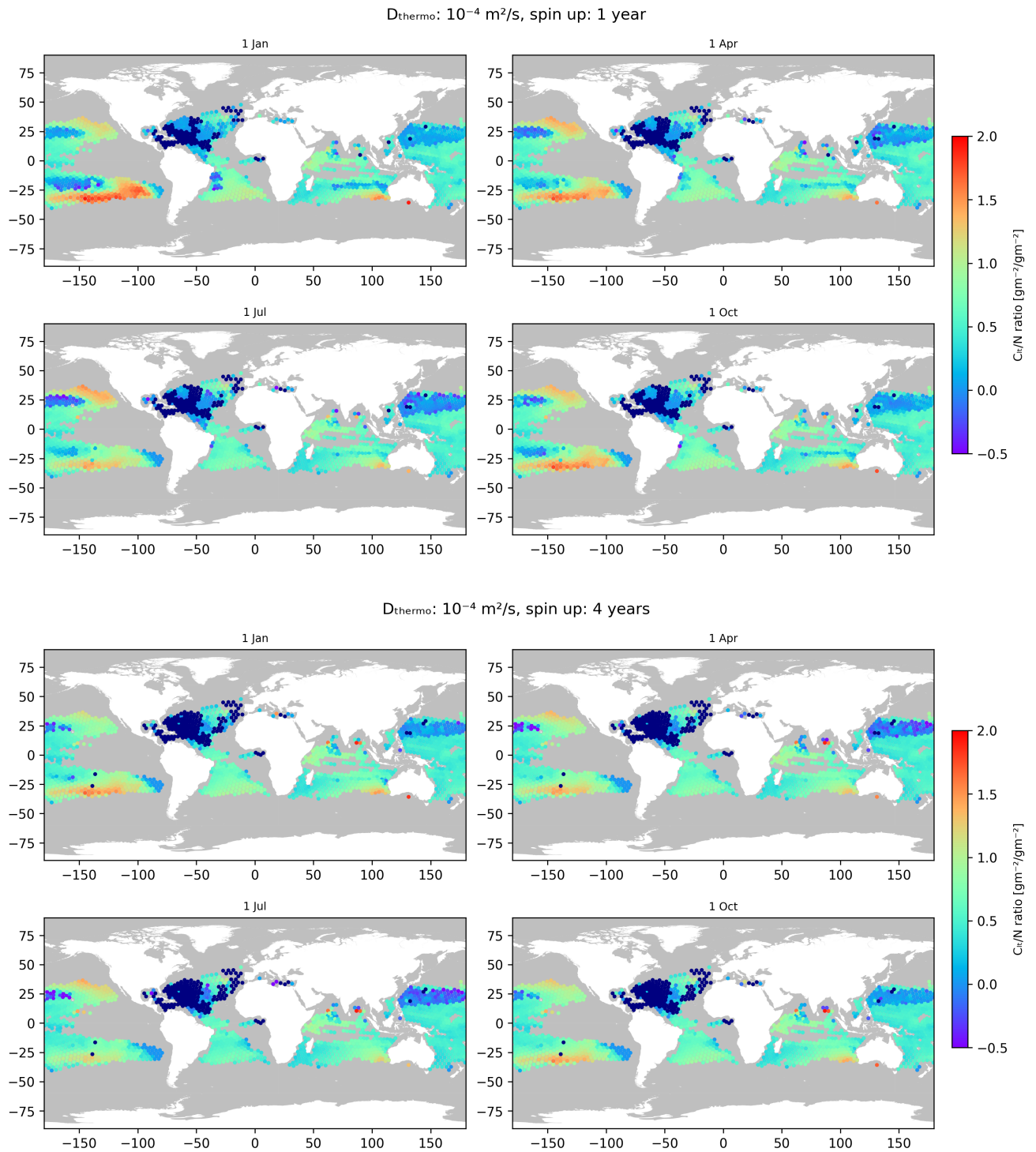
Figure E.12: Ratio of long-term C sequestration per unit N added [g m^{-2}/g m^{-2}] from fertilization in simulations with a thermocline diffusivity of 10^{-4} m^{2}s^{-1}. Top and bottom four figures are associated with 1 or 4 full years of baseline simulation spin-up, respectively. The dark blue hexagons had no nitrogen limitation in their mixed layer at the moment of fertilization, so no nitrogen addition took place.

E.3. Long run
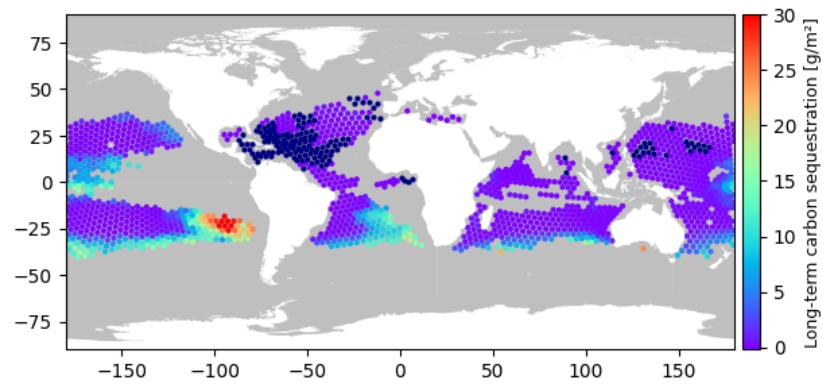
(a) Long-term carbon sequestration [g m^{-2}] from fertilization
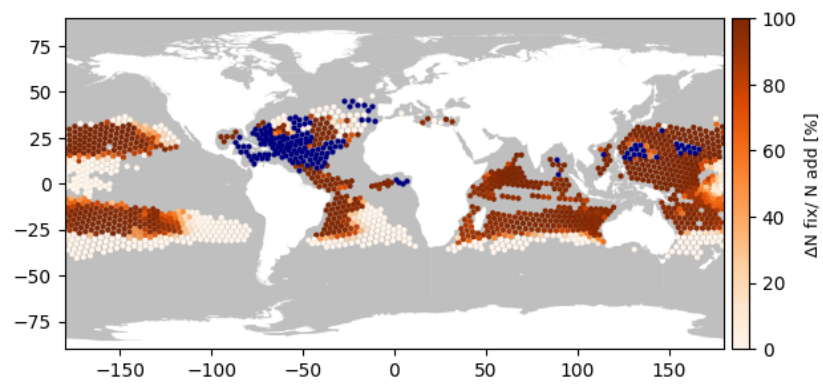
(b) Normalized offset [%] of the added nitrogen from reduced nitrogen fixation
(calculated by $\frac{Nfix,BS - Nfix,FS}{Nadd} * 100\%$)
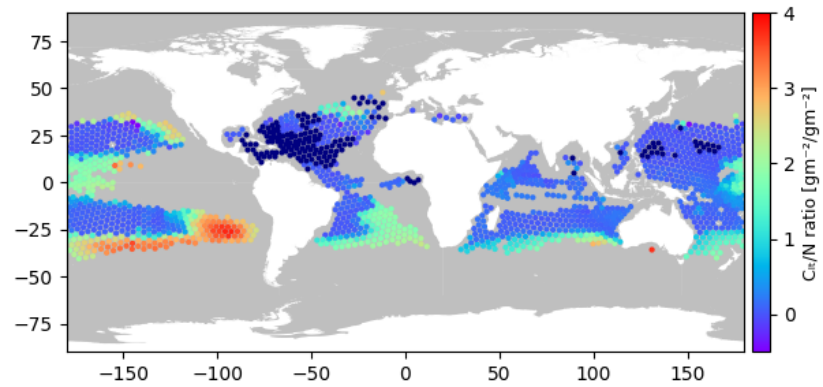
(c) Ratio of long-term C sequestration per unit N added [g m^{-2}/g m^{-2}]

Figure E.13: Results from the nitrogen fertilization after 50 years. The long run is characterized by a thermocline diffusivity of $3 \cdot 10^{-5}$ m^{2}s^{-1}, a baseline simulation spin-up of 1 year, and the nitrogen is added at the beginning of July.